POLITECNICO DI MILANO
DEPARTMENT OF MECHANICAL ENGINEERING
DOCTORAL PROGRAMME IN MECHANICAL ENGINEERING

FATIGUE ANALYSIS OF ROLLING ELEMENT BEARING UNDER HIGH-SPEED AND HEAVY-LOAD CONDITIONS

Doctoral Dissertation of:
Abdullah Yahya A Moafa

Supervisor:
Prof. Paolo Pennacchi

Tutor:
Prof. Tullio Tolio

The Chair of the Doctoral Program:
Prof. Andrea Bernasconi

2025 – Cycle XXXVII

Acknowledgement

In the name of ALLAH, the Most Gracious, the Most Merciful.

It is my firm belief that this dissertation could not have been completed without the guidance and mercy of ALLAH. My faith in ALLAH sustained me during the most difficult times and continually gave me hope. All praise and thanks be to ALLAH.

Pursuing a PhD at Politecnico di Milano has been an exceptional privilege. I am deeply grateful to everyone within the Politecnico di Milano community who supported and encouraged me throughout this journey.

I would like to express my sincere gratitude to my supervisor, Prof. Paolo Pennacchi, for his invaluable support, insightful guidance, continuous encouragement, and generous advice throughout this research journey. This work is truly a reflection of his persistent dedication and scholarly mentorship, not only in academic matters, but also in personal and non-academic aspects for which I am equally grateful.

My heartfelt thanks also go to Prof. Tullio Tolio, my PhD tutor, for his kind assistance and wise counsel, which greatly contributed to the development of this work.

I am deeply grateful to the Technical and Vocational Training Corporation (TVTC) in the Kingdom of Saudi Arabia for granting me the opportunity to pursue my doctoral studies and for their unwavering support, which played a crucial role in the completion of this academic endeavor.

I would also like to extend my sincere appreciation to the Department of Saudi Affairs and the Cultural Attaché at the Royal Embassy of the Kingdom of Saudi Arabia in Rome, Italy, for their tireless efforts in facilitating our journey as Saudi students and for their steadfast commitment to ensuring a comfortable, productive, and vibrant living environment in Italy. Their support was essential in navigating challenges and achieving academic success.

Finally, I am profoundly grateful for the unwavering love, sacrifices, and devotion of my father and mother, pillars of strength and values in my life. My deepest appreciation goes to my beloved wife *Suha*, whose patience and support illuminated my path, and to my son *Mohammad*, whose presence inspired me and gave my journey profound meaning. I also extend my heartfelt thanks to my brothers and sisters, and their families, for their constant encouragement and emotional support. Their belief in me has been a wellspring of motivation during the most trying moments of this journey.

Abdullah Yahya Moafa
Milan, December 2025

Abstract

This thesis presents an in-depth investigation into the mechanical performance and fatigue behavior of angular contact ball bearings (ACBBs) under varying applied loads and rotational speeds, integrating advanced modeling techniques with material comparisons. A novel mathematical and theoretical coupled model is developed, incorporating elastohydrodynamic lubrication (EHL), thermal transience, and multiparticle contact mechanics. The proposed model is benchmarked against the conventional Harris model to assess its predictive capability across a wide range of operational conditions. Key parameters studied include inner and outer raceway contact loads, ball-raceway contact angles, friction torque components, heat generation, and bearing fatigue life. Results indicate that the new model consistently predicts higher contact loads than the Harris model, particularly under elevated loads and at lower speeds, due to its consideration of local deformation, dynamic lubrication film behavior, and transient thermal effects. Contact angles and load distribution shift significantly with speed, highlighting the importance of centrifugal and gyroscopic effects at high RPMs. The thesis also evaluates the performance of three bearing materials—alloy steels, nickel-based superalloys, and titanium alloys. Alloy steels demonstrate superior load-deflection stiffness and contact load capacity, while titanium alloys exhibit the longest fatigue life under light loads but degrade faster under heavy loads. At 15,000 RPM, improved EHL and centrifugal force effects contribute to extended fatigue life, counteracting some of the detrimental impacts of high-speed operation. Friction torque analysis reveals a nonlinear increase with load and a strong speed dependency in viscous and spin components, driving substantial heat generation. Thermal analysis confirms that both spinning and viscous friction are the dominant contributors to heat under high-speed conditions. Fatigue life modeling shows an inverse relationship with applied load but improved endurance at extreme speeds due to favorable load redistribution and lubrication conditions. The findings of this work underscore the

necessity of integrating lubrication, thermal, and dynamic loading effects into bearing analysis for more accurate performance prediction. The proposed model enhances the understanding of ACBB behavior and offers valuable insights for optimized design, material selection, and predictive maintenance in demanding applications such as aerospace, automotive, and industrial machinery. Future work should include experimental validation and explore long-term reliability and defect evolution under extreme operating conditions. The operating conditions simulated in this study closely reflect those experienced by ball bearings supporting the main shaft in aircraft gas turbines.

Keywords: Fatigue life; Ball bearing; Skidding; Thermal deformation; Heat generation; Lubrication.

Nomenclature

Symbol	Parameter / Description	Unit
d_m	Pitch diameter of bearing (mean of inner and outer diameters)	mm
d_i	Inner ring diameter	mm
d_o	Outer ring diameter	mm
P_d	Diametral clearance (difference between outer and inner diameters minus 2D)	mm
f_i	Inner raceway curvature factor	-
f_o	Outer raceway curvature factor	-
A	Geometric parameter related to ring radii ($r_o + r_i$ - D or BD)	mm
B	Total curvature ($f_i + f_o$ - 1)	-
$\alpha°$	Initial bearing contact angle	degrees
P_w	Modified diametral clearance	mm
ΔP_d	Change in diametral clearance	mm
Δ_r	Inner ring diameter change due to interference fit	mm
Δ_h	Outer ring diameter change due to interference fit	mm
I_s	Inner ring interference parameter	mm
I_h	Outer ring interference parameter	mm
I_0	Initial installation interference	mm
ΔI_c	Change in interference due to centrifugal force	mm
ΔI_T	Change in interference due to thermal expansion	mm
D	Bearing ball diameter	mm
ω	Angular velocity (rad/s or rpm)	rpm
ω_m	Orbital angular velocity of rolling element	rpm
ω_R	Self-rotational angular velocity of rolling element	rpm
Γ_i	Thermal expansion coefficient of inner ring	1/K
Γ_s	Thermal expansion coefficient of shaft	1/K
ΔT_i	Temperature rise of inner ring	°C or K
ΔT_s	Temperature rise of shaft	°C or K
$h_{min}^{i,o}$	Dimensionless minimum oil film thickness (inner/outer)	-
$K_{oil}^{i,o}$	Oil film stiffness (inner/outer)	N/m
$U_{(i,o)}$	Dimensionless velocity parameter (inner/outer)	-
G	Dimensionless material parameter	-
Q_z	Dimensionless load parameter	-
R_x	Equivalent radius of curvature between rolling elements and raceways	mm
γ	Parameter equal to D/d_m	-
$K_{(i,o)}$	Combined stiffness from Hertzian and oil film stiffness (inner/outer)	N/m
$K_H^{i,o}$	Hertzian stiffness component (inner/outer)	N/m
F_a	Applied axial load	N
F_r	Applied radial load	N
δ_a	Relative axial displacement of inner and outer rings	mm
δ_r	Relative radial displacement of inner and outer rings	mm
θ	Relative angular displacement of inner and outer rings	radians
X_{1j}, X_{2j}	Intermediate geometric parameters at ball location j	mm
δ_{ij}, δ_{oj}	Contact deflections at inner and outer raceways at position j	mm
Q_{ij}, Q_{oj}	Contact loads on inner and outer raceways at position j	N
M_{gj}	Ball gyroscopic moment at position j	Nm
m_b	Mass of each rolling ball	kg
J_b	Moment of inertia of rolling ball	kg·m²

G	Gravitational force acting on the bearing	N
Skd_{theo}	Theoretical skidding coefficient	dimensionless
σ_{max}	Maximum compressive stress at the center of contact area	Pa
σ	Normal stress at any point within the contact area	Pa
τ_y	Shear stress due to fluid film lubrication	Pa
M_{total}	Total friction torque	Nm
M_l	Rolling friction torque	Nm
M_v	Viscous friction torque	Nm
P_l	Torque due to applied load	Nm
f_l	Factor depending on bearing design and relative bearing load	-
v_o	Oil kinematic viscosity	mm^2/s
Ω	Thermal conductivity	W/m·K
$\wp_i$	Distance between heat transfer points on inner ring	mm
$\wp_o$	Distance between heat transfer points on outer ring	mm
C_s	Maximum stress at the outer raceway	Pa
φ_s	Parameter related to bearing geometry	-
i	Number of rows in bearing	-
X_s	Radial load factor	-
Y_s	Axial load factor	-
y_e	Distance in Y direction	mm
z_e	Distance in Z direction	mm
L	Bearing fatigue life (million revolutions)	million revs
L_H	Bearing fatigue life in hours	hr
Q_{ci}	Load capacity of inner raceway	N
Q_{co}	Load capacity of outer raceway	N
α_i	Contact angle of inner raceway	degrees
α_o	Contact angle of outer raceway	degrees
δ_K	Axial deflection constant	mm
K_n	Axial deflection constant normalized	-
k	Ellipticity ratio (a/b)	-
F	Contact force factor	-
z	Contact force exponent	-
a^, *b*^	Dimensionless semi-major and semi-minor axes of contact ellipse	-
a, b	Semi-major and semi-minor axes of contact ellipse	mm
δ^*	Dimensionless contact deflection	-
δ	Contact deflection	mm
m	Mass (general variable)	kg
β	Angle between W and z' axes in ball coordinate system	degrees
γ'	Parameter ratio D/d_m	-
λ_{ij}, λ_{oj}	Load distribution factors at inner and outer raceway contacts	-
F_{cj}	Centrifugal force at ball j	N
ω_R / ω	Ratio of ball self-rotation speed to shaft speed	-
ω_m / ω	Ratio of ball orbital speed to shaft speed	-
$\tan\beta$	Tangent of angle β	-
M_{si}, M_{so}	Friction torque due to spinning about axis normal to inner/outer raceway	Nm
H_{fij}, H_{foj}	Bearing frictional power loss at each rolling element inner/outer raceway	W
H_{fi}, H_{fo}	Total frictional power loss inner/outer raceway	W
H_{lv}	Viscous heat generated	W
$H_{i,o_{total}}$	Total heat generated on inner/outer raceway	W
u_s	Bearing cage surface velocity	m/s

P_r	Prandtl number	-
h_V	Film coefficient of heat transfer	$W/m^2 \cdot K$
S_i, S_o	Area normal to heat flow in inner/outer ring	mm^2
ΔT_i, ΔT_o	Temperature differences between shaft and inner ring, and outer ring and housing	K
$\wp_i$, $\wp_o$	Distances between heat transfer points inner/outer ring	mm
m_b	Mass of ball	kg
J	Moment of inertia related to gyroscopic moment	$kg \cdot m^2$

Thesis Outline

Chapter 1: Introduction

This chapter provides the foundation of the thesis by introducing the importance of angular contact ball bearings (ACBBs) in high-speed mechanical systems. It outlines the background, motivation, and challenges in modeling fatigue and thermal behavior under realistic operating conditions. The chapter also clearly defines the research problem, objectives, scope, and significance, setting the stage for the theoretical and numerical investigations that follow.

Chapter 2: State of the Art

A comprehensive review of the state-of-the-art literature related to the dynamic, thermal, tribological, and fatigue behavior of ACBBs is presented. The chapter discusses limitations in conventional models such as the Harris model and emphasizes recent advances in elastohydrodynamic lubrication (EHL), preload optimization, defect modeling, cage dynamics, and material behavior. Research gaps are identified and serve as the basis for the novel coupled model developed in this thesis.

Chapter 3: Theoretical Analysis of Rolling Bearings

This chapter introduces the mathematical formulations and theoretical framework developed to model the mechanical, thermal, and tribological behavior of ACBBs. It covers key phenomena such as changes in contact angles due to interference fits, effects of bearing clearances and lubricant film, dynamic responses under high-speed conditions, stress distribution, heat generation, and fatigue life estimation. The model integrates EHL, centrifugal and gyroscopic forces, and thermal effects to enable accurate prediction of bearing behavior.

Chapter 4: Results and Discussion

This chapter presents and analyzes the simulation results obtained from the proposed theoretical model. It examines the effects of applied loads and rotational speeds on

various bearing parameters including contact loads, contact angles, friction torque, and heat generation. Material comparisons are made between alloy steels, nickel-based superalloys, and titanium alloys in terms of stiffness and fatigue life. The findings validate the enhanced capabilities of the proposed model over traditional approaches.

Chapter 5: Software Implementation

The computational tools and simulation environment used in the study are described in this chapter, with a focus on MATLAB. It highlights the historical development, reliability, and flexibility of MATLAB for scientific modeling. Code snippets and screenshots illustrate the implementation of the mathematical model, enabling reproducibility and transparency in the research process.

Chapter 6: Conclusions and Recommendations

This final chapter summarizes the main findings, highlights the contributions of the research to the field of bearing analysis, and outlines its practical implications for design and maintenance in aerospace and industrial applications. Limitations of the current study are acknowledged, and suggestions for future work—including experimental validation and defect progression modeling—are provided to guide continued research.

Table of Content

Acknowledgement.....
Abstract I
Nomenclature III
Thesis Outline VI
Table of Content VIII
Chapter 1: Introduction 1
1.2 Problem Statement 1
1.3 Research Objectives 2
1.4 Scope of the Study 2
1.5. Application of the Study to Gas Turbine Bearings in Aircraft: A Technical Justification of Operating Conditions 3
1.5.1. Relevance of L10 Life in Aerospace Bearing Design 3
1.5.2. Simulated Operating Conditions: Alignment with Gas Turbine Realities .3
1.5.3. Material Selection: Comparative Analysis of Three Bearing Alloys 4
1.5.4. Lubrication Strategy: Use of High-Performance Mineral Oil 4
1.5.5. Fit and Tolerance Considerations 5
Chapter 2: State of the Art.....6
2.1 Introduction.....6
2.2 Dynamic Modeling of Angular Contact Ball Bearings 7
2.3 Skidding and Overskidding Behavior.....9
2.4 Preload Effects and Optimization 10
2.5 Lubrication, Friction, and Thermal Effects 12
2.6 Material Behavior and Fatigue Life Modeling 14
2.7 Defect Modeling and Failure Mechanisms 16
2.8 Cage Dynamics and Stability.....17
2.9 Summary and Research Gaps 19
Chapter 3: Theoretical analysis of rolling bearing 23

3.1. Initial angles change due to bearing interference fit 26
3.4. Loading and stress distribution modelling 37
3.5. Bearing generation heat modeling 44
3.6. Bearing fatigue life calculation modelling 49
3.7. Model Structure and Computational Flow 52
Chapter 4: Results and discussion 55
4.1. Simulation Input Parameters and Model Configuration 55
4.2. Effect of applied load on the inner raceway contact load at various speeds 57
4.3. Effect of applied load on the outer raceway contact load at various speeds 60
4.4. Effect of applied load on the ball raceway contact angles at various speeds 65
4.5. Effect of applied load on the bearing friction at various speeds 69
4.6. Effect of applied load on the generated heat at various speeds 73
4.8. Load-deflection constants of ball bearing inner raceway for different materials 80
4.10. The fatigue life behaviour of the bearing across different materials 82
Chapter 5: Description of the software 84
5.1. MATLAB Code Description by Line Ranges 84
5.1.1. Detailed Explanation of the MATLAB Code 85
Chapter 6: Conclusions and Recommendations 111
6.1. Summary of Findings 112
6.2 Significance of the Study 113
6.3. Contributions 114
6.4. Practical Implications 114
6.5. Limitations 114
6.6. Recommendations for Future Work 115
Reference 116
List of Figures 121
List of Tables 123
Appendix 124
Appendix A: The Written Code 124

Appendix B: MATLAB in the Computational Framework 152
B.1 Integration of MATLAB in Computational Frameworks: Reliability, History, and Applications 152
B.2. Numerical Algorithms and Implementation Details 152
B.3. Historical Background and Evolution of MATLAB..... 154
B.4. Reliability and Computational Strength of MATLAB 154
B.5. Applications for MATLAB in Scientific Research 154
B.6. Notable Examples of MATLAB in Research..... 155

Chapter 1: Introduction

Rolling element bearings are fundamental components in modern mechanical systems, enabling smooth rotational motion and supporting various load types with high efficiency and precision. Among them, angular contact ball bearings (ACBBs) are widely used in high-speed, high-load applications due to their ability to simultaneously accommodate axial and radial forces. As mechanical systems continue to evolve toward higher performance demands—particularly in aerospace, automotive, and advanced industrial applications—the need for accurate prediction and optimization of bearing behavior has become increasingly critical. This thesis investigates the mechanical and thermal behavior of ACBBs under varying operating conditions, with a focus on enhancing modeling accuracy and evaluating the influence of different bearing materials on performance and fatigue life.

1.2 Problem Statement

Despite the critical role ACBBs play in modern mechanical systems, conventional models are often inadequate for predicting their behavior under high-speed, high-load conditions. These models typically ignore important physical effects such as lubricant film behavior, heat generation, and the influence of centrifugal and gyroscopic forces. In addition, current literature lacks a unified framework that couples mechanical, thermal, and tribological phenomena and assesses their collective impact on bearing performance across different material types.

This thesis addresses these limitations by developing a novel mathematical and theoretical coupled model that integrates EHL, thermal transience, and contact mechanics to evaluate the detailed behavior of ACBBs under varying operating conditions. Moreover, it investigates how different bearing materials—namely alloy steels, nickel-based superalloys, and titanium alloys—affect key performance indicators such as contact load, stiffness, friction, heat generation, and fatigue life.

1.3 Research Objectives

The primary objectives of this research are:

1. To develop a novel mathematical and theoretical coupled model for ACBBs that incorporates elastohydrodynamic lubrication, heat generation, and multiparticle contact mechanics.
2. To compare the performance of the proposed model with the conventional Harris model in predicting contact loads, angles, torque, and fatigue life under various operating conditions.
3. To evaluate the effect of rotational speed and applied axial load on key bearing parameters, including frictional torque, heat generation, and power loss.
4. To perform a comparative analysis of three bearing materials (alloy steels, nickel-based superalloys, and titanium alloys) in terms of load-deflection behavior, contact load, and fatigue performance.
5. To provide practical insights for bearing design, lubrication strategy optimization, and material selection in high-speed mechanical systems.

1.4 Scope of the Study

This thesis focuses on angular contact ball bearings subjected to axial loading and rotational speeds ranging from 6000 to 15000 RPM. The developed model simulates the contact interaction between the ball elements and raceways, considering temperature-dependent material properties, lubricant film thickness, and dynamic effects such as centrifugal and gyroscopic forces. Material behavior is assessed under both static and dynamic conditions, and fatigue life is estimated based on established bearing life equations, enhanced by more accurate load predictions.

The study is purely numerical, using a novel mathematical and theoretical coupled model. While the model offers strong predictive capabilities, experimental validation is identified as a future extension.

1.5. Application of the Study to Gas Turbine Bearings in Aircraft: A Technical Justification of Operating Conditions

Rolling-element bearings are critical components in high-performance mechanical systems, particularly in aerospace propulsion units such as gas turbines. These bearings are subjected to extreme operating conditions, including high rotational speeds, substantial axial and radial loads, elevated temperatures, and stringent lubrication requirements. The present study was designed to simulate these demanding conditions, with a specific focus on the main shaft support bearings in aircraft gas turbines. The operating parameters used—rotational speeds up to 15,000 rpm, axial loads reaching 47,500 N, and high-temperature environments—were selected to reflect the real-world stresses encountered in such applications.

1.5.1. Relevance of L10 Life in Aerospace Bearing Design

The L10 life rating, as defined by ISO 281, represents the number of revolutions at which 90% of a group of identical bearings are expected to operate without fatigue failure. This metric is widely adopted in aerospace engineering due to its statistical reliability and its ability to account for dynamic load conditions. Studies by Zaretsky et al. [1] have demonstrated that L10 life is highly sensitive to variations in load, speed, lubrication, and temperature—factors that are all prevalent in gas turbine environments [2].

1.5.2. Simulated Operating Conditions: Alignment with Gas Turbine Realities

The study replicated the operational envelope of main shaft bearings in aircraft gas turbines. These bearings are typically exposed to:

• **High rotational speeds (up to 15,000 rpm),** which induce significant centrifugal forces and thermal gradients [3].

• **Substantial axial loads (up to 47.5 kN),** resulting from pressure differentials across the compressor and turbine stages [3].

• **Elevated temperatures**, often exceeding 200°C, due to proximity to combustion zones and frictional heating [4].

• **Tight interference fits** between the bearing and shaft to prevent micro-slippage and ensure thermal stability [5].

These conditions were carefully modeled in the study to ensure that the fatigue life predictions (L10) would be directly applicable to aerospace-grade bearing systems.

1.5.3. Material Selection: Comparative Analysis of Three Bearing Alloys

To enhance the applicability of the findings, the study included a comparative evaluation of three bearing materials commonly used in aerospace applications:

• AISI 52100 (100Cr6): A high-carbon chromium steel known for its hardness and fatigue resistance under moderate temperatures.

• Nickel-Based Superalloys: High-performance materials engineered for extreme thermal environments, offering exceptional creep resistance, structural stability, and oxidation protection at elevated temperatures exceeding 800°C.

• Titanium Alloys: Lightweight, corrosion-resistant materials with a high strength-to-weight ratio, commonly used in aerospace and biomedical applications due to their ability to maintain mechanical integrity at elevated temperatures up to 600°C.

Each material was analyzed under identical loading and thermal conditions to assess its influence on bearing life and performance. The results revealed significant differences in L10 life, with titanium alloys outperforming the others in corrosion-resistant endurance with the relatively light loads, albeit at a higher material cost.

1.5.4. Lubrication Strategy: Use of High-Performance Mineral Oil

The study employed a high-performance mineral oil-based lubricant, selected for its thermal stability, oxidation resistance, and compatibility with aerospace bearing materials. Mineral oils remain widely used in aviation due to their cost-effectiveness and proven reliability in controlled environments [6]. The lubricant used had a viscosity

index optimized for high-speed applications and a flash point exceeding 250°C, ensuring consistent film thickness and minimal degradation under thermal stress.

Proper lubrication is essential not only for reducing friction and wear but also for dissipating heat and preventing surface fatigue. The study's findings align with those of SKF and NSK, which emphasize the role of lubricant viscosity and thermal conductivity in extending bearing life [7].

1.5.5. Fit and Tolerance Considerations

The mechanical fit between the bearing and shaft was modeled using interference fits (e.g., k6 or m6), as recommended by ISO 286 and DIN 620 for high-speed, high-load applications [8]. These fits ensure that the bearing remains securely seated under thermal expansion and dynamic loading. Improper fits can lead to fretting corrosion, misalignment, and premature failure—risks that are particularly unacceptable in aerospace systems.

Chapter 2: State of the Art

Understanding the advanced behavior of angular contact ball bearings (ACBBs) is crucial for further development of the performance and reliability of high-speed rotating machines. Investigation of bearing operation's tribological, thermal, and mechanical behavior has significantly increased in the last decades. A number of modeling techniques have been attempted by researchers for estimation of contact forces, temperature rise, lubrication film behavior, and fatigue life, especially at high load as well as speed ranges. Traditional models, i.e., the Harris model, however, rely on simplifying assumptions that compromise the validity of these models under the dynamic, real-life operating conditions. This chapter presents a critical overview of the key developments in the modeling and analysis of ACBBs with emphasis on elastohydrodynamic lubrication (EHL), thermal effects, preload strategy, skidding behavior, cage dynamics, and material effects on fatigue performance. The aim is to outline the limitations of the state-of-the-art methods and determine the research gaps that are considered in this thesis with a a novel mathematical and theoretical coupled model.

2.1 Introduction

Angular contact ball bearings (ACBBs) have wide application in high-speed and high-precision machinery due to their ability to support axial and radial loads. Their performance influences the reliability, efficiency, and service life of aerospace, automotive, and industrial machinery systems. Consequently, there is a large amount of research that has been focused on comprehending, modeling, and improving the dynamic, thermal, tribological, and fatigue performance of ACBBs under various operating conditions.

Classical bearing theories like the Jones raceway control theory and the Harris model have been the standard to calculate contact loads and stiffness and fatigue life. Such theories, however, make simplifying assumptions and do not address such complex

behaviors under the actual conditions of operation like transient lubrication behaviors, thermal growth, skidding, and cage motion. Progress in thermo-elastohydrodynamic lubrication (TEHL), multi-body dynamics, and a novel mathematical and theoretical coupled model allowed physically more realistic and more refined models to fill the gap between experimental performance and theory.

Besides this, more emphasis has been laid on the understanding of the influence of material selection, preload conditions, lubrication regimes, and surface defects on bearings' performance. Research has progressed from monolithic mechanical to coupled thermo-mechanical, tribological, and fatigue life investigations. The chapter provides the consistent picture of the important contributions in the literature on dynamic modeling, skidding behavior, preload optimization, lubrication and heat generation, material behavior, defect modeling, and cage dynamics. Investigations in these areas are the analytical and theoretical foundation of the thesis under review.

2.2 Dynamic Modeling of Angular Contact Ball Bearings

Accurate dynamic simulation of ACBBs is the key to simulating their performance under varying loads, speeds, and boundary conditions. Early models provided quasi-static or highly simplified dynamic analysis without accounting for complex interactions such as thermal expansion, cage dynamics, and action of lubricant. New research work has advanced to create multi-DOF, thermo-mechanical, and elastohydrodynamic models to more accurately simulate bearing behavior.

Gao et al. [9] introduced a kinematic-Hertzian-thermo-hydrodynamic (KH-THD) model to model the interaction between kinematics, contact forces, lubrication, and thermal effects. Novel, unexplored phenomena such as over-skidding, cage speed being larger than theoretical prediction, especially in large ACBBs, were uncovered by their study. The model showed that ignoring thermal friction effects results in enormity-sized prediction errors in the behavior of the rolling element, especially in the high speed or starved lubrication regime.

Based on that, Gao et al. [10] proposed a KH-TEHD (thermal-elastohydrodynamic) model with layer loop structure for simulating the thermal deformation, ball-cage contact, hydrodynamic pressure between guide ring and cage, and lubricant starvation.

It was experimentally verified by demonstrating the superiority of the current formulations by unveiling the influence of thermal expansion and cage-guide contact on the stability and skidding of bearings. Their research showed that overskidding is favored by bearing size and running speed, and thermal deformation is four times greater than ball-raceway clearance under poor lubrication.

Wen et al. [11] introduced a multi-DOF dynamic model based on the comprehensive interaction of all the components of the bearing, such as cage and oil lubrication, under defective conditions. Five DOFs of the inner ring, six DOFs of each of the balls, and three of the cage were adopted in the model. Their study demonstrated that surface defects lead to periodic angular misalignments, changes in ball-raceway load characteristics, and cage pocket impacts. The model also demonstrated that defect size, load, and speed have profound impacts on contact force oscillation and traction behavior.

Mishra et al. [12] offered a comparative study in the development of three dynamic models of differing complexity for deep groove ball bearing fault diagnosis, from basic kinematics-based Simulink models to sophisticated multi-body dynamics in ADAMS. Compared with experimental vibration signatures, it was revealed that complex models with realistic contact mechanics provide significantly better predictions, consistent with the increasing trend towards higher-fidelity simulations in bearing diagnostics.

Analytical modeling was advanced further by Gao et al. [13] through the establishment of the Jones raceway control hypothesis. This included clearance, centrifugal displacement, and thermal deformation and could predict contact states and fatigue life more precisely under axial and combined loads. This is a significant step towards the inclusion of mechanical and thermal modeling and fatigue prediction.

Together, these studies represent a pattern in the literature: that kinematic, lubrication, thermal response, contact mechanics, and cage dynamics must be accounted for in dynamic ACBB models if they are to be highly accurate in their predictions for performance. They also confirm the inclusion of more advanced phenomena such as skidding, fatigue failure, and thermal degradation, which are considered in the sections below.

2.3 Skidding and Overskidding Behavior

Skidding is one of the major dynamic effects in ACBBs, especially at high speeds or low loads. It happens when the rolling elements are no longer able to sustain pure rolling contact with the raceways and experience partial or complete sliding. Not only does it increase friction and heat generation but also wear, make lubrication harder, and introduce failure modes such as pitting or cage instability. In extreme cases, overskidding—when the rolling elements move faster than their theoretical pure rolling speed—can occur, as has been observed in a series of recent research studies.

Large-size ACBBs' overskidding phenomenon was experimentally observed for the first time by Gao et al. [9]. Overskidding is the condition where the cage/rotor speed ratio is higher than the calculated theoretically optimum for the ideal rolling condition, according to their definition. The new phenomenon led to the development of the KH-THD model based on contact kinematics, thermal, ball-cage interaction, and lubrication effects. The study confirmed that common assumptions of cage velocity cannot hold in the case of variable lubrication and high-speed operation scenarios, particularly when the inner dynamics are altered by frictional heating due to skidding. Describing the phenomenon in more detail, Gao et al. [10] used the KH-TEHD model to demonstrate how overskidding severity is reinforced by rotating speed and bearing size. Using experimental data, they demonstrated how lubricant starvation promotes skidding and creates four times the normal ball-raceway clearance using thermal expansion. The model also demonstrated the significant role of cage-guide hydrodynamic pressure in stabilizing the cage motion and preventing skidding oscillation.

Chunjiang et al. [14] examined gyroscopic torque and traction force equilibrium to study the skidding threshold. The results confirmed that there exists a gyroscopic equilibrium friction coefficient that is highly speed- and axial load-sensitive. The inner contact angles rise and outer contact angles decrease with an increase in axial force, and there result corresponding variations in friction torque and contact forces. The study provided a new perspective on the contribution of gyroscopic effects to localized skidding with emphasis on high-speed conditions.

Wang et al. [15] developed a complex dynamic model that includes interactions between the balls, raceways, cage, and lubricant. Their findings verified the need for a minimum axial load to counteract skidding. Below the minimum load, the orbital and

rotational velocities of the balls are inadequate for pure rolling, and there is excessive skidding—particularly in the lightly loaded regions of the bearing. The study also noted that with combined axial-radial loading, non-uniform load distribution causes localized skidding despite the overall load being within the safe zone.

Xu et al. [16] extended skidding analysis by establishing an advanced dynamic model with time-dependent stiffness and thickness of the oil film, bearing clearances, and cage dynamic behaviors. Experimental validation on a synchronous differential encoder (SDE) system established that skidding severity is positively correlated with bearing clearance and adequately captured in vibration responses. The slip ratio, the most important indicator of skidding severity, was found to rise with the increase in the clearance—verifying the model accuracy and its appropriateness for real-time application.

Yunlong et al. [17] provided complementary insight by combining a dynamic bearing model with a thermo-elastohydrodynamic lubrication (TEHL) model. They indicated that skidding is most related to poor lubrication performance and heat generation, especially if improper axial load is applied at a particular speed. Critical speed and load parameters at which lubricant film failure and skidding will be thermally self-sustained with the risk of bearing seizure were determined from their model.

Together, these studies provide a complete picture of skidding and overskidding in ACBBs. They emphasize that axial load, speed, clearance, lubrication regime, and cage dynamics all contribute to skidding behavior. Most importantly, they demonstrate that skidding is not a mechanical but a thermal and tribological behavior and that it requires coupled dynamic models and experimental validation to allow confident prediction and countermeasure methods.

2.4 Preload Effects and Optimization

Preloading is one of the important design and operating parameters of angular contact ball bearings (ACBBs) and directly influences internal load distribution, stiffness, change in contact angle, skidding, friction, and fatigue life. Insufficient preload results in ball-raceway separation and excessive vibration, while over-preloading will result in

excessive stress, frictional heat, and early failure. Optimal preload is therefore essential for achieving optimal bearing performance and service life.

Zhang et al. [18] introduced a quasi-dynamic model to examine the impact of preload on ball-raceway contact conditions for various loads and speeds. The model accounted for centrifugal and gyroscopic effects and introduced a criterion for the detection of ball-raceway separation. The results showed that the number of loaded balls, contact force distribution, and fatigue life are all directly affected by preload. Low and also very high preloads are harmful to service life—either by applying single ball loads or by raising internal stress. An optimal preload range that would reduce these and provide maximum fatigue life was established in the work.

Xu et al. [19] proposed an analytical approach of preload designing based on Hirano's skidding criterion. The approach determines the critical axial preload for pure rolling motion at various speeds. It was experimentally confirmed that the optimal preload reduces bearing temperature and friction, particularly at operating speeds exceeding 10,000 RPM. The level of this type of preload was found to be speed-dependent, confirming that constant preload values for various operating conditions are not adequate.

Wu et al. [20] explored ACBBs' thermal performance in non-uniform preload conditions, which are common due to assembly or manufacturing errors. A three-degree-of-freedom model was employed to model the heat generation by a novel mathematical and theoretical coupled model of the temperature field. Their finding was that non-uniform preload minimizes localized heat generation and peak operating temperatures relative to uniform preloads, an unanticipated advantage in some applications. This finding warrants the practical use of distributed or semi-rigid preload configurations to induce thermal enhancement.

Yunlong et al. [17] also investigated TEHL preload, showing how improper preload results in inferior lubrication and rising temperature, especially at high speed. Their simulations indicated a significant preload-speed interaction, whereby the preload must be optimized in order to achieve maximum film thickness and prevent thermal failure. At low preload, breakdown of the film occurs at high speeds, while excessive preload increases contact pressure and shear heating.

In addition, preload was also shown to influence skidding behavior. Wang et al. [15] determined that minimal levels of preload must be provided in order to prevent skidding by creating adequate ball orbital and spin speeds. In the absence of proper preload, orbital motion lags behind the theoretical rolling motion, resulting in sliding and local overheating. Gao et al. [10] confirmed that cage whirling oscillations also increase in the event of improper preload, particularly when there is starved lubrication or unbalance. From a practical perspective, preload optimization is a trade-off between thermal control, mechanical stability, and wear reduction. The research addressed in this review unanimously supports analytical or simulation-assisted preload optimization based on parameters such as temperature, load, speed, clearance, and lubrication. Such methods provide a more robust basis for preload design relative to traditional empirical rules and are critical in high-precision and high-speed applications of bearings.

2.5 Lubrication, Friction, and Thermal Effects

Lubrication is the key to the performance and reliability of angular contact ball bearings (ACBBs), particularly at high speeds. Lubrication reduces friction and wear and also acts as a coolant. The relationship between lubrication, heat generation, and contact mechanics is, however, complicated, even more so at dynamic operating conditions. Improved understanding of elastohydrodynamic lubrication (EHL) and thermo-elastohydrodynamic lubrication (TEHL) in the bearing contact area has been achieved through the inclusion of these effects in more realistic models of bearing action.

Yunlong et al. [17] propose a comprehensive model integrating dynamic behavior and TEHL analysis. They demonstrated that speed and applied load significantly influenced film thickness, frictional heat generation, and power loss. Importantly, they demonstrated that application of axial load can result in lubrication film breakdown, inducing sliding, localized heating, and resulting thermal failure. The critical speed and preload combinations yielding sufficient film formation were determined in their study, emphasizing the significance of integrated lubrication modeling in bearing design.

Zheng et al. [21] noted the heat resulting from vibration in ACBBs, wherein the dynamic vibration contributes significantly to power loss and temperature rise—factors that had been traditionally overlooked by traditional thermal models. Their vibration-

energy model demonstrated how vibratory motions not only modify the bearing loads but also add additional spin power loss. By incorporating these factors in a thermal network model with experimentally correlated parameters, the study improved the precision of temperature rise prediction with applicability to spindle-bearing applications.

Shi et al. [22] analyzed the influence of film thickness and surface texture on lubricating performance. Through the integration of quasi-dynamic modeling, micro-TEHL analysis, and a novel mathematical and theoretical coupled model, they demonstrated that surface textures transverse to the lubricant entrainment direction enhance film formation and reduce surface pressure and shear stress. By contrast, longitudinal textures have an adverse influence. Their research also demonstrated that negative surface roughness profile skewness and low kurtosis improve fatigue life, and the surface finish assists lubricant-film efficiency.

Martin et al. [23] tested scuffing resistance using various lubricants and speeds using high-speed rig testing with M50 bearing steel. They found that the traditional PV (pressure × velocity) criterion was not sufficient to predict failure. Instead, they found that failure would occur when the EHL film thickness was approximately equal to the maximum surface roughness and that this corroborated the effectiveness of the film thickness to surface roughness ratio as the new scuffing limit. Their findings also revealed that lubricant choice and surface finish are more significant parameters than were previously believed.

Reichenbach et al. [24] carried out some early work on the high-temperature frictional behavior of silicone, mineral, and ester lubricants. They reported that lubrication failure was achieved at different temperatures for all lubricants, and oil-air mist lubrication failed at significantly lower temperatures. The research highlighted that volatility and deposition properties of lubricants must be considered in the design of high-speed bearing lubrication systems.

Gao et al. [10] added thermal expansion and starvation lubrication to their KH-TEHD model. Simulated as well as experimental findings showed that the thermal deformation of the bearing raceway could be up to 4× larger than normal clearances under starvation. They also confirmed that cage-guide hydrodynamic pressure must be considered in the

accurate simulation of cage motion and overall thermal stability, especially at high speeds.

Considered collectively, these researches demonstrate that lubrication should not be treated as a passive boundary condition but must be modeled dynamically along with structural deformation, contact response, and thermal expansion in order to describe its full influence on bearing friction, temperature, and reliability. Furthermore, advanced modeling methods involving surface texture, vibration response, and lubricant film formation shed insight on real bearing performance and direct the design of enhanced thermal management and lubrication systems.

2.6 Material Behavior and Fatigue Life Modeling

The choice of bearing material has a significant influence on load-carrying capacity, stiffness, wear life, and fatigue life, especially for conditions of high load and speed. Traditional materials such as alloy steels remain popular due to their established mechanical properties and high stiffness. However, with increasing demands for high-performance in aerospace and precision industrial applications, alternative materials such as nickel-based superalloys and titanium alloys are now also being explored for their improved thermal and fatigue properties under highly specified operating conditions.

Wang et al. [25] conducted a theoretical study to analyze the impact of wear-induced clearance variation and radial deflection on bearing mechanics and fatigue life. Their results indicated that wear-induced increase in radial clearance decreases stiffness, which has a contributory impact on higher stress concentration and reduced fatigue life. Their study also found that preload clearance plays a vital role in life prediction and that optimum preload values are based on the elasticity and wear resistance of a material. This study provides a good basis for incorporating wear evolution into fatigue modeling.

Shi et al. [22] created a new relative fatigue life model integrating quasi-dynamics, micro-TEHL analysis, surface texture simulation, and theoretical stress modeling. They confirmed that transverse surface textures increased fatigue life by promoting hydrodynamic film formation, while longitudinal textures, high skewness, and high

kurtosis reduced it. They recorded a 3.9% disparity in predicted and experimental maximum stress values, validating the precision of their integrated algorithm. This research emphasizes the importance of including surface roughness parameters in fatigue life prediction, particularly under high-speed conditions.

Gao et al. [13] introduced an analytical fatigue life model based on an enhanced raceway control theory. Incorporating thermal deformation and centrifugal displacement, their model captured ball-raceway contact variation more effectively under axial and combined loading. They showed that clearance variation significantly influences dynamic behavior and fatigue life and that conventional models omitting these factors tend to overestimate or underestimate service life. Their model is a valuable design engineering tool for predicting bearing lifespan under actual thermal and mechanical conditions.

Chunjiang et al. [14] indirectly but significantly contributed to fatigue modeling by showing the speed and axial force variation of gyroscopic torque and friction coefficients, which influence internal load distribution. Due to fatigue life being very sensitive to contact load cycles and angular variations, such knowledge is required to improve the accuracy of life prediction, especially at high speeds where dynamic imbalance is significant.

Temperature contribution to the degradation of fatigue is also considerable. Gao et al. [10] in their research proved that thermal deformation within the raceway can surpass clearance during lubrication starvation, resulting in abnormal stress, wear, and fatigue. Their findings present that the fatigue life of a bearing is not only governed by the bearing's material strength or loading history but also thermal performance, lubrication reliability, and structural stability under dynamic operation.

On a material basis, titanium alloys have shown superior light-load fatigue life due to lower density and greater elasticity. Again, however, Wang et al. [25] described, as their fatigue performance deteriorates very rapidly at increased load and speed, and they are less well suited to heavy-duty use. Alloy steels, in contrast, show stable fatigue resistance over a wider range of loads but are subject to thermal degradation if there is too little lubrication or cooling. Nickel-based superalloys lie between these two extremes of performance—offering good fatigue endurance and superior resistance to steels at high temperature, but at greater material cost.

In conclusion, the literature considered here demonstrates that ACBB fatigue life modeling is a problem of multiphysics that must account for contact mechanics, lubrication regime, material properties, surface texture, and thermal effects. Current computational models combining TEHL simulations, stress analysis, and material-dependent wear behavior present a satisfactory framework for service life prediction under various conditions and bearing design optimization.

2.7 Defect Modeling and Failure Mechanisms

Surface imperfections in angular contact ball bearings (ACBBs), particularly localized surface defects in the form of spalls, pits, or cracks on the raceways, are one of the primary sources of compromised performance and failure. These imperfections alter the customary load transmission, modify the contact mechanics, and generate abrupt force and vibration responses. Accurate modeling of defect-induced dynamics is therefore imperative for efficient diagnostics, predictive maintenance, and life prediction.

Wen et al. [11] introduced a comprehensive multi-degree-of-freedom (DOF) dynamic model for ACBBs with outer raceway defects. Contrary to previous studies that considered defects to be periodic excitations, they incorporated the geometry of the defect into the constraint equations directly, being more physical. Defects, in their study, had a significant impact on angular misalignments, induced oscillations in contact forces, and generated ball-pocket impacts—especially at the defect exit. The magnitudes of these effects depend on defect size, position, load condition, and speed. This work introduced one of the most comprehensive descriptions of defect impact on tribo-dynamic performance.

Kong et al. [26] developed a vibration model suitable for defect detection by integrating Hertzian contact theory and relative motion analysis of bearing components. The model was designed for transient contact force prediction of the ball in passing through a localized defect in which elliptical contact area and stress distribution were taken into account. Experimental verification of vibration signal indicated close conformity, validating the ability of the model to reproduce the defect-induced vibration's characteristic features. This work solidified the importance of accurate contact stress modeling in early-stage defect detection.

Liu et al. [27] addressed the defect and edge evolution shape in cylindrical roller bearings, which is directly related to ball bearing dynamics. They further showed that the sharp-edged rectangular models applied to calculations cannot represent the true nature of defect-induced dynamics. Their work initiated new paths in model development for defect edge evolution and subsequent vibration and contact stiffness. Though the study was conducted on roller bearings, its result is applicable to ACBBs and presents a helpful conclusion regarding the way defect geometry can reshape system response.

Xu et al. [16] proposed a new dynamic skidding and fault modeling that also accounted for the effect of bearing clearance and sliding caused by defects. They measured levels of cage velocity fluctuation through a synchronous differential encoder (SDE) system to detect skidding and the severity of defect. Using their results, they confirmed that, in addition to affecting the skidding behavior, bearing clearance also increases the vibration signature of the defect and thus is an important factor in fault modeling.

Mishra et al. [12] proposed a hierarchical modeling approach to model faulty bearing vibration signals through models with different complexity levels. Such detailed spatial multi-body models with contact and traction dynamics alone were able to mimic the complex spectral features of actual faulty bearings. This once again validated the need for high-fidelity dynamic models in the practice of condition monitoring.

In summary, the literature indicates that defect modeling in ACBBs should not be restricted to idealized cyclic excitation hypotheses. Geometric fidelity, propagation of stress waves, variation of contact force, and vibration response are all shared priorities for realistic analyses. Bearing clearance, cage interactions, and lubrication condition are also significant factors in the dynamic response to defects. Advanced modeling methodologies, supported by prior experimental evidence, are powerful tools for defect detection, prognosis, and health monitoring system design in high-speed rotating machinery.

2.8 Cage Dynamics and Stability

A cage (or retainer) of an angular contact ball bearing (ACBB) performs the critical task of rolling element spacing and motion guidance. While significant, cage dynamics

have been a lower research priority topic than raceway/rolling element interactions. Recent investigations have demonstrated, however, that cage instability—through ball-pocket impact, asymmetric forces, or lubrication nonuniformities—can generate skidding, enhanced vibration, and even premature bearing failure. With the higher bearing speeds and more varied lubrication conditions, it is now critical to model cage behavior accurately.

Gao et al. [28] introduced a high-fidelity cage-centered dynamic model of ACBBs for aeronautical applications. Due to the low stiffness of porous polyimide cage materials used, the model partitioned the cage into Nb segments (equal to the number of balls) and assigned 4×Nb degrees of freedom to balls and Nb+3 DOF to the cage. The model considered translational and axial whirling motion and accounted for ball-pocket normal/tangential forces, axial impacts, and hydrodynamic pressure between guide ring and cage. Through high-speed camera experiments, they verified the model prediction of the cage whirl radius and stability for different speeds and axial loads. According to their results, cage whirl amplitude is reduced by increasing axial load, while radial loads aggravate the instability due to guide-ring rubbing.

Wen et al. [11] further identified cage-pocket collisions as a direct consequence of surface defect and dynamic loading. The multi-DOF model of theirs demonstrated that a ball entering a defect region would lose contact with the raceway for a transient period and regain contact abruptly, imparting impact forces onto the cage. This results in reciprocating impacts that are intensified at lower speeds and larger defect sizes. Under conditions of no defects, combined axial-radial loading may trigger these impacts, destabilizing cage motion and causing local heating and wear.

Gao et al. [9, 10] also established that cage dynamics are strongly related to overskidding. With their KH-THD and KH-TEHD models, they illustrated that overskidding leads to an error in cage speed in real and theoretical senses, initiating ball-raceway separation and oscillatory cage-ball contacts. Incomplete or starved lubrication contributes by causing frictional heating and reducing the damping forces at the cage interface. They significantly determined that thermal expansion and hydrodynamic pressure in the space of cage-guide ring clearance cannot be neglected and must be accounted for to be able to make reasonable cage stability predictions. Xu et al. [16] introduced an empirical method of online cage motion measurement using a

synchronous differential encoder (SDE) system. In their experiments, they confirmed that the greater the bearing clearance, the greater the cage skidding and the greater the angular velocity deviations. These dynamic variations, when measured and analyzed, reveal important indications of cage instability and can be used for fault detection in its early stage. From a modeling point of view, cage behavior is far from being independent but is influenced by rolling element dynamics, preload, lubrication regime, and even thermal gradients. Simulation of cage dynamics must accommodate effects such as centrifugal forces, cage-bore and cage-pocket friction, lubricant film interaction, and elastic deformation to provide any realistic description. In addition, cage instability tends to spread in the system and causes vibration to grow and bearing life to diminish. Collectively, the literature emphasizes that we have to treat the cage as an active dynamic member, and not as a passive structural member. Its defect response, stability, and lubricant film interaction are of paramount concern in designing dependable high-speed ACBBs—particularly in harsh applications such as aerospace turbines, precision spindles, and electric motor drives.

2.9 Summary and Research Gaps

This chapter has reviewed the extensive body of literature focused on the dynamic, thermal, tribological, and structural behavior of angular contact ball bearings (ACBBs). Significant advancements have been made in modeling and simulation techniques, which now integrate multiple physical phenomena, including contact mechanics, elastohydrodynamic lubrication (EHL), thermal expansion, and material-specific fatigue behavior. However, several important themes and limitations emerge from this review.

Dynamic modeling has evolved from quasi-static approximations to advanced multi-body, multi-DOF models that incorporate complex interactions between rolling elements, cage, lubricant, and raceways. Models such as KH-THD and KH-TEHD have successfully captured the coupled effects of kinematics, heat generation, and lubrication, improving prediction accuracy under high-speed conditions. Despite these improvements, most models still require experimental validation across a wider range of operating conditions, especially in the presence of dynamic loads and lubricant starvation.

The phenomenon of skidding and overskidding, once overlooked, is now recognized as a critical issue in high-speed bearings. Studies have demonstrated that improper preload, excessive clearance, or inadequate lubrication can lead to skidding, which exacerbates wear and elevates thermal stresses. While minimum axial load thresholds have been identified for skidding mitigation, there remains a need to develop generalized skidding criteria that account for varying geometries, materials, and loading scenarios.

Preload optimization has been widely addressed, with research confirming that both under- and over-preloading degrade bearing life. New analytical and simulation-based methods offer promising tools for preload tuning, yet many of these still rely on idealized assumptions. Real-world conditions—such as non-uniform preload, manufacturing tolerances, and temperature gradients—remain underexplored, especially in transient operating environments.

Lubrication and thermal behavior have emerged as dominant factors in bearing degradation and failure. TEHL modeling has greatly improved understanding of film thickness behavior, power loss, and frictional heating. However, most models treat lubrication as uniform and stable, which may not reflect actual conditions in high-speed or starved lubrication regimes. Moreover, interactions between vibration, lubricant rheology, and surface roughness need further experimental and computational investigation.

In terms of material behavior and fatigue life, studies have shown that titanium alloys outperform traditional steels under light loads, while alloy steels and nickel-based superalloys offer better performance in heavy-load applications. Yet, fatigue life models often neglect the synergistic effects of material microstructure, surface finish, and lubrication condition—all of which can critically influence subsurface stress distribution and crack initiation.

Defect modeling has become more realistic with the inclusion of geometric defect profiles, contact stiffness variation, and localized vibration responses. Nevertheless, most models assume isolated or predefined defects and rarely account for defect evolution over time or the influence of debris, surface fatigue, and real-time wear. Integrating defect growth models with health monitoring data remains an open challenge.

Finally, cage dynamics have gained prominence in recent research, especially for aerospace-grade bearings with lightweight, low-stiffness cage materials. Whirl instability, cage-pocket collisions, and cage-guide lubrication effects all play a significant role in bearing stability but are often simplified or ignored in system-level simulations. Future studies should develop more comprehensive, cage-inclusive models and validate them under various thermal and lubrication regimes.

Identified Research Gaps

Insufficient integration of EHL, heat generation, and contact mechanics in conventional models like the Harris model. Most legacy models neglect transient lubrication film dynamics and thermal expansion effects, leading to inaccurate predictions under high-speed, high-load conditions.

- Lack of coupled multiphysics models that simulate inner and outer raceway contact behavior under realistic operating conditions. Existing studies rarely provide detailed comparisons of contact load distribution, contact angles, and friction torque at varying speeds and loads using a novel mathematical and theoretical coupled model.
- Limited exploration of fatigue life prediction with respect to material type (e.g., alloy steels, titanium alloys, and nickel-based superalloys) under varying speed and load regimes. Few models directly relate material stiffness, contact load, and dynamic capacity to bearing fatigue degradation in a coupled simulation framework.
- Underrepresentation of centrifugal and gyroscopic effects in fatigue life and contact force redistribution, particularly in models evaluating bearing performance beyond 10,000–15,000 RPM.
- Neglect of thermal transience and local heat generation effects, especially due to spinning and viscous friction, in many conventional and semi-analytical models.
- Inadequate modeling of friction torque breakdown, where load-dependent, spin-induced, and viscous components are not treated as separate contributors to total

power loss and heat generation, limiting the accuracy of thermal behavior predictions.

- Scarce comparative analysis between classical and advanced bearing models, particularly regarding their predictions on contact loads, angles, friction torque, and fatigue life — which this study addresses through comprehensive validation of the new FE-based model against the Harris model.

Chapter 3: Theoretical analysis of rolling bearing

Roller and ball bearings support loads with rotational and translational movement. Unlike hydrodynamic bearings, rolling bearings have complex inner dynamics, e.g., element and shaft rotation, orbital movement, and sliding contact. Non-zero contact angles at high-speed produce spinning, gyroscopic effects, and greater inner speeds—especially for lubricated angular contact ball bearings [13]. These increase the centrifugal forces and the gyroscopic moment's effect on inner forces and deflection and stiffening the supported-load distribution.

This chapter presents the theoretical foundation of a novel mathematical and theoretical coupled model developed for the analysis of angular contact ball bearings (ACBBs) under high-speed and heavy-load conditions, also derives a model of such inner dynamics: the action of skidding, centrifugal forces, and the gyroscopic motion. Simplifying assumptions, i.e., "outer raceway control" and distribution of the gyroscopic moment, are made to compute inner forces and deflection economically under high-speed, thrust-loaded running. While the individual equations and formulations presented in this chapter are drawn from established theories and prior works—including the classical Harris model [29], Jones' raceway control theory [30], elastohydrodynamic lubrication (EHL) theory [11],and principles of heat transfer and fatigue life estimation—the original contribution of this thesis lies not in the derivation of new standalone equations, but in the systematic integration and computational implementation of these interacting physical phenomena into a unified, coupled numerical framework.

- **Coupled Model:** The term "coupled" refers to a modeling approach in which multiple physical domains—in this case, mechanical, thermal, and tribological—are solved simultaneously within an integrated numerical framework. The coupling captures essential cause-and-effect relationships: for example, the mechanical load distribution determines frictional heat generation; this heat causes thermal expansion of bearing components; the altered dimensions and clearances, in turn, change the lubricant film thickness and stiffness, which feeds back to modify the mechanical load distribution. This

bidirectional interdependence is solved iteratively until a converged state of equilibrium is reached for the entire system.

- **Theoretical Model:** This descriptor pertains to the physics-based foundation of the work. The theoretical model is composed of established principles and constitutive equations drawn from solid mechanics, fluid dynamics, and thermodynamics. These include Hertzian contact theory, elastohydrodynamic lubrication (EHL) equations, laws of heat generation and transfer, and fatigue life theory. The "theoretical" aspect signifies that the model's structure is derived from first principles and physical laws rather than empirical fitting.
- **Mathematical Model:** This term refers to the numerical implementation of the theoretical framework. It involves the translation of continuous physical equations into discrete, solvable numerical forms. This includes the application of algorithms such as the Newton-Raphson method for solving nonlinear equilibrium equations, iterative loops for thermal coupling, and numerical integration techniques. The "mathematical" aspect emphasizes the computational strategies employed to obtain quantitative solutions from the theoretical system of equations.

Rationale for the Combined Description: The proposed framework is accurately described as both a theoretical and a mathematical coupled model. It is theoretical because it is rooted in physical laws; it is mathematical because these laws are formulated into a solvable numerical system; and it is coupled because the system solves the interacting physical phenomena concurrently. This integrated approach is what enables a more realistic simulation of bearing behavior under complex operating conditions than is possible with sequential or decoupled analyses.

The proposed model advances beyond conventional bearing analysis in two principal ways:

1. **Integrated Multi-Physics Coupling:** Traditional models, such as the Harris model, often treat mechanical loading, lubrication, and thermal effects in a decoupled or simplified manner. In contrast, the model developed

here explicitly couples the following key phenomena within a single iterative numerical scheme:

- **Mechanical Load Distribution:** Based on Hertzian contact theory and raceway geometry, accounting for centrifugal and gyroscopic forces at high speeds.
- **Interference Fit and Assembly Effects:** Incorporating initial changes in contact angle and clearance due to press-fit installation (Section 3.1).
- **Elastohydrodynamic Lubrication (EHL):** Modeling the effects of a variable lubricant film on contact stiffness and load transmission, where film thickness is a function of speed, load, and temperature (Section 3.2).
- **Dynamic High-Speed Effects:** Including centrifugal forces, gyroscopic moments, and the conditions for skidding, which significantly alter internal load distribution at elevated rotational speeds (Section 3.3).
- **Thermal Generation and Dissipation:** Coupling frictional heat generation (from load, spin, and viscous effects) with a simplified thermal network model to predict component temperatures, which in turn affect material properties, clearances, and lubricant viscosity (Section 3.5).
- **Fatigue Life Prediction:** Utilizing the dynamically calculated contact loads and angles—which are themselves influenced by thermal and lubrication states—to estimate bearing life via enhanced load-capacity formulas (Section 3.6).

The coupling is achieved through an iterative solution procedure. For a given applied load and rotational speed, the model simultaneously solves for mechanical equilibrium, updates lubricant film stiffness based on current loads and speeds, calculates the resulting frictional heat, estimates the temperature rise, and feeds the thermal expansion data back into the geometric and clearance calculations. This closed-loop process,

illustrated in Figure 3.12, continues until convergence in both mechanical forces and thermal state is achieved.

2. **Computational Implementation for Extended Operational Envelopes:** The second key contribution is the implementation of this integrated model within a robust computational environment (MATLAB). This implementation enables the simulation of ACBB behavior under extreme operating conditions—specifically, speeds up to 15,000 RPM and axial loads up to 47.5 KN—which are representative of aerospace gas turbine main shaft bearings but are often beyond the predictive scope of the uncoupled Harris model. The numerical framework handles the nonlinearities and interdependencies inherent in the coupled system, allowing for a more accurate prediction of:
    - Contact load distribution between inner and outer raceways.
    - Variation of contact angles with speed and load.
    - Breakdown of friction torque into load-dependent, spinning, and viscous components.
    - Heat generation rates and their partition between raceways.
    - Fatigue life considering the combined influence of dynamic loading, thermal stresses, and lubricant film effects.

3.1. Initial angles change due to bearing interference fit

An interference fit, often referred to as a press fit, is a tight fit when a bearing is inserted into a housing or onto a shaft. [29]. This creates a pre-load that can alter the initial bearing angle [31]. The interference fit reduces the effective clearance of the bearing, which can lead to changes in the contact angle and endplay [32].This alteration can affect the bearing's performance and lifespan [18].

Practically, when a bearing is installed with an interference fit, it means the bearing is slightly larger than the bore it’s being inserted into [33]. This requires force to fit, which alters the initial angle and can induce stress and deformation. This fit creates a very tight connection that can withstand high loads and reduce movement but also impacts

on the bearing's alignment and geometry [34]. The tightness or looseness between an assembly's mating elements is the word used in engineering to describe fit. Shafts and holes are often the mating pieces. In general, fits fall into three categories. In rotor machinery applications, clearance fit, interference fit, and transition fit are often used kinds [35].

The initial bearing angle during installation is altered as a result of interference fit. Furthermore, at high speeds, the bearing's internal motion becomes complex, friction raises the internal temperature, causing the bearing to expand and deform, and its dynamic properties change dramatically [30].

Figure 3.1 depicts the ball bearing in its most basic configuration. It is clear that the average of bore and outside diameters is about the same as the bearing pitch diameter, dm. Clearance is frequently considered in the design, the diametral clearance, P_d, in Figure 3.1.

The Jones model [30], which is a somewhat comprehensive bearing analysis model, does not take temperature-induced displacement, centrifugal force, or interference fit into account. However, it is challenging to distinguish between different Jones control theories. The following establishes the interference fit and thermal expansion due to the temperature difference between the shaft and inner ring as well as between the outer and housing rings [29].

$$d_m = \frac{1}{2}(d_i + d_o) \quad (1)$$

$$P_d = d_o - d_i - 2D \quad (2)$$

$$f_i = \frac{r_i}{D} \quad (3)$$

$$f_o = \frac{r_o}{D} \quad (4)$$

$$A = r_o + r_i - D \quad \textbf{Or} \quad A = BD \quad (5)$$

$$B = f_i + f_o - 1 \quad (6)$$

$$\alpha^\circ = cos^{-1}\left(1 - \frac{P_w}{2A}\right) \quad (7)$$

$$P_w = P_d + \Delta P_d \quad (8)$$

$$\Delta P_d = -\Delta_r - \Delta_h \quad (9)$$

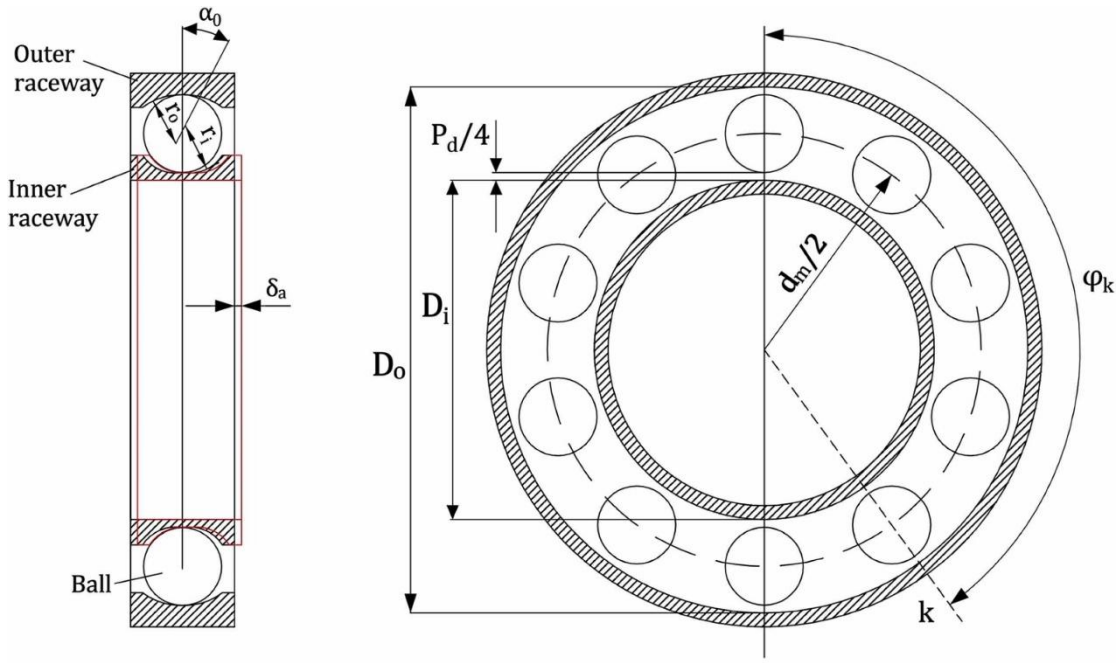

Figure 3.1: An angular contact ball bearing's cross section [13]

The rolling bearing inner ring diameter change results from pressure fit could be calculated through Harris model as [29]:

$$\Delta_r = \frac{2I_s\left(\frac{d_i}{D_b}\right)}{\left[\left(\left(\frac{d_i}{D_b}\right)^2\right)-1\right]\left\{\left[\frac{\left(\left(\frac{d_i}{D_b}\right)^2\right)+1}{\left(\left(\frac{d_i}{D_b}\right)^2\right)-1}+\xi_i\right]+\frac{E_i}{E_s}\left[\frac{\left(\left(\frac{D_b}{D_s}\right)^2\right)+1}{\left(\left(\frac{D_b}{D_s}\right)^2\right)-1}-\xi_s\right]\right\}} \tag{10}$$

$$I_s = I_0 - \Delta I_c - \Delta I_T \tag{11}$$

From tables in ref. [29] the bearing initial installation interference I_0 can be found. The inner ring and shaft interference reduces because of the excessive speed in the real conditions [29]. This change can be calculated as follows:

$$\Delta I_c = \Delta D_s - \Delta D_i \tag{12}$$

$$\Delta D_i = 3.13 \times 10^{-11} \times \frac{\mathfrak{D}_i \omega^2 (D_b + d_i)^3}{E_i} \tag{13}$$

$$\Delta D_s = 3.13 \times 10^{-11} \times \frac{\mathfrak{D}_s \omega^2 (D_b + D_s)^3}{E_s} \tag{14}$$

where $\boldsymbol{\omega}$ is the rotational velocity, $\mathfrak{D}_i$ denotes inner ring density, and $\mathfrak{D}_s$ denotes the one of the axis. In addition, temperature has an impact on the interference fit change.

Temperature increases and thermal deformation occurs while the bearing is operating at high speed. The change in fit is determined by the bearing thermal expansion coefficient. The following is an expression for the temperature-induced change in inner ring interference fit:

$$\Delta I_T = \Gamma_i \Delta T_i D_i - \Gamma_s \Delta T_s D_s \tag{15}$$

Representing the bearing temperature rise for inner ring and shaft, respectively, are ΔTi and ΔT_s. The thermally expansion coefficient is represented by, K_i and K_s. In the same way, interference fit reduces the outer ring diameter [29]:

$$\Delta_{\boldsymbol{h}} = \frac{2\boldsymbol{I_h}\left(\frac{D_o}{d_o}\right)}{\left[\left(\left(\frac{D_o}{d_o}\right)^2\right)-1\right]\left\{\left[\frac{\left(\left(\frac{D_o}{d_o}\right)^2\right)+1}{\left(\left(\frac{D_o}{d_o}\right)^2\right)-1}+\xi_o\right]+\frac{E_o}{E_h}\left[\frac{\left(\left(\frac{D_h}{D_o}\right)^2\right)+1}{\left(\left(\frac{D_h}{D_o}\right)^2\right)-1}-\xi_h\right]\right\}} \tag{16}$$

$$\Delta\psi = \frac{2\pi}{Z}, \psi_j = \frac{2\pi}{Z(j-1)} \tag{17}$$

$$I_h = I_0 - \Delta I_c - \Delta I_T \tag{18}$$

$$\Delta I_c = \Delta D_o - \Delta D_h \tag{19}$$

$$\Delta D_o = 3.13 \times 10^{-11} \times \frac{\mathfrak{D}_o {\omega_o}^2 (D_o + d_o)^3}{E_o} \tag{20}$$

$$\Delta D_h = 3.13 \times 10^{-11} \times \frac{\mathfrak{D}_h {\omega_o}^2 (D_h + D_o)^3}{E_h} \tag{21}$$

$$\Delta I_T = \Gamma_o \Delta T_o D_o - \Gamma_h \Delta T_h D_h \tag{22}$$

3.2. Bearing clearances and oil film's effects on bearing contact

Fluid lubrication is essential for ball and roller bearings to function properly over extended periods of time. Dry film lubricants, such as molybdenum disulfide, provide appropriate protection for modern rolling bearings under the high pressure, vacuum, and temperature extremes seen in aerospace applications. However, these bearings have not been submitted to stringent criteria for heavy-duty and fatigue-free operation. It is also known that only a small amount of lubricants are needed for exceptional

performance when there is no high temperature present. As a result, a lot of rolling bearings can be filled with greases that contain very little oil, and the lubricant can be kept in place by mechanically sealing them. These rolling bearings often carry out their necessary tasks for lengthy periods of time [17].

Bearings may overheat and "burn" if they are lubricated with too much oil or grease. It didn't come until the end of the 1940s that the lubrication process of rolling elements in close proximity to a raceway was analytically confirmed, and it was not until the early 1960s that it was demonstrated experimentally. This is analogous to Reynolds' discovery of hydrodynamic lubrication in journal bearings in the 1880s. In a well-designed bearing, for instance, it is well acknowledged that a fluid layer completely isolates the bearing surface from the journal or slider surface. Furthermore, any fluid that has enough viscosity for the intended purpose—such as oil, water, gas, or another material—can be used as a lubricant [36]. However, fluid films have only recently been shown to successfully separate rolling surfaces that are subjected to extremely high pressures in rolling bearing contact zones. Rolling bearings with lubricating fluid layers have been shown to efficiently separate rolling surfaces in a variety of successful applications.

Several researchers have used classical hydrodynamic theory to study the hydrodynamic effect of lubricants on rolling bearings, since it was probable that, under particular load and speed circumstances, lubricant films of considerable amounts did develop in the contact zones. As early as 1916, Martin [37] suggested a fix for stiff rolling cylinders. Osterle looked at a roller bearing assembly's hydrodynamic lubrication in 1959 [38].

Under Electrohydrodynamic lubrication (EHL) theory [11]; The minimum oil film thickness, $h_{min}^{i,o}$, and its stiffness, $K_{oil}^{i,o}$, for the elliptical contact EHL under isothermal circumstances, may be computed by:

$$h_{min}^{i,o} = 3.63\bar{U}_{i,o}^{0.68} G^{0.49} Q_Z^{-0.073}\left(1 - e^{-.068k}\right) \quad (23)$$

$$K_{oil}^{i,o} = \frac{dF}{dh_{min}^{i,o}} \quad (24)$$

$$K_{oil}^{i,o} = 6.4066 \times 10^8 \, h_{min}^{-14.6986} \, \bar{U}^{9.3157} \, G^{6.7123} \, \acute{E} \, {R_x}^{15.6986}\left(1 - e^{-0.68k}\right)^{13.6986} \quad (25)$$

Where $\overline{U}$ is the dimensionless velocities parameter, $\overline{U} = \frac{\eta_o U_{i,o}}{2\acute{E}R_x}$, Between the rolling and raceway, the corresponding radius of curvature is Rx, ellipticity is represented by $\mathcal{k}$, and the material parameter, G, is equal to $\lambda E'$. Between the roller and raceway, the fluid is swept into the rolling element–racetrack contacts at the lubricant entrainment velocity as follows [17]:

$$U_i = \frac{d_m}{2}[(1-\gamma)(\omega - \omega_m) + \gamma\omega_R] \quad (26)$$

$$U_o = \frac{d_m}{2}[(1+\gamma)\omega_m + \gamma\omega_R] \quad (27)$$

$$v_o = 2.26.10^{-3} SSU - \frac{1.95}{SSU} \quad (28)$$

$$\eta_{b=v_b\rho_{oil}\mathcal{G}} \quad (29)$$

From [39] , data for a typical mineral oil at nominal temperatures, equation (λ) gives the pressure coefficient of viscosity.

$$Q_z = \frac{Q}{E\prime {R_{xi}}^2} \quad (30)$$

$$\lambda = 0.1122\left(\frac{v_o}{10^4}\right)^{0.163} \quad (31)$$

$$R_{xi} = \frac{D}{2}(1-\gamma) \quad (32)$$

$$R_{xo} = \frac{D}{2}(1+\gamma) \quad (33)$$

$$E' = \frac{E}{1-\xi^2} \quad (34)$$

Where, Pitch diameter is represented by dm, parameters equal to D/d_m, inner race angle velocity by ω, orbital angle velocity by ω_m, and self-rotating angle velocity by ω_R.

$$K_{i,o} = \frac{K_H^{i,o} K_{oil}^{i,o}}{K_H^{i,o} + K_{oil}^{i,o}} \quad (35)$$

$$K_H^{i,o} = \frac{2\sqrt{2}\left(\frac{E}{1-\xi^2}\right)}{3(\sum\rho)^{1/2}}\left(\frac{1}{\delta^*}\right)^{\frac{3}{2}} \quad (36)$$

Young's modulus, contact deflection, curvature sum, and Poisson's ratio are shown by the symbols $\boldsymbol{E}$, $\boldsymbol{\delta}*$, $\boldsymbol{\rho}$, and ξ, while the mass of each rolling ball is indicated by $\boldsymbol{m_b}$.

3.3. Dynamic model for High-speed conditions

In order to allow the shaft or slider to rotate and translate, bearings are designed to support a range of loads. Rolling bearings can move in more intricate ways than

hydrodynamic or hydrostatic bearings. While the bearing is installed on a shaft rotating at n rpm, the rolling components rotate around the bearing axis at n rpm and around their own axes at n_m. Along with the rolling motions, the contact zones also experience some sliding. Rolling and spinning motion happen concurrently if the balls' and raceways' contact angles are not zero, as they are in ball bearings other than basic radial bearings. Additionally, gyroscopic pivotal motions take place, especially in ball bearings that are lubricated with oil and grease. Internal rotational speeds of rolling bearings and relative velocities, or sliding velocities, will be examined in this part of our thesis, and the mathematical formulas for their subsequent computation will be written for high speed, centrifugal force, kidding effects, and gyroscopic moment in a thrust load angular contact ball bearing. When ball and roller bearings run at high speeds, the centrifugal forces of the rolling element are much greater than the forces acting on the bearing.

Based on the angles of contact, high-speed ball bearings can have quite substantial ball centrifugal forces and ball gyroscopic moments. As a result, angles often get smaller in the outside raceway and rise in the inner racetrack. This has an effect on the bearing's deflection versus load characteristics, which in turn has an impact on the rotor system dynamics that the ball bearing supports. The lubrication properties and, consequently, the friction in ball and roller bearings are likewise impacted by high speed. The rolling element's inertial loading, gyroscopic moments, and centrifugal forces will alter as a result of the internal bearing speeds. In many high speed rolling bearing applications, the internal distribution of load and, hence, stresses, may be accurately assessed without taking the rolling components' frictional loading into account. However, this work illustrates friction impacts including skidding affects of the distribution of internal loads.

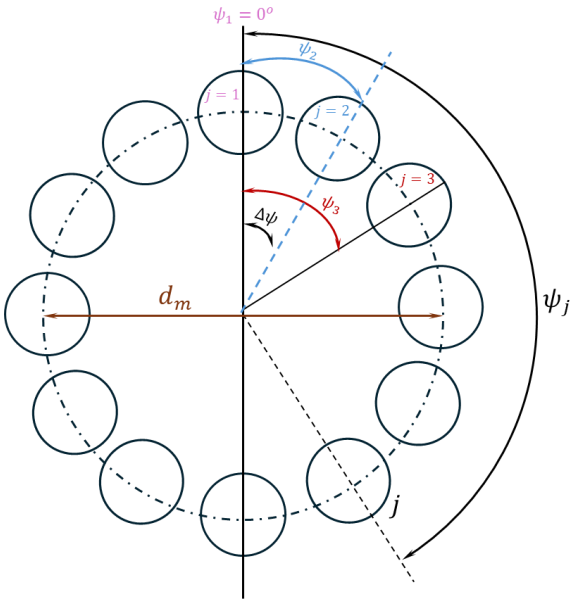

Figure 3.2: Rolling elements angular positions in ψz plane [29]

If noncoplanar friction forces are small, the load diagram of Figure 3.2 is generated by considering the plane that intersects the bearing axis and the center of a ball at azimuth ψ_j. It is also feasible to assume that "outer raceway control" is approximated at a certain ball location, where frictional force entirely resists the gyroscopic moment of the ball at the contact with the outer raceway. This assumption has minimal impact on the computations' correctness. Therefore, for "outer raceway control" in Figure 3.3, $\lambda_{ij}=0$ and $A_{oj}=2$; otherwise, $\lambda_{ij}=\lambda_{oj}=1$.

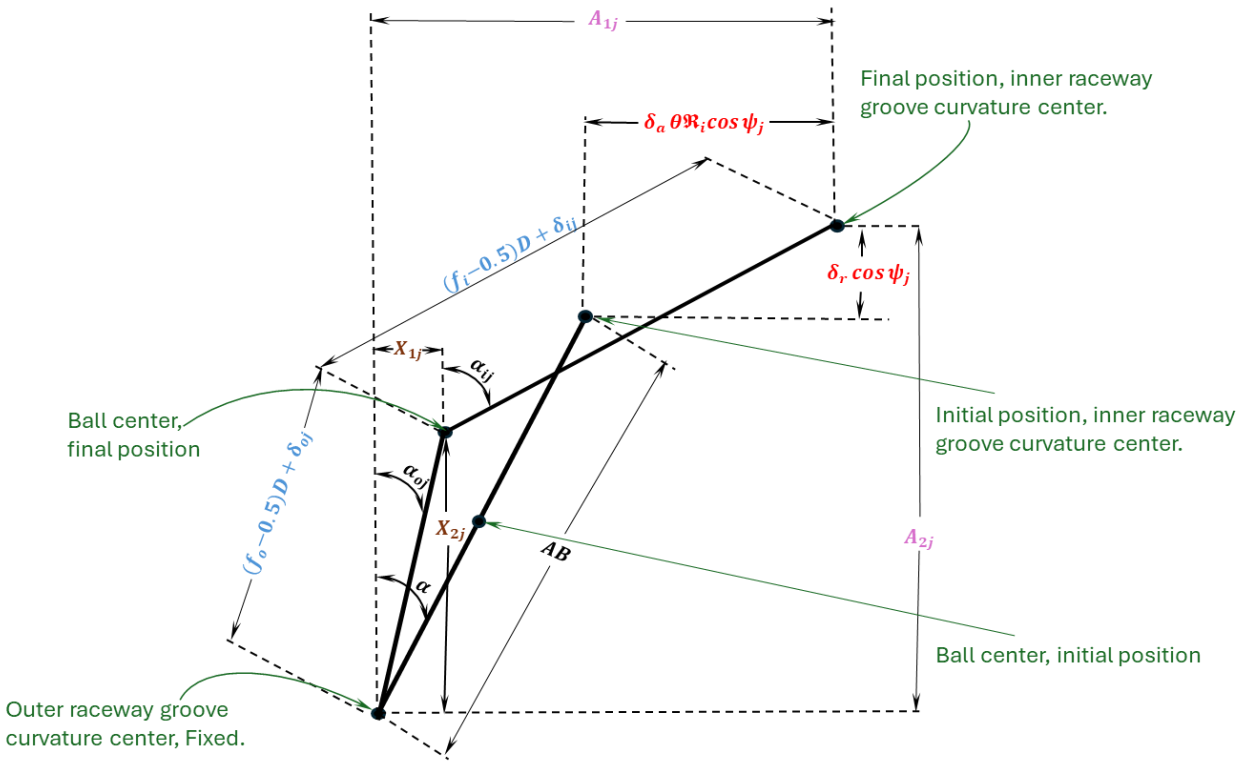

Figure 3.3: Positions of the raceway groove curvature centres and ball centre at angular position ψ, both with and without load applied [29]

Where the first contact angle before loading is α^o and inner raceway groove curvature centers' radius is $\boldsymbol{R_i}$ which is written in the following formula:

$$\boldsymbol{R_i} = \frac{d_m}{2} + (r_i - 0.5D)\,cos\,\alpha^o \tag{37}$$

Additionally, the axial separation at each ball position between the inner and groove centers is defined by the corresponding angular displacements θ and the inner and outer rings' respective axial displacements δ_a.

$$A_{1j} = AB\,sin\,\alpha^\circ + \delta_a + \theta\Re_i\,cos\,\psi_j \tag{38}$$

A relative radial displacement of the ring centers δ_r is used to determine the radial displacement.

$$A_{2j} = AB\,cos\,\alpha^\circ + \delta_r\,cos\,\psi_j \tag{39}$$

$$cos\,\alpha_{oj} = \frac{X_{2j}}{(f_o-0.5)D+\delta_{oj}} \tag{40}$$

$$sin\,\alpha_{oj} = \frac{X_{1j}}{(f_o-0.5)D+\delta_{oj}} \tag{41}$$

$$cos\,\alpha_{ij} = \frac{A_{2j}-X_{2j}}{(f_i-0.5)D+\delta_{ij}} \tag{42}$$

$$sin\,\alpha_{ij} = \frac{A_{1j}-X_{1j}}{(f_i-0.5)D+\delta_{ij}} \tag{43}$$

It can be found by using the Pythagorean theorem Figure 3.3 the following equations:

$$\left(A_{1j}-X_{1j}\right)^2 + \left(A_{2j}-X_{2j}\right)^2 - \left[(f_i-0.5)D+\delta_{ij}\right]^2 = 0 \tag{44}$$

$$X_{1j}^2 + X_{2j}^2 - \left[(f_o-0.5)D+\delta_{oj}\right]^2 = 0 \tag{45}$$

$$Q_{ij}\,sin\,\alpha_{ij} - Q_{oj}\,sin\,\alpha_{oj} - \frac{M_{gj}}{D}\left(\lambda_{ij}\,cos\,\alpha_{ij} - \lambda_{oj}\,cos\,\alpha_{oj}\right) = 0 \tag{46}$$

$$Q_{ij}\,cos\,\alpha_{ij} - Q_{oj}\,cos\,\alpha_{oj} + \frac{M_{gi}}{D}\left(\lambda_{ij}\,sin\,\alpha_{ij} - \lambda_{oj}\,sin\,\alpha_{oj}\right) + F_{cj} - G\,sin\,\psi_j = 0 \tag{47}$$

The only thing left to do is determine the equilibrium conditions applied to the entire bearing in order to determine the values of δ_a, δ_r, and θ. These are:

$$F_a - \sum_{j=1}^{j=Z}\left(\frac{K_{ij}(A_{1j}-X_{1j})\delta_{ij}^{1.5} - \frac{\lambda_{ij}M_{gi}}{D}(A_{2j}-X_{2j})}{(f_i-0.5)D+\delta_{ij}}\right) = 0 \tag{48}$$

$$F_r - \sum_{j=1}^{j=Z}\left(\frac{K_{ij}(A_{2j}-X_{2j})\delta_{ij}^{1.5} + \frac{\lambda_{ij}M_{gi}}{D}(A_{1j}-X_{1j})}{(f_i-0.5)D+\delta_{ij}}\right) = 0 \tag{49}$$

$$\mathfrak{M} - \sum_{j=1}^{j=Z}\left(\frac{K_{ij}(A_{1j}-X_{1j})\delta_{ij}^{1.5} - \frac{\lambda_{ij}M_{gi}}{D}(A_{2j}-X_{2j})\Re_i}{(f_i-0.5)D+\delta_{ij}} + \lambda_{ij}f_iM_{gi}\right) \times \left[cos\,\psi_j\right] = 0 \tag{50}$$

The following is the relationship between normal contact deformations and normal ball loads:

$$Q_{oj} = K_{oj}\delta_{oj}^{1.5} \tag{51}$$

$$Q_{ij} = K_{ij}\delta_{ij}^{1.5} \tag{52}$$

Where Load-deflection constant $K_{o,i}$ is:

$$K_{o,i} = \frac{2\sqrt{2}\left(\frac{E}{1-\nu^2}\right)}{3(\sum\rho)^{1/2}}\left(\frac{1}{\delta^*}\right)^{\frac{3}{2}} \tag{53}$$

Where $\omega_m^2 = \left(\frac{\omega_m}{\omega}\right)^2\omega^2$, the centrifugal force F_{cj} and gyroscopic moments M_{gj} are obtained as:

$$F_{cj} = \frac{1}{2} m d_m \omega^2 \left(\frac{\omega_m}{\omega}\right)_j^2 \quad (54)$$

$$M_{gj} = J \left(\frac{\omega_R}{\omega}\right)_j \left(\frac{\omega_m}{\omega}\right)_j \omega^2 \sin\beta \quad (55)$$

$$\tan\beta = \frac{\sin\alpha_o}{\cos\alpha_o + \gamma'} \quad (56)$$

$$\gamma' = \frac{D}{d_m} \quad (57)$$

The ratio of ball to raceway angular velocities is calculated by setting β to 0:

$$\frac{\omega_R}{\omega} = \frac{\pm 1}{\left(\frac{\cos\alpha_o + \tan\beta \sin\alpha_o}{1+\gamma' \cos\alpha_o} + \frac{\cos\alpha_i + \tan\beta \sin\alpha_i}{1+\gamma' \cos\alpha_i}\right)\gamma' \cos\beta} \quad (58)$$

Inner raceway rotation is found by the lower sign, while outer raceway rotation is indicated by the upper sign.

Once more, the relationship between raceway speed and ball orbital angular velocity can be found using the outer raceway control condition. Since $\omega_m = -\omega_o$ for a rotating inner raceway, β' must equal 0.

$$\frac{\omega_m}{\omega} = \frac{1}{1 + \frac{(1-\gamma' \cos\alpha_i)(\cos\alpha_o + \tan\beta \sin\alpha_o)}{(1+\gamma' \cos\alpha_o)(\cos\alpha_i + \tan\beta \sin\alpha_i)}} \quad (59)$$

Consequently, for a bearing with a revolving inner racetrack, the ball orbital angular velocity to raceway speed ratio is:

$$\frac{\omega_m}{\omega} = \frac{1-\gamma' \cos\alpha_i}{1+\cos(\alpha_i - \alpha_o)} \quad (60)$$

$$m_b = \frac{1}{6} \rho \pi D^3 \quad (61)$$

$$J_b = \frac{1}{6} \rho \pi D^5 \quad (62)$$

The ball's orbital speed at angular location ψ_j is ω_m and ω is the speed of ring. It should be clear that orbital speed is not constant for every ball's location because it depends on the contact angle.

G is the gravitational force on the bearing, which is expressed by the following equation. Where m_b is the ball mass and g is the earth's gravitational acceleration G is:

$$G = m_b g \quad (63)$$

Skidding can be theoretically found as follows:

$$Skd_{theo} = \frac{\left(1-\frac{D}{d_m \cos\alpha_{ij}}\right)(\cos\alpha_{oj}+tan\,\beta\ \sin\alpha_{oj})}{\left(1+\frac{D}{d_m \cos\alpha_{oj}}\right)(\cos\alpha_{ij}+tan\,\beta\ \sin\alpha_{ij})+\left(1-\frac{D}{d_m \cos\alpha_{ij}}\right)(\cos\alpha_{oj}+tan\,\beta\ \sin\alpha_{oj})} \quad (64)$$

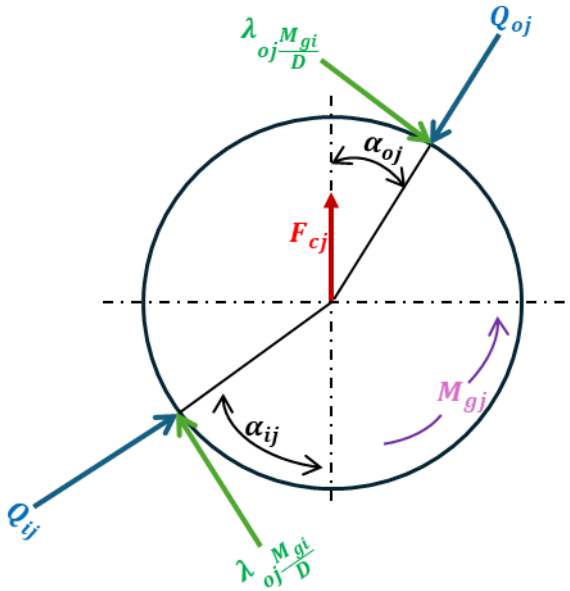

Figure 3.4: Ball loading at angular position ψ_j [29]

3.4. Loading and stress distribution modelling

From a ring to the others, the rolling parts transfer the loads supported by ball and roller bearings. Both the type of load placed on the bearing and its internal design determine how much loading each ball or roller can carry. Due to speed effects, rolling elements experience dynamic loading in addition to applied loading. Bearing geometry has an impact on dynamic loading as well.

The motions that take place in bearings are the basis for the equations that are developed in this section. A mass particle's location within the bearing that is rapidly traveling along an axis x is shown in instantaneous position in Figure 3.5. The following coordinate axis systems are presented in order to make the analysis simpler:

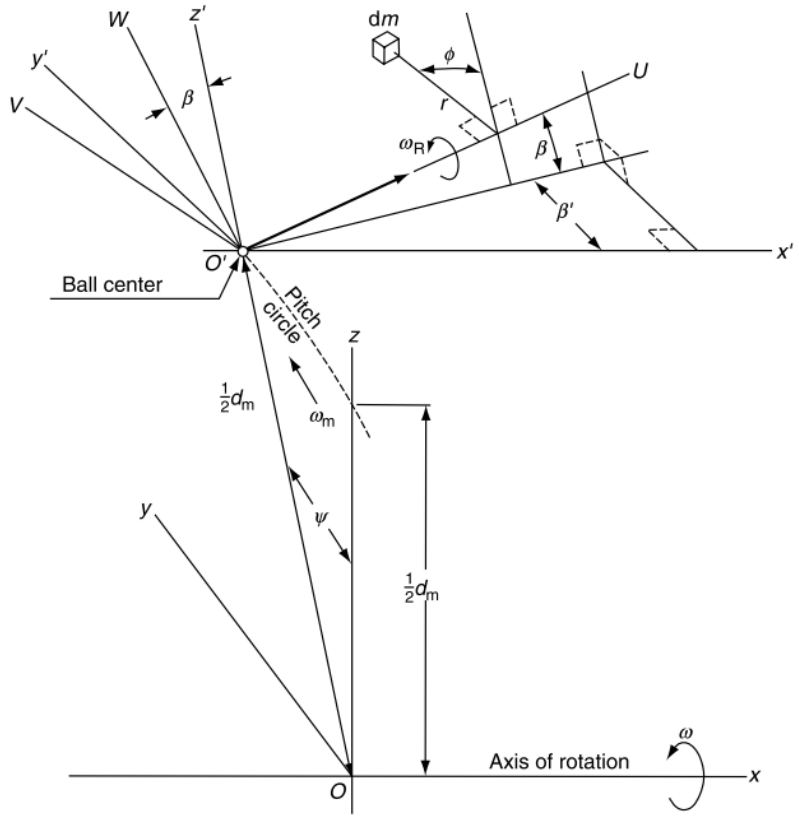

Figure 3.5: Ball mass element instantaneous position d_m [29]

(x, y, z) A constant Cartesian coordinate system where the x-axis aligns with the axis of bearing rotation.

(x', y', z') Cartesian coordinates where the fixed set's x axis is parallel to the x' axis. This coordinate system revolves at orbital speed around the fixed x axis at radius $^1/_2\, \boldsymbol{d_m}$ with its origin at 0' at the ball center.

(U, V, W) A constant of Cartesian coordinates that rotate at orbital speed ω_m and have their origin at the ball center 0'. The ball's rotation axis is about its own center and the U axes are collinear. The angle between the W and z' axes is β, and the W is in the planes of the U and z' axes.

(U, r, ϕ) Polar coordinate system that spins with the ball.

In the absence of a load, two revolving bodies having distinct radius of curvature in a pair of basic planes that intersect the contact between the bodies may meet at a single point. We refer to such a situation as point contact. This situation is depicted in

Figure 3.6. I represents the upper body, whereas II represents the lower body. The main planes are denoted by I and II. Thus, the radius of curvature of body I in plane λ I is represented by r_{I2}.

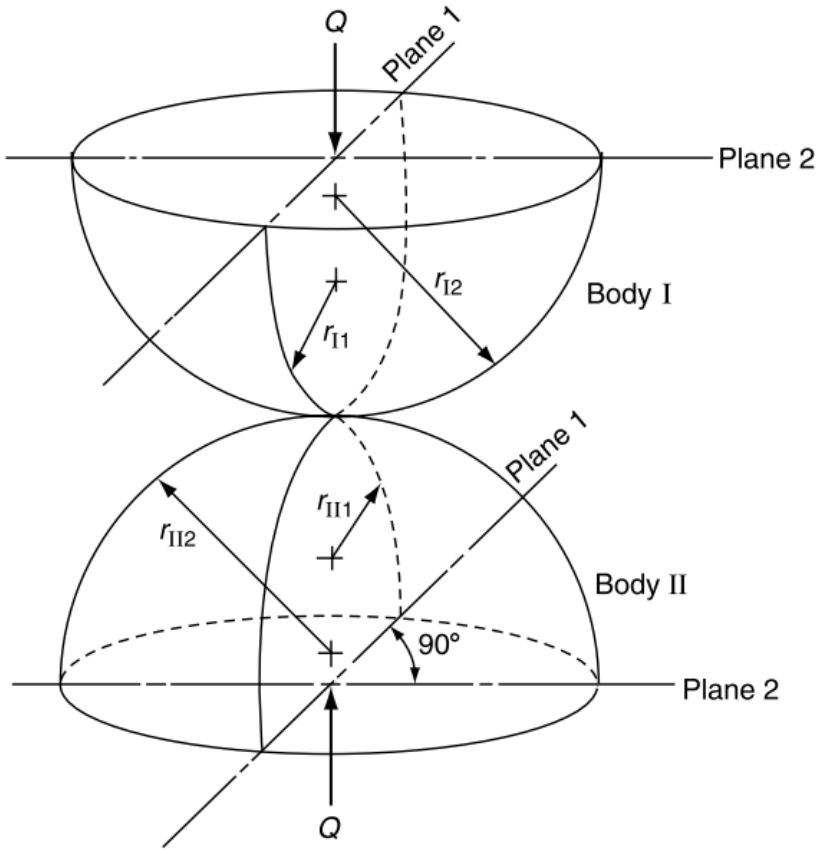

Figure 3.6: Contacting bodies geometry [29]

The following definitions are used to characterize contact between mating surfaces of revolution.

Curvature sum:

$$\sum \rho_i = \frac{4}{D} - \frac{1}{f_i D} + \frac{2}{D}\left(\frac{\gamma}{1-\gamma}\right) \quad = \quad \frac{1}{D}\left(4 - \frac{1}{f_i} + \frac{2\gamma}{1-\gamma}\right) \tag{65}$$

$$\sum \rho_o = \frac{4}{D} - \frac{1}{f_o D} + \frac{2}{D}\left(\frac{\gamma}{1-\gamma}\right) \quad = \quad \frac{1}{D}\left(4 - \frac{1}{f_o} + \frac{2\gamma}{1-\gamma}\right) \tag{66}$$

Curvature difference:

$$F_{(\rho)_i} = \frac{\frac{1}{f_i}+\frac{2\gamma}{1-\gamma}}{4-\frac{1}{f_i}+\frac{2\gamma}{1-\gamma}} \tag{67}$$

$$F_{(\rho)_o} = \frac{\frac{2}{D}\left(\frac{\gamma}{1-\gamma}\right)-\left(-\frac{1}{f_o D}\right)}{\sum \rho_o} = \frac{\frac{1}{f_o}+\frac{2\gamma}{1-\gamma}}{4-\frac{1}{f_o}+\frac{2\gamma}{1-\gamma}} \tag{68}$$

While γ is:

$$\gamma_{i,o} = \frac{D\cos\alpha_{i,o}}{d_m} \tag{69}$$

While most rolling bearing have a constant rotation of the outer, inner raceway, or both, the rotational speeds are usually too low to produce gyroscopic moments of magnitude or ball or roller centrifugal forces that would drastically change the distribution of the applied load. Additionally, in the majority of applications, this load distribution is not significantly impacted by the frictional forces and moments operating on the rolling parts. Therefore, in a vast majority of applications, it is generally acceptable to disregard these effects when examining the distribution of rolling element loads under simple operating conditions. On the other hand, during complex operating conditions that include high speeds and heavy loads, the influence of these factors must be considered, which is what the activities of this thesis include.

Each rolling element of a bearing loaded in pure thrust is loaded evenly in the manner described below:

$$Q = \frac{F_a}{Z\sin\alpha} \tag{70}$$

$$F_a = ZQ\sin\alpha \tag{71}$$

Nevertheless, the following is how an axial deflection constant K is defined:

$$\delta_K = \frac{B}{g(+\gamma)+g(-\gamma)} \tag{72}$$

where the inner racetrack is denoted by γ from (Eq 26), $g(+\gamma)$ and the outside raceway by $g(-\gamma)$. Jones [30] further shows that for all contact angles, the sum of g $(+\gamma)$ and g $(-\gamma)$. is almost constant and is only dependent on total curvature B. The axial deflection constant K for ball bearings is shown against the overall curvature B in Figure 3.7.

$$B = f_o + f_i - 1 \tag{73}$$

The relationship between K and the axial deflection constant, Kn, is as follows:

$$K_n = \frac{\delta_K D^{0.5}}{B^{1.5}} \tag{74}$$

$$\frac{F_a}{ZD^2\delta_K} = sin\,\alpha\left(\frac{cos\,\alpha^o}{cos\,\alpha} - 1\right)^{1.5} \tag{75}$$

$$\alpha' = \alpha + \frac{\frac{F_a}{ZD^2K} - sin\,\alpha\left(\frac{cos\,\alpha^o}{cos\,\alpha} - 1\right)^{1.5}}{cos\,\alpha\left(\frac{cos\,\alpha^o}{cos\,\alpha} - 1\right)^{1.5} + 1.5\,tan^2\,\alpha\left(\frac{cos\,\alpha^o}{cos\,\alpha} - 1\right)^{0.5} cos\,\alpha^o} \tag{76}$$

$$\delta_a = \frac{BD\,sin(\alpha - \alpha^o)}{cos\,\alpha} \tag{77}$$

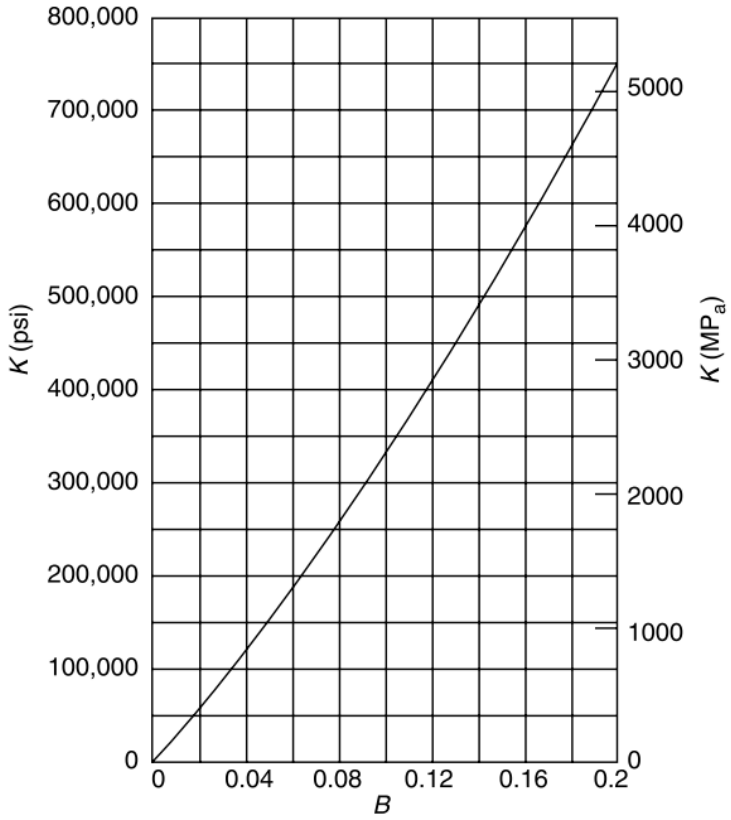

Figure 3. 7: Axial deflection constant K for ball bearings vs total curvature B [29]

For an elliptical contact area, the arbitrary length κ is defined by:

$$\kappa = {}^{a}/_{b} \tag{78}$$

Hower, Brewe and Hamrock [40] using a least squares method of linear regression, obtained simplified approximations for $k, \mathfrak{F}\ and\ \mathfrak{z}$. These equations are:

$$\mathcal{K} \approx 1.0339 \left(\frac{\Re_x}{\Re_y}\right)^{0.636} \tag{79}$$

$$\mathfrak{F} = 1.5277 + 0.6023 \ln\left(\frac{\Re_x}{\Re_y}\right) \tag{80}$$

$$\mathfrak{z} \approx 1.0003 + \frac{0.5968}{\left(\frac{\Re_x}{\Re_y}\right)} \tag{81}$$

$$\Re_x^{-1} = \rho_{x1} + \rho_{x2} \tag{82}$$

$$\Re_y^{-1} = \rho_{y1} + \rho_{y2} \tag{83}$$

$$a^* = \left(\frac{2\mathcal{K}^2\mathfrak{z}}{\pi}\right)^{1/3} \tag{84}$$

$$b^* = \left(\frac{2\mathfrak{z}}{\pi\mathcal{K}}\right)^{1/3} \tag{85}$$

$$\delta^* = \frac{2\mathfrak{F}}{\pi}\left(\frac{\pi}{2\mathcal{K}^2\mathfrak{z}}\right)^{1/3} \tag{86}$$

$$a = a^*\left[\frac{3Q}{2\sum\rho}\left(\frac{1-\xi_i^2}{E_i} + \frac{1-\xi_b^2}{E_b}\right)\right]^{1/3} \tag{87}$$

$$b = b^*\left[\frac{3Q}{2\sum\rho}\left(\frac{1-\xi_i^2}{E_i} + \frac{1-\xi_b^2}{E_b}\right)\right]^{1/3} \tag{88}$$

$$\delta = \delta^*\left[\frac{3Q}{2\sum\rho}\left(\frac{1-\xi_i^2}{E_i} + \frac{1-\xi_b^2}{E_b}\right)\right]^{2/3} \frac{\sum\rho}{2} \tag{89}$$

The geometrical center of an elliptical contact region experiences the most compressive stress. This stress's magnitude is:

$$\sigma_{max} = \frac{3Q}{2\pi ab} \tag{90}$$

Equation (89) provides the normal stress at additional locations within the contact region in line with Figure 3.8:

$$\sigma = \frac{3Q}{2\pi ab}\left[1 - \left(\frac{x}{a}\right)^2 - \left(\frac{y}{b}\right)^2\right]^{1/2} \tag{91}$$

Full flooded oil lubrication:

$$\tau_y = \frac{3\mu Q}{2\pi ab}\left[1 - \left(\frac{x}{a}\right)^2 - \left(\frac{y}{b}\right)^2\right]^{1/2} \quad (92)$$

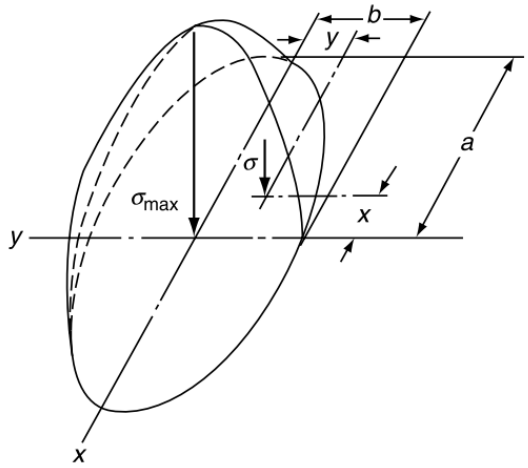

Figure 3.8: Point-contact ellipsoidal surface compressive stress distribution [29]

$F_{(\rho)}$	a^*	b^*	δ^*
0	1	1	1
0.1075	1,0760	0.9318	0.9974
0.3204	1.2623	0.8114	0.9761
0,4795	1.4556	0.7278	0.9429
0.5916	1.6440	0.6687	0.9077
0.6716	1.8258	0.6245	0.8733
0.7332	2.011	0.5881	0.8394
0,7948	2.265	0.5480	0.7961
0.83495	2.494	0.5186	0.7602
0.87366	2.800	0.4863	0.7169
0.90999	3.233	0.4499	0.6636
0.93657	3.738	0.4166	0.6112
0,95738	4.395	0.3830	0.5551
0.97290	5.267	0.3490	0.4960
0.983797	6.448	0.3150	0.4352

0.990902	8.062	0.2814	0.3745
0.995112	10.222	0.2497	0.3176
0.997300	12.789	0.2232	0.2705
0.9981847	14.839	0.2072	0.2427
0.9989156	17.974	0. 18822	0.2106
0.9994785	23.55	0.16442	0.17167
0.9998527	37.38	0. 13050	0.11995
1	∞	0	0

Table 3.1: Dimensionless contact parameter

3.5. Bearing generation heat modeling

A rolling element-raceway contact is too complex to be captured in a straightforward analytical expression. Some combinations of rolling, sliding, and spinning motions are produced by the combined action of kinematic constraints and an applied force. These motions pull the lubricant into contact, where its characteristics, which are influenced by the pressure and temperature variations across the contact area, create a film that, to a certain degree, separates the contacting bodies based on the lubricant's characteristics as well as the bodies' microgeometry. A multitude of extremely irregularly shaped microcontacts emerge within the micro-contact when the separating film is small in relation to the composite surface roughness. This results in microscale perturbations in temperature, pressure, and film thickness. Furthermore, these microcontacts have the potential to flex both elastically and plastically, which causes the microgeometry to change over time.

The separating lubricant layer is sheared by sliding and spinning motions on the macro-contact, which also drags the microcontacts across one another if separation is just partial. A tangential force is the product of these combined processes. A major determinant of fatigue life, this tangential or traction force modifies the solids' stress distribution. The characteristics of the lubricant under the regionally varying pressure, temperature, and shear rates that predominate in the macro-contact determine how much the fluid contributes to traction. The type of surface boundary films formed by

oxidation and lubricant additives, or the local film conditions, will determine how much traction the sliding microcontacts can provide.

It is widely acknowledged that the dry friction experienced while sliding identical surfaces over one another is far greater than the friction caused by rolling nonlubricated surfaces over one another. Although the movements of the contacting elements in rolling bearings are more complicated than what pure rolling suggests, rolling bearings have far less friction than the majority of fluid film or sleeve bearings of comparable size and load-carrying capability. Naturally, the hydrostatic gas bearing is a noteworthy exception to the aforementioned rule; nevertheless, unlike rolling bearings, these bearings are not self-sustaining and necessitate a sophisticated gas supply system. Any amount of friction results in a waste of energy and slows down motion. As a result, friction in a rolling bearing causes a rise in temperature and can be quantified as a retarding torque. There are numerous sources of friction in rolling bearings, however the following are the main ones:

As a result, friction in a rolling bearing causes a rise in temperature and can be quantified as a retarding torque. There are numerous sources of friction in rolling bearings, however the following are the main ones:

1. Rolling elastic hysteresis.
2. The shape of the contacting surfaces causes sliding in rolling element-raceway contacts.
3. Sliding because of contacting elements' deformation.
4. The cage can slide between rolling elements and, in the case of a landriding cage, between bearing rings.
5. Lubricant viscous drag on the cage and rolling elements.
6. Sliding between inner and/or outer ring flanges and roller ends.
7. Friction in the seal.

Rotational friction, lubricant viscosity, and applied load combine to form the bearing's total friction torque. It is possible to write the total friction torque in [41] as :

$$M_{total} = M_1 + M_v \tag{93}$$

$$M_1 = f_l P_1 d_m \tag{94}$$

$$M_v = 10^{-7} f_e (v_o * RPM)^{\frac{2}{3}} (d_m)^3 \tag{95}$$

$$P_1 = 0.9 F_a ctn(\alpha) - 0.1 F_r \tag{96}$$

Where P_1 is torque due to applied load, $M_1$is rolling friction torque, M_v is viscous friction torque, f_e is a factor depending upon the type of bearing and method of lubrication from [29]. v_o is an oil kinematic viscosity at operating temperature and M_{total} is the total friction torque on the bearing.

$$b_i^* = \left(\frac{2\epsilon_i}{\pi \kappa_i}\right)^{\frac{1}{3}} \tag{97}$$

$$M_{si} = \frac{3\mu Q_i a_i \epsilon_i}{8} \tag{98}$$

$$b_o^* = \left(\frac{2\epsilon_o}{\pi \kappa_o}\right)^{\frac{1}{3}} \tag{99}$$

$$M_{so} = \frac{3\mu Q_o a_o \epsilon_o}{8} \tag{100}$$

While $\kappa_{i,o}$ is the aspect ratio of the ellipse of inner, outer raceway, $\epsilon_{i,o}$ is the complete elliptic integral of the second kind for inner, outer raceway, $b_{i,o}^*$is dimensionless semi-minor axis of contact ellipse of inner, outer raceway, $M_{si,o}$ is friction torque due to spinning about the axis normal to the inner, outer raceway contact area, μ is coefficient of friction, the $Q_{i,o}$ is the Normal force between rolling element and inner, outer raceway and $a_{i,o}$ is semimajor axis of the projected contact of inner, outer raceway.

The maximum stress occurring at the outer raceway C_s is:

$$C_s = \varphi_s \, i \, Z \, D^2 \cos\alpha \tag{101}$$

Where φ_s is a parameter related to the bearing geometry from [29] and i is how many rows are in bearing.

$$F_s = X_s F_r + Y_s F_a \tag{102}$$

$$\mathrm{f}_l = z_e y_e (F_s / C_s) \tag{103}$$

Where F_s is a static equivalent load for combining radial and thrust loads, X_s is radial load factor and Y_s is axial load factor). Both are from [29]. F_a is the applied axial load and F_r is the applied radial load. f_l is a factor depending upon bearing design and relative bearing load. $y_e$is distance in the Y direction and $z_e$is distance in the Z direction. Both are from [29].

$$n_s = \left(\frac{\left(1-\gamma' \cos\alpha_i\right)\tan(\alpha_i-\beta)+\gamma' \sin\alpha_i}{\gamma'}\right) \times RPM \left(\frac{1-\gamma' \cos\alpha_i}{1+\cos\left(\alpha_i-\alpha_o\right)}\right) \quad (104)$$

$$H_{fi_j} = 1.047 \times 10^{-4} n_s M_{si} \quad (105)$$

$$H_{fi} = Z \times H_{f_{ij}} \quad (106)$$

$$H_{fo_j} = 1.047 \times 10^{-4} n_s M_{so} \quad (107)$$

$$H_{fo} = Z \times H_{f_{oj}} \quad (108)$$

Where $H_{fi,o_j}$is the bearing frictional power loss in watts at each rolling elements of inner/outer raceway. $M_{si,o}$ is friction torque due to spinning about the axis normal to the inner/outer raceway contact area. n_s is the ball spinning speed. $H_{f_{i,o}}$ is the bearing frictional power loss in watts of the whole inner/outer raceway.

$$H_{1_v} = 1.047 \times 10^{-4} RPM\ M_{total} \quad (109)$$

$$H_{i\_total} = H_{1_v} + H_{fi} \quad (110)$$

$$H_{0\_total} = H_{1_v} + H_{fo} \quad (111)$$

Where H_{1_v} is the viscous heat generated and H_{i,o_total} is the total heat generated on the inner/outer raceway.

$$u_s = \frac{1}{2}\left(\frac{\pi * RPM * d_m}{60}\right) \quad (112)$$

$$P_r = \frac{c_{p*}\, v_o}{\Omega} \quad (113)$$

$$h_V = 0.0332\ \Omega\ P_r^{\,0.33} \left(\frac{u_s}{v_o d_m}\right)^{0.5} \quad (114)$$

Where u_s is equal to bearing cage surface velocity, h_V is the film coefficient of heat transfer, Ω is thermal conductivity, $P_r$is Prandtl number of the oil, c_p is the specific heat capacity and v_o is kinematic viscosity.

$$S_i = \frac{Z * 2 * a_i * {b_i}^3}{3} \quad (115)$$

$$S_o = \frac{Z * 2 * a_o * {b_o}^3}{3} \quad (116)$$

$$H_{vi} = h_v \, S_i \, \Delta T_i \quad (117)$$

$$H_{vo} = h_v \, S_o \, \Delta T_o \quad (118)$$

$$H_{ci} = \frac{\Omega \, S_i}{\wp_i} \, \Delta T_i \quad (119)$$

$$H_{co} = \frac{\Omega \, S_o}{\wp_o} \, \Delta T_o \quad (120)$$

$$H_{i\_total} = \left(h_v \, S_i \, + \frac{\Omega \, S_i}{\wp_i}\right) \Delta T_i \quad (121)$$

$$H_{o\_total} = \left(h_v \, S_o + \frac{\Omega \, S_o}{\wp_o}\right) \Delta T_o \quad (122)$$

Where $H_{vi,o}$is the heat convection between surfaces.$S_{i,o}$ is the area normal to the flow of heat between two points of inner, outer ring. ΔT_i is the difference temperature between shaft and inner ring. ΔT_o is the difference temperature between outer ring and housing.$H_{ci,o}$is the heat conduction between surfaces and $\wp_{i,o}$ is the distance between the same two points of inner, outer ring.

	Symbol	parameter	value	unit
1	v_o	Kinematic viscosity	5	mm^2/s
2	Ω	Thermal conductivity	0.14	W/M.K
3	$\wp_i$	The distance between the same two points in inner ring side	12.79	mm
4	$\wp_o$	The distance between the same two points in outer ring side	12.27	mm
5	-	Oil type at 40°C	SAE 20 W40	-
6	α	Nominal contact angle	40	degree
7	μ	The coefficient of friction	0.03	-
8	φ_s	A parameter related to the bearing geometry	15.48	-
9	i	Number of the rows in bearing	1	-

10	X_s	The radial load factor	0.5	-
11	Y_s	The axial load factor	0.26	-
12	y_e	The distance in the Y direction	0.33	mm
13	z_e	The distance in the Z direction	0.001	mm
14	f_e	A factor depending upon the type of bearing and method of lubrication	6.6	-
15	c_p	The specific heat capacity at constant pressure	2.2	J/g.oC

Table 3.2*:* Heat generation parameters and their values

3.6. Bearing fatigue life calculation modelling

It has been believed that all causes of damage, with the exception of material fatigue, may be avoided provided a rolling bearing in operation is adequately greased, properly aligned, and kept free from abrasives, moisture, and corrosive chemicals. In the past, rolling bearing theory assumed that because of the likelihood of surface fatigue in rolling contact, no rotating bearing could provide infinite service. When compared to other loads operating on engineering structures, the stresses that are continually applied to these surfaces can be incredibly large, as mentioned in the previous sections of this thesis. In the latter instance, some steels appear to have an endurance limit, as seen in Figure 3.9. This endurance limit is the maximum amount of cyclically applied, reversing stress that, if not exceeded, the structure can sustain before failing due to exhaustion. The endurance limit for structural fatigue has been established by the use of rotating beams and/or torsional testing of basic bars for various materials; however, this is outside the purview of the work.

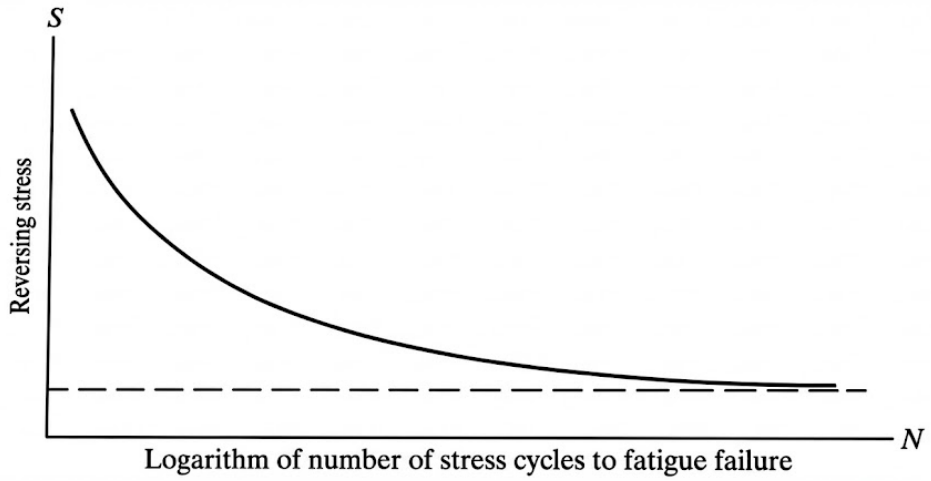

Figure 3. 9: S-N curve for mild steel [29]

The flaking off of metallic particles from the raceway and/or rolling element surfaces is a sign of rolling contact fatigue. This flaking often starts as a crack beneath the surface of correctly made, well-lubricated bearings and spreads to the surface, finally forming a pit or spall in the load-carrying surface [42]. According to the hypothesis of Lundberg et al. [43], the crack is caused by the maximum orthogonal shear stress which takes place at a depth below the surface. An image of a typical fatigue failure in a ball bearing raceway may be found in Figure 3.10 [44].

Figure 3. 10: A typical fatigue failure in a ball bearing raceway [44]

The maximal orthogonal shear stress is not always accepted by researchers as the critical stress that causes failure. An additional criterion is the Von Mises distortion

energy theory, which produces a scalar "stress" level—that is, the maximum orthogonal shear stress—of comparable magnitude to the double amplitude, Figure 3.11 [45].

According to the hypothesis of Lundberg et al. [43], fatigue cracking starts at weak spots under the material's surface. Therefore, with all other things being equal, altering the steel's composition, metallurgical structure, and homogeneity can have a big impact on a bearing's fatigue characteristics. Macroscopic slag inclusions, which result in unsuitable steel for bearing manufacture and, ultimately, premature failure, are not included when discussing weak areas. The weak areas in question may be microscopic inclusions and metallurgical dislocations that are only observable through laboratory techniques.

According to the foregoing analysis, the fatigue life of a rolling element- raceway point contact subjected to normal load $\boldsymbol{Q}$ may be estimated by [29]:

$$L = \left(\frac{Q_c}{Q}\right)^3 \tag{123}$$

$$Q_{ci} = 93.2 * \left(\frac{2f_i}{2f_i - 1}\right)^{0.41} \frac{(1-\gamma_i)^{1.39}}{(1+\gamma_i)^{1/3}} \left(\frac{\gamma_i}{cos\,\alpha_i}\right)^{0.3} D^{1.8} Z^{\frac{-1}{3}} \tag{124}$$

$$Q_{co} = 93.2 * \left(\frac{2f_o}{2f_o - 1}\right)^{0.41} \frac{(1+\gamma_o)^{1.39}}{(1-\gamma_o)^{1/3}} \left(\frac{\gamma_o}{cos\,\alpha_o}\right)^{0.3} D^{1.8} Z^{\frac{-1}{3}} \tag{125}$$

To account for spinning, the inner raceway capacity is reduced by a factor of $1 - 0.33 \times \sin \alpha_i$.

$$Q'_{ci} = Q_{ci}(1 - 0.33\,sin\,\alpha_i) \tag{126}$$

$$L_i = \left(\frac{Q_{ci}}{Q_{ei}}\right)^3 \tag{127}$$

$$L_o = \left(\frac{Q_{co}}{Q_{eo}}\right)^3 \tag{128}$$

$$L_H = \frac{L}{N*60} \tag{129}$$

$$L = (L_i^{-1.11} + L_o^{-1.11})^{-0.9} \tag{130}$$

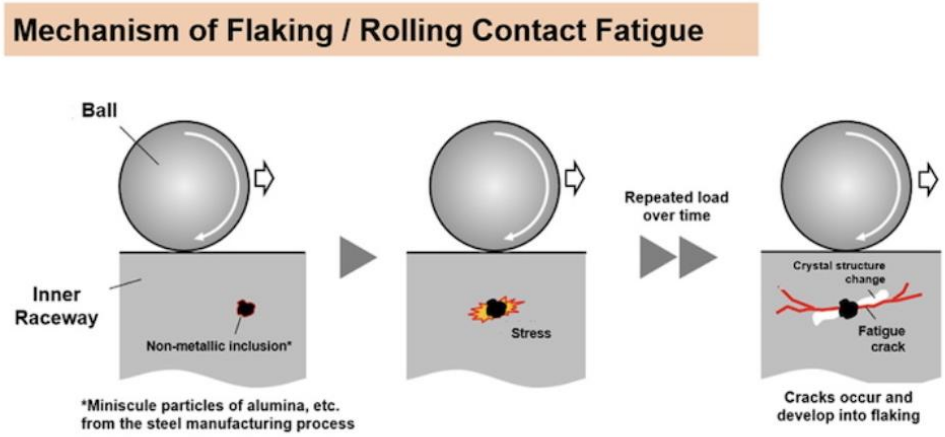

Figure 3.11: A diagram showing how the fatigue starts beneath the surface of the metal [45]

3.7. Model Structure and Computational Flow

The proposed coupled model was implemented in MATLAB through a structured, iterative computational routine. The core algorithm integrates the theoretical equations into a numerical framework designed to solve the interdependent mechanical, thermal, and tribological phenomena. Figure 3.12 presents a high-level block diagram of this implementation, illustrating the main modules, data flow, and iterative loops. The primary computational steps are as follows, with key equation groups indicated in parentheses:

1. **Input Parameters & Initialization:** Geometric, material, and operational constants are listed in Table 4.1. Initial values for the primary unknowns—the axial, radial, and angular displacements of the inner ring (δ_a,δ_r,θ)—are set.

2. **Mechanical Equilibrium Loop (Newton-Raphson Solver):** This core module solves the system of nonlinear equilibrium equations governing the bearing's internal load distribution under high-speed dynamics.

    - For each ball at angular position ψj, it solves for the ball center coordinates (X_{1j}, X_{2j}) and contact deflections (δ_{ij},δ_{oj}) using geometric compatibility equations **(44, 45)** and force equilibrium equations **(46, 47)**.

- The solver uses the Newton-Raphson method to iteratively update the ring displacements (δ_a,δ_r,θ) until global equilibrium of forces and moments is satisfied, equations **(48, 49, 50)**.
- Outputs from this module for each ball position include the normal contact loads (Q_{ij},Q_{oj}), contact angles (α_{ij},α_{oj}), and centrifugal forces.

3. **Thermal Coupling Loop:** Using the contact loads and kinematics from the mechanical solution, this module calculates the bearing's thermal state.
   - **Heat Generation:** The frictional power loss is computed, decomposed into components from spinning friction, equations **(105, 107)**, load-dependent friction, and viscous friction equation **(109)**.
   - **Heat Transfer & Temperature Update:** A simplified thermal network model solves for the temperature rise of the inner and outer rings (ΔT_i ,ΔT_o) using equations for conducted and convected heat, equations **(119, 120, 117, 118)**.
   - **Convergence Check:** The algorithm checks if the temperature difference between successive iterations is below a threshold (0.01 °C). If not, the updated temperatures are used to recalculate thermal expansions, which modify clearances and material properties. The process then returns to the Mechanical Equilibrium Loop with updated geometry.
4. **Post-Processing & Output:** Once mechanical and thermal convergence is achieved, final performance metrics are calculated.
   - **Fatigue Life:** The basic dynamic load capacity (Q_{ci},Q_{co}) is computed by equations **(124, 125)**, and the bearing L_{10} life is estimated by equations **(127, 128, 130)**.
   - **Performance Summary:** All results—including contact loads, angles, friction torque, heat generation rates, and fatigue life—are compiled, visualized, and exported to structured files (e.g., Excel) for analysis.

The MATLAB code is structured into modular functions corresponding to these blocks (NewtonRaphsonSolver.m, HeatGeneration.m, ThermalSolver.m), called sequentially

by a main script. This modular design enhances code clarity, maintainability, and facilitates future extensions. The calculation flow of the model is shown in Figure 3.12 below.

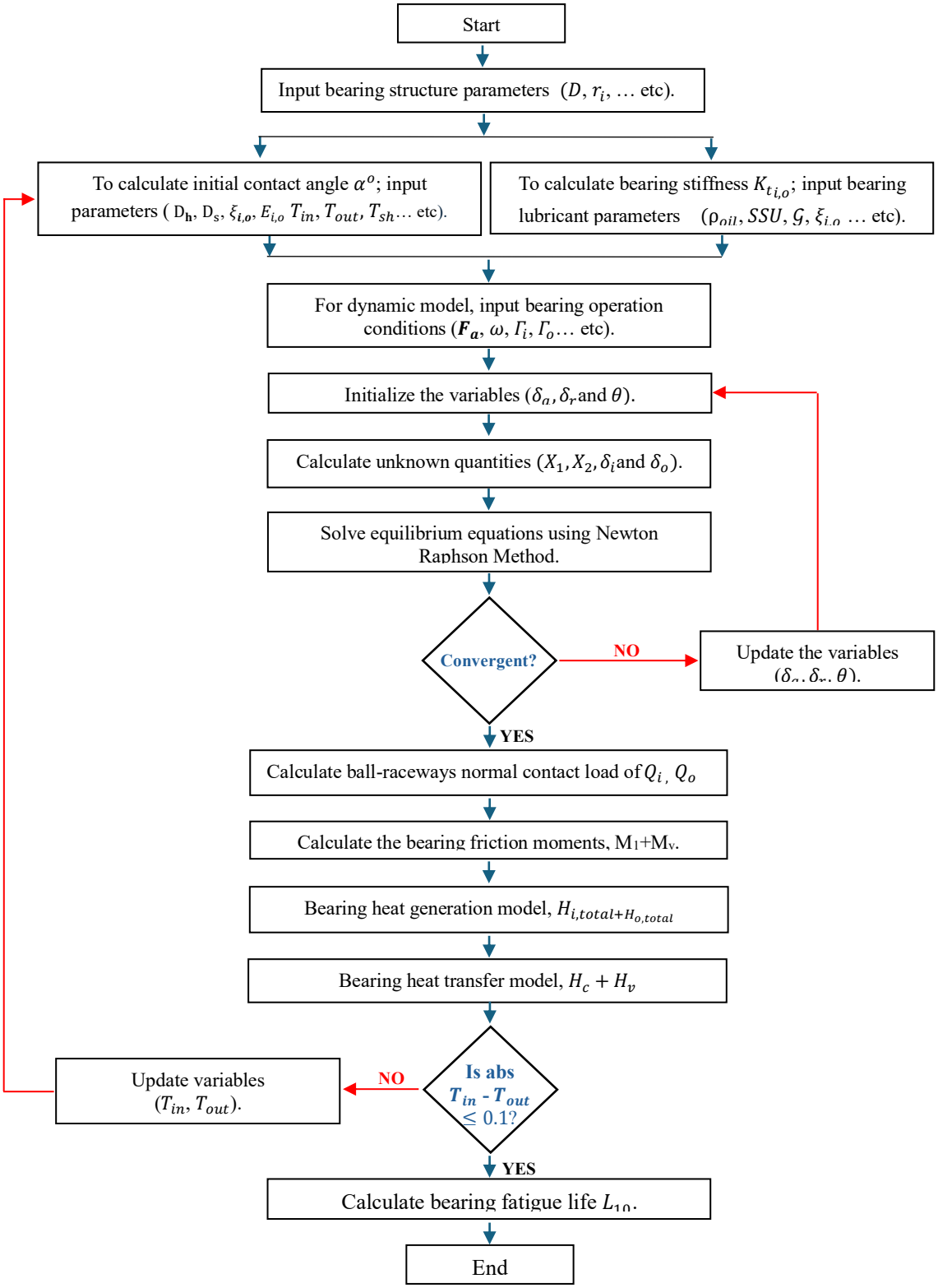

Figure 3.12: Flowchart of the coupled iterative algorithm for solving mechanical-thermal-lubrication equilibrium in the proposed model

Chapter 4: Results and discussion

4.1. Simulation Input Parameters and Model Configuration

To ensure transparency and reproducibility, all numerical simulations presented in this chapter were conducted using the proposed coupled model with a consistent set of input parameters. These parameters are representative of a medium-scale angular contact ball bearing (ACBB) designed for high-speed applications, such as those found in aerospace gas turbine systems. The bearing geometry, material properties, operational conditions, and lubricant characteristics are summarized in Table 4.1.

The simulations systematically vary two primary operational variables:

1. **Axial Load (*Fa*):** Ranging from 0 N to 47,500 N, in increments of 2,500 N.
2. **Rotational Speed (*N*):** Set at 6,000 RPM, 10,000 RPM, and 15,000 RPM.

All other parameters were held constant unless otherwise specified in comparative analyses (e.g., material comparisons in Sections 4.6–4.8). The results presented in the following sections are the product of the coupled iterative algorithm described in Section 3.6, which solves for mechanical equilibrium, lubrication state, thermal balance, and fatigue life for each unique combination of load and speed.

Category	Parameter	Symbol	Value	Unit
Bearing Geometry	Ball Diameter	D	12.7	mm
	Pitch Diameter	d_m	65.0	mm
	Number of Balls	Z	16	–
	Initial Contact Angle (unloaded)	α^o	40	°
	Inner Raceway Groove Radius	r_i	6.603	mm
	Outer Raceway Groove Radius	r_o	6.603	mm

Category	Parameter	Symbol	Value	Unit
	Inner Ring Bore Diameter	d_i	52.3	mm
	Outer Ring Outside Diameter	d_o	77.7	mm
	Inner Raceway Curvature Factor	f_i	0.52	–
	Outer Raceway Curvature Factor	f_o	0.52	–
Material Properties (Baseline: Alloy Steel AISI 52100)	Young's Modulus	E	210	GPa
	Poisson's Ratio	v	0.3	–
	Density	ρ	7800	kg/m³
	Thermal Expansion Coefficient	Γ	11.5×10−6	1/K
Operational Conditions	Applied Axial Load Range	Fa	0 – 47,500	N
	Rotational Speeds	n	6,000; 10,000; 15,000	RPM
	Ambient / Housing Temperature	T_{amb}	40	°C
	Gravitational Acceleration	g	9.81	m/s²
Lubricant (SAE 20W40 Mineral Oil)	Kinematic Viscosity at 40°C	v_0	5.0	mm²/s
	Thermal Conductivity	Ω	0.14	W/(m·K)

Category	Parameter	Symbol	Value	Unit
	Specific Heat Capacity	c_p	2.2	kJ/(kg·K)
	Pressure-Viscosity Coefficient	λ	1.122×10−8	Pa^{-1}
	Density	ρ_{oil}	875	kg/m^3
Tribological & Calculation Parameters	Coefficient of Friction (Ball-Raceway)	μ	0.03	–
	Convergence Tolerance (Thermal Loop)	ΔT_{tol}	0.1	°C
	Convergence Tolerance (Newton-Raphson)	ϵ	1×10−6	–

Table 4. 1:Primary input parameters for numerical simulations

4.2. Effect of applied load on the inner raceway contact load at various speeds

The Harris model and the new model are contrasted in terms of inner raceway contact load (Qi) for various loads and speeds (6000, 10000, and 15000 RPM), Figure 4.1-4.3. The comparison provides significant information regarding the performance of the bearing as further explored by Table 4.1. The new model generally predicts higher contact loads than the Harris model in all scenarios. It accounts for issues not fully addressed by standard techniques. The contact load increases with the increase in the applied load in an expected manner and presents a near-straight-line relationship in both the new and Harris models. The contrast between the Harris and the new model is even better when the applied load is elevated. It indicates that at higher loads, the new model carefully examines issues such as local deformation temporary effects due to heat and particle-particle interaction effects on load transfer. The impact of varying speeds is evident in the results. At low speeds (6000 RPM), the distinction between the two

models is clearer, but at 15000 RPM, the predictions are closer. This implies that the Harris model may not be able to predict well how elastohydrodynamic lubrication and dynamic interactions behave at lower speeds. However, at higher speeds, the simpler concepts are more appropriate. The new model likely incorporates heat changes and film thickness variations, which account for the differences observed. One of the salient points of the new model is that it accounts for the effects of elastohydrodynamic lubrication (EHL) and changes in heat. The higher contact load exhibited by the model indicates that lubrication film thickness, heat expansion of materials, and clearance changes are significant in altering the load distribution. At higher speeds, the EHL state would be more stable, but at lower speeds, thinner lubricant from temperature and local heating can boost contact stresses, which is consistent with what we observe. The higher contact loads from the new model imply greater stress on the raceway, which can contribute to more wear and fatigue in the long run. This result indicates that we should develop better lubrication techniques, preload conditions, and heat management to enable bearings to last longer. In addition, the better modeling of multiparticle contact mechanics implies that problems such as contamination, debris interaction, and initiating small defects could further influence performance, things that conventional models do not handle well. The results indicate that the new mathematical and theoretical coupled model provides an improved understanding of ACBB behavior, particularly in illustrating how lubrication, heat changes, and varying loads influence its performance.

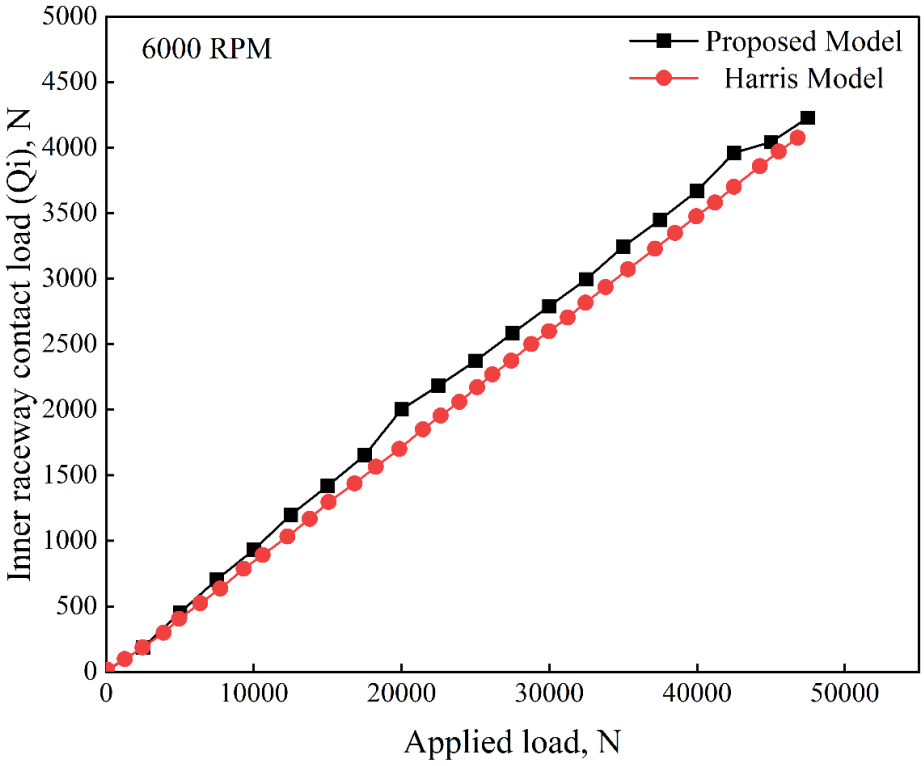

Figure 4. 1: Effect of applied load on the inner raceway contact load at 6000 RPM

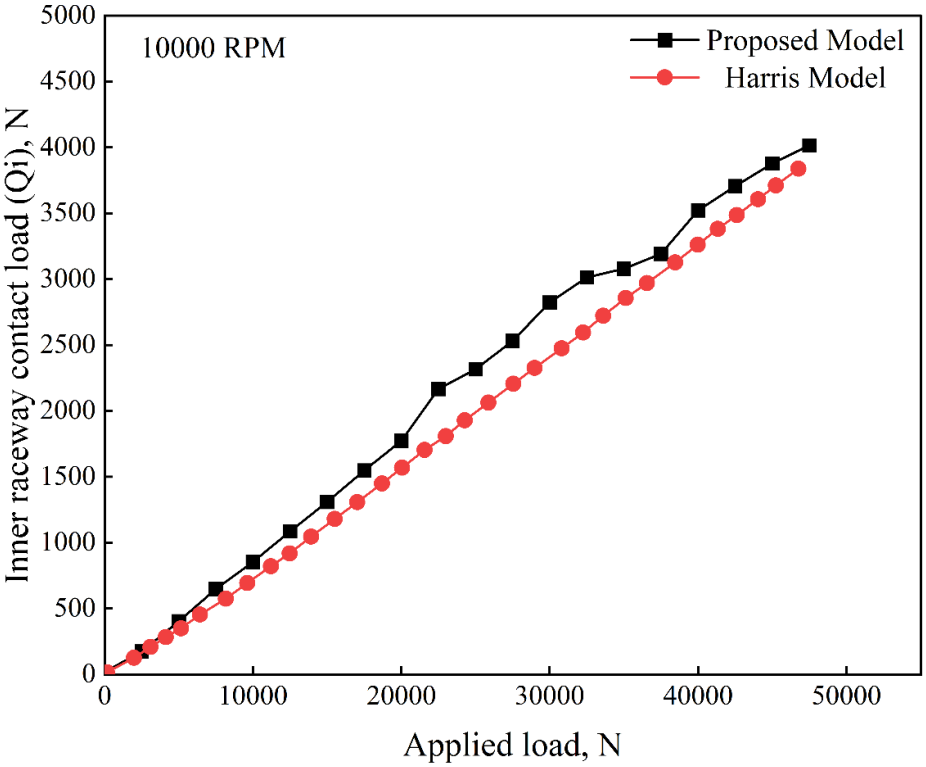

Figure 4.2: Effect of applied load on the inner raceway contact load at 10000 RPM

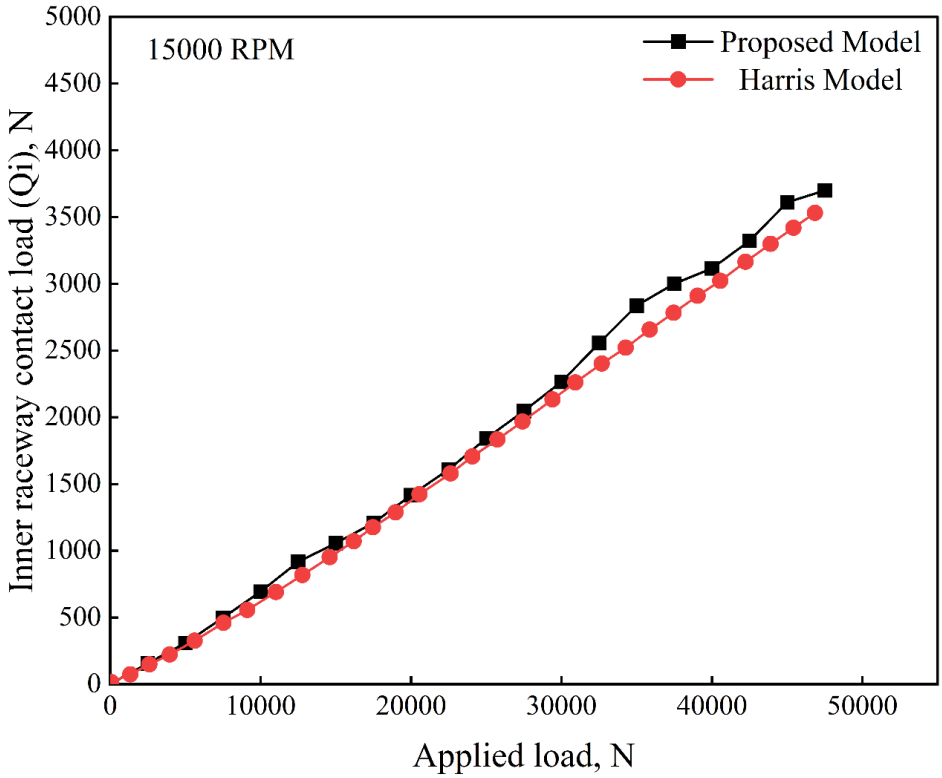

Figure 4.3: Effect of applied load on the inner raceway contact load at 15000 RPM

4.3. Effect of applied load on the outer raceway contact load at various speeds

The paper examines the variation in the outer raceway contact load (Qo) in an angular contact ball bearing (ACBB) with various loads and speeds (6000 RPM, 10000 RPM, and 15000 RPM), Figure 4.4-4.6. The primary aim is to contrast a new model with the Harris model and analyze the accuracy of each in predicting the values of Qo in various scenarios as further explored by Table 4.2. The findings present a clear trend: the increase in the load and speed increases the value of Qo, something to be expected due to increased elastic deformation and larger forces on the rolling components. The new model consistently estimates higher values of Qo relative to the Harris model, and the gap widens with increased speed, particularly with high loads. The implication is that the Harris model [29] may not take into account certain effects of speed that become significant in high-speed and load scenarios.

The two models are quite similar at 6000 RPM. It indicates that during medium speeds, the predictions made by both models are quite identical. However, when the speed

increases to 10000 RPM and then to 15000 RPM, the Harris model indicates a poorer quality of operation (Qo) compared to the proposed model. The disparity indicates that the Harris model fails to account for the influence of elastohydrodynamic lubrication (EHL), the expansion caused by heat due to friction, and varied loads on the bearings when operating at high speed. The influence on the stress distribution in the contact area is changed by the addition of a layer of lubricant through the use of EHL. The generation of increased heat due to friction causes the expansion of the bearing components and alteration in the inner space, hence the way the loads are distributed. The influence caused by the rolling components through centrifugal forces and gyroscopic moments is another factor in the bearing components. It is responsible for the distribution of the contact loads to the bearing components.

The data confirms these observations and indicates that Qo increases steadily with the load. At 6000 RPM, the initial Qo is 353.81 N with no load and increases to 4488.91 N with a load of 47500 N. At 10000 RPM, the initial Qo is much greater and increases from 1067.89 N to 4615.45 N with the full load. At 15000 RPM, the initial Qo increases even further to 2466.29 N and reaches 4716.65 N with a load of 47500 N. The greater initial Qo with increased speed indicates the significance of centrifugal forces in the manner in which the load is distributed and the need for such effects to be represented in better models.

The findings are significant in understanding the operation and reliability of bearings when they are running at high speed. Accurately forecasting Qo is significant in maintaining proper lubrication procedures. Good lubrication will prevent wear and overheating, and these are the major causes of failures in bearings operating at high speed. Improved load predictions will enable the generation of better maintenance schedules and the ability to determine how long the bearings will last and function in varied conditions. The comparison between the Harris model and the new model demonstrates the necessity of developing better-bearing analysis models. That entails taking into account high-speed conditions such as fluctuating temperatures and contact with multiple particles. Such advances will ensure better-bearing designs with reduced maintenance costs and improved performance in high-speed machines such as aerospace engines, high-speed turbos, and high-precision tools.

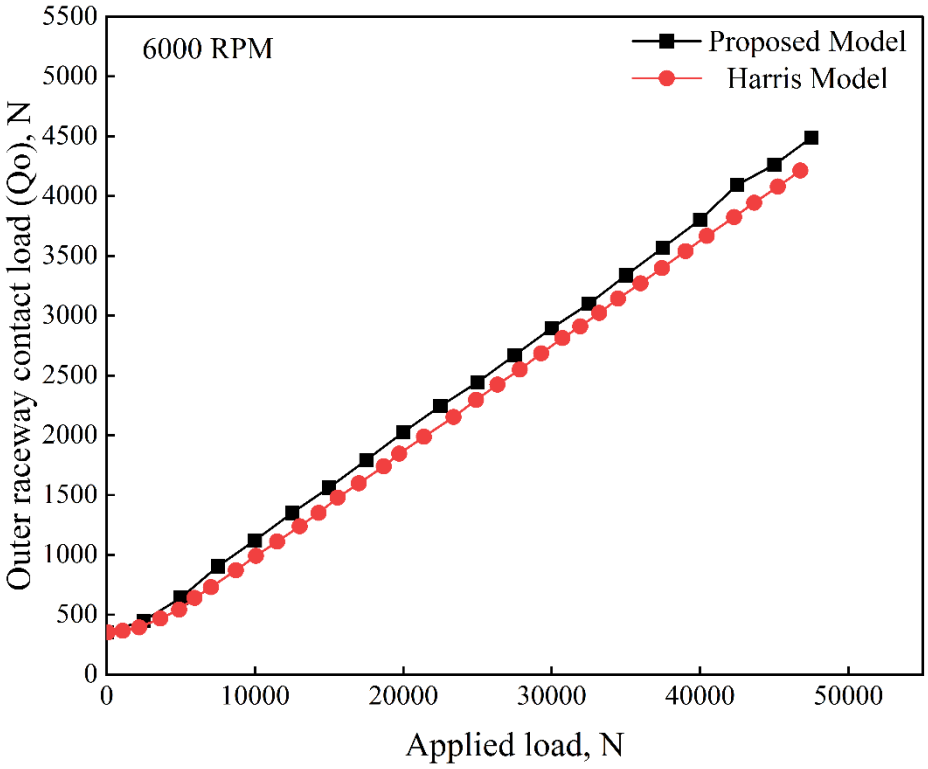

Figure 4.4: Effect of applied load on the outer raceway contact load at 6000 RPM

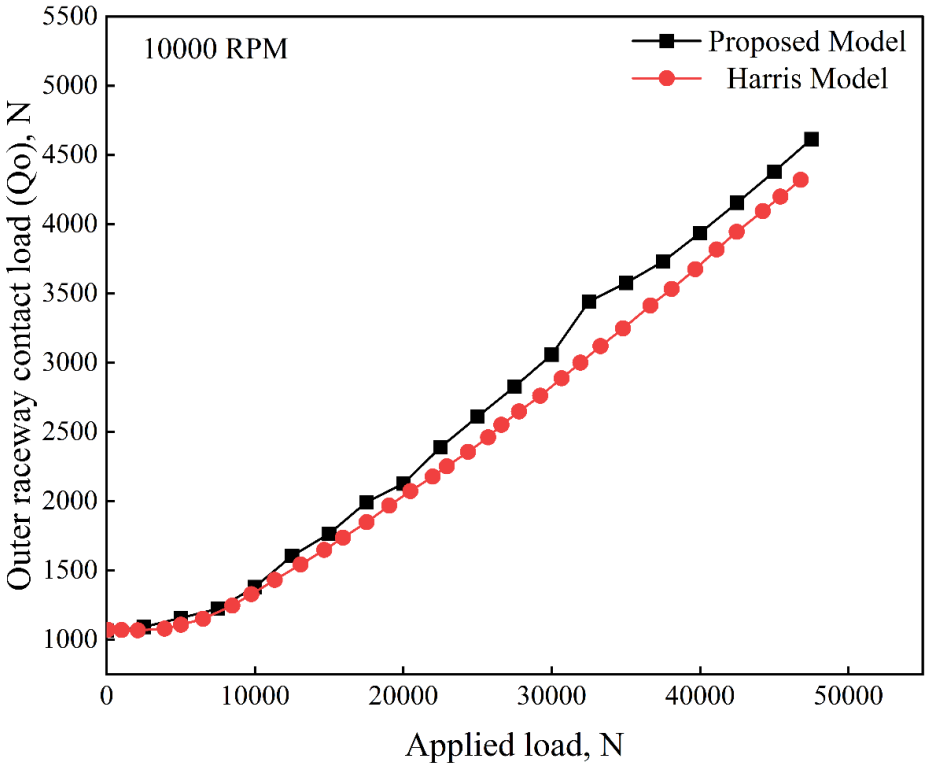

Figure 4. 5: Effect of applied load on the outer raceway contact load at 10000 RPM

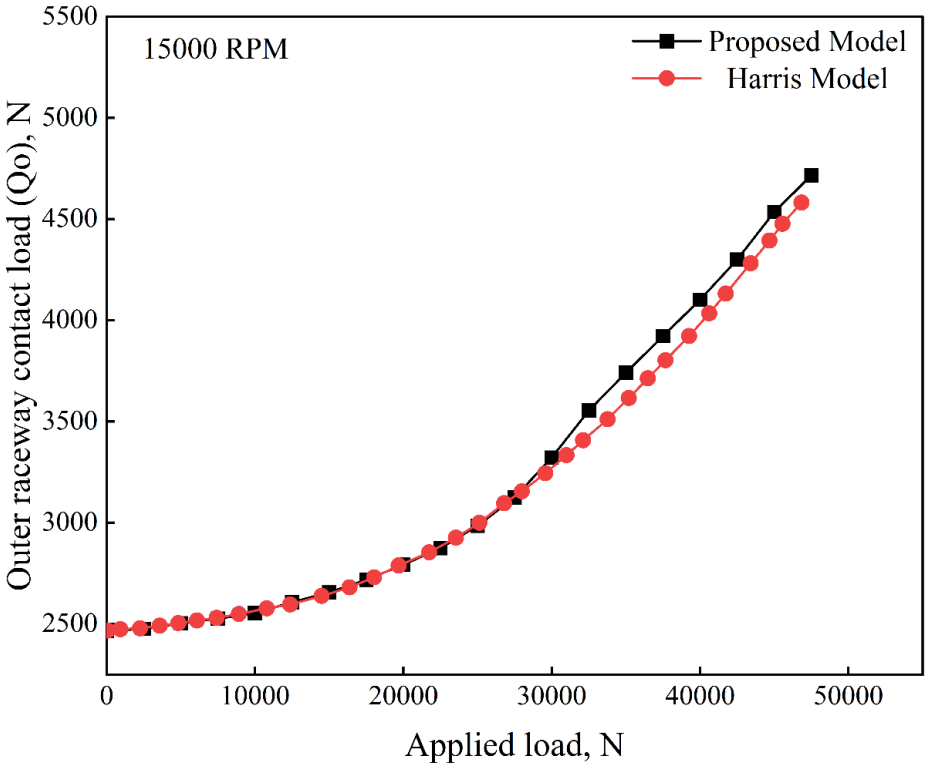

Figure 4.6: Effect of applied load on the outer raceway contact load at 15000 RPM

Proposed model								
6000 RPM			10000 RPM			15000 RPM		
Applied load	Q_i	Q_o	Applied load	Q_i	Q_o	Applied load	Q_i	Q_o
0	1.78968	384.461	0	35.9419	1093.11	0	8.00545	2653.04
2500	194.814	450.095	2500	169.633	1128.19	2500	239.153	2644.19
5000	424.9	640.762	5000	403.163	1211.09	5000	578.25	2747.92
7500	342.456	792.564	7500	660.342	1271.56	7500	726.105	2631.41
10000	1047.27	1074.86	10000	866.953	1410.1	10000	830.548	2619.37
12500	1169.46	1357.36	12500	1073.33	1628.34	12500	1020.86	2636.97
15000	1427.28	1570.06	15000	1331.2	1809.77	15000	1174.94	2748.29
17500	1611.67	1795.43	17500	1577.55	2035.55	17500	1229.47	2718.05
20000	1904.52	2009.31	20000	1761.22	2162.78	20000	1460.25	2838.68
22500	2131.07	2235.59	22500	1997.94	2387.5	22500	1645.21	2922.15
25000	2341.74	2435.55	25000	2241.99	2605.05	25000	1859.03	3050.25
27500	2567.4	2674.39	27500	2449.95	2825.02	27500	2053.79	3174.72
30000	2786.48	2902.62	30000	2633.51	3014.51	30000	2249.85	3347.49
32500	2999.12	3117.41	32500	2879.54	3241.85	32500	2453.11	3561.83
35000	3214.26	3347.28	35000	3112.83	3494.62	35000	2646.23	3744.93
37500	3403.01	3566.04	37500	3303.69	3706.09	37500	2864.42	3915
40000	3640.61	3812.24	40000	3519.47	3928.01	40000	3064.95	4124.77
42500	3811.63	4051.01	42500	3715.46	4142.06	42500	3279.85	4318.46
45000	4014.13	4268.5	45000	3884.31	4368.07	45000	3323.1	4550.87
47500	4224.85	4495.05	47500	4088.62	4599.69	47500	3675.61	4774.92
Harris model								
6000 RPM			10000 RPM			15000 RPM		
Applied load	Q_i	Q_o	Applied load	Qi	Qo	Applied load	Q_i	Q_o
0	9.66	351.38	0	15.6165	1072.79	0	7.58	2466.9
2500	189.47	449.85	2500	162.312	1092.16	2500	149.4	2480.61
5000	437.95	640.5	5000	387.471	1168.54	5000	309.07	2505.39
7500	714.2	908.27	7500	643.342	1234.86	7500	463.42	2530.22
10000	949.22	1123.14	10000	849.289	1385.48	10000	639.34	2564.71
12500	1198.27	1354.74	12500	1070.62	1607.48	12500	820.51	2598.55
15000	1415.64	1561.16	15000	1307.58	1771.96	15000	1006.57	2649.11
17500	1647.73	1790.03	17500	1552.86	1997.77	17500	1214.2	2714.07
20000	1900.87	2000.34	20000	1765.94	2139.35	20000	1411.8	2798.15

22500	2131.17	2223.27	22500	1983.67	2350.69	22500	1617.86	2883.83
25000	2337.3	2430.59	25000	2220.63	2576.19	25000	1828.23	2993.45
27500	2564.82	2669.95	27500	2427.96	2795.3	27500	2037.57	3130.85
30000	2782.28	2894.66	30000	2633.38	2989.86	30000	2236	3320.63
32500	2997.12	3110.38	32500	2870.52	3226.63	32500	2441.85	3531.72
35000	3208.99	3335.94	35000	3091.66	3464.39	35000	2645.18	3700.7
37500	3391.1	3553.19	37500	3298	3689.79	37500	2852.23	3889.49
40000	3624.95	3798.78	40000	3500.57	3897.62	40000	3054.2	4092.95
42500	3829.34	4042.15	42500	3690.52	4100.16	42500	3261.51	4290.09
45000	4018.27	4257.92	45000	3860.71	4333.45	45000	3459.15	4523.42
47500	4208.71	4482.4	47500	4000.9	4564.12	47500	3656.65	4735.53

Table 4. 2: Compassions among the proposed model and Harris model regarding normal contact loads

4.4. Effect of applied load on the ball raceway contact angles at various speeds

This study further investigates the variation in ball-raceway contact angles—inner (α_i) and outer (α_o)—as a function of applied axial load (Fa) across three rotational speeds (6000, 10000, and 15000 RPM), comparing predictions from the classical Harris model and a newly proposed model as given numerically in Table 4.3.

Figure 4.7 (a), at 6000 RPM and zero axial load, both models yield similar inner contact angles, with the Harris model predicting α_i= 58.64° and the proposed model giving 58.63°, indicating strong agreement under unloaded conditions. However, as the axial load increases, notable differences emerge. The proposed model consistently predicts slightly lower inner contact angles and slightly higher outer contact angles than the Harris model across the load range. For instance, at F = 15000 N, the proposed model predicts α_o = 36.35° compared to 36.35° in the Harris model, but the trend diverges subtly with increasing load. This suggests that the proposed model may introduce modified compliance characteristics or additional non-linearities in contact behavior not captured by the Harris model.

Figure 4.7 (b), at a moderate speed of 10000 RPM, both models maintain similar trends, with α_i decreasing and α_o increasing as the axial load increases. However, the proposed model shows more pronounced deviations from the Harris model at lower loads. At Fa

= 2500 N, the proposed model estimates $\alpha_i = 58.78°$ and $\alpha_o = 5.49°$, slightly higher than Harris's 58.77° and 5.39°, respectively. These differences persist but become less distinct at higher loads. The slight divergence implies the proposed model incorporates additional dynamic effects or speed-dependent corrections, offering potentially improved realism at low-to-moderate load levels.

Figure 4.7 (c), at the highest investigated speed of 15000 RPM, the distinction between the two models becomes more evident, particularly at lower axial loads. The proposed model predicts noticeably larger outer contact angles under no load ($\alpha_o = 0.114°$ vs. 0.000° in Harris), and the discrepancy remains visible at Fa = 2500 N (3.19° vs. 2.48°). These differences suggest that the proposed model accounts for centrifugal force effects or gyroscopic influences more comprehensively. At higher loads (≥ 15000 N), both models converge again, indicating that load dominates over speed effects in determining contact angles under such conditions.

Across all speeds, both models affirm the expected mechanical behavior: increasing axial load leads to decreasing α_i and increasing α_o, signifying load transfer from the inner to outer raceway. However, the proposed model introduces refinements that result in marginally higher α_o values and smoother transitions across speed regimes, especially in the low-load regions.

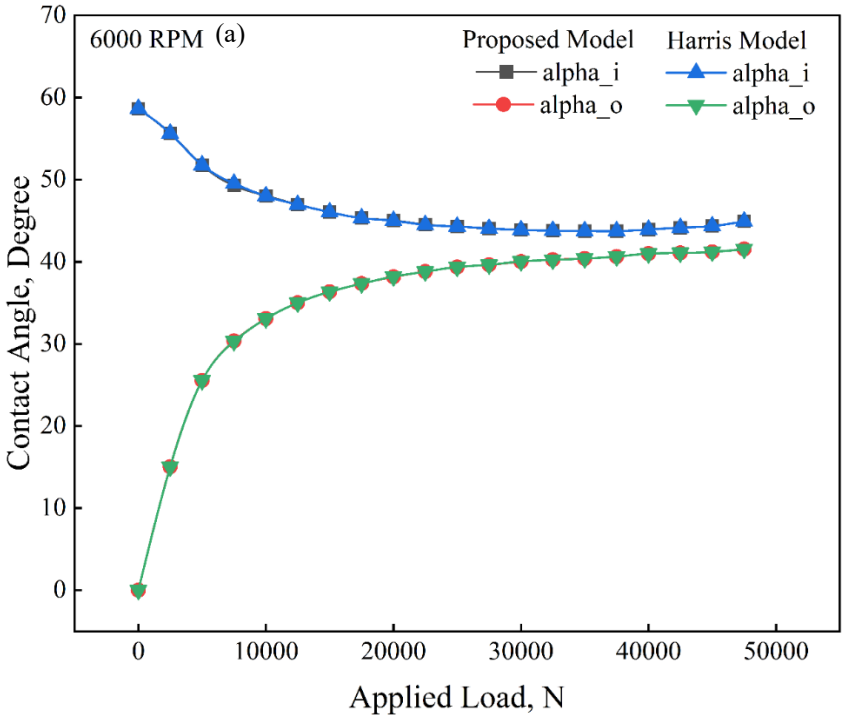

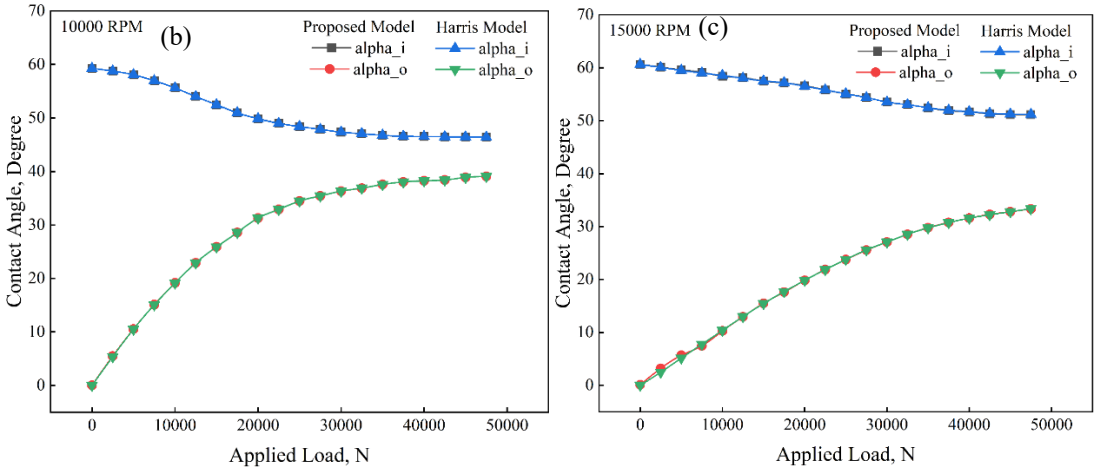

Figure 4. 7: Effect of applied load on the ball raceway contact angles at various speeds, (a) 6000 RPM, (b) 10000 RPM, and (c) 15000 RPM

The following table shows a compassion among the proposed model and Harris model regarding contact angles.

Proposed Model								
6000 RPM			10000 RPM			15000 RPM		
Fa	alpha_i	alpha_o	Fa	alpha_i	alpha_o	Fa	alpha_i	alpha_o
0	58.63517	0.004385	0	59.2623	0.038003	0	60.63319	0.114278
2500	55.63946	15.02453	2500	58.77843	5.493453	2500	60.10565	3.187569
5000	51.76139	25.53836	5000	58.07191	10.54339	5000	59.60685	5.678759
7500	49.28429	30.36512	7500	56.94735	15.10163	7500	59.13281	7.45142
10000	48.02497	33.06693	10000	55.60329	19.17624	10000	58.40285	10.26956
12500	46.94271	35.00643	12500	53.99552	22.90551	12500	58.12259	12.95247
15000	46.04441	36.34531	15000	52.47787	25.89579	15000	57.48864	15.51054
17500	45.31592	37.33357	17500	50.9651	28.58629	17500	57.1314	17.62671
20000	45.01074	38.1704	20000	49.86769	31.2827	20000	56.6092	19.82602
22500	44.5026	38.79267	22500	49.00514	32.90527	22500	55.81312	21.87419
25000	44.28952	39.34587	25000	48.39105	34.48366	25000	55.08888	23.75425
27500	44.04068	39.63048	27500	47.8585	35.42836	27500	54.37885	25.54614
30000	43.88877	40.0229	30000	47.33842	36.31732	30000	53.50742	27.05747
32500	43.79205	40.23892	32500	47.06131	36.8787	32500	53.02002	28.53198
35000	43.75723	40.39598	35000	46.76599	37.57403	35000	52.43175	29.79198

37500	43.75004	40.62301	37500	46.55728	38.03014	37500	51.90677	30.76456
40000	43.92617	40.97924	40000	46.51749	38.25859	40000	51.67781	31.57762
42500	44.15562	41.06354	42500	46.48084	38.39489	42500	51.31281	32.28324
45000	44.34086	41.19961	45000	46.44286	38.88892	45000	51.17524	32.7966
47500	44.91073	41.53507	47500	46.406	39.07689	47500	51.15488	33.32411
Harris Model								
Fa	alpha_i	alpha_o	Fa	alpha_i	alpha_o	Fa	alpha_i	alpha_o
0	58.64	0	0	59.25894	0	0	60.632	0
2500	55.64	15.0182	2500	58.7732	5.385	2500	60.064	2.476
5000	51.76	25.5443	5000	58.0733	10.508	5000	59.511	5.139
7500	49.51	30.3168	7500	56.9405	15.087	7500	59.011	7.764
10000	47.99	33.0827	10000	55.6015	19.161	10000	58.549	10.394
12500	46.95	35.0071	12500	53.9933	22.904	12500	58.027	12.969
15000	46.04	36.3488	15000	52.4726	25.898	15000	57.496	15.457
17500	45.32	37.3371	17500	50.9659	28.585	17500	57.178	17.698
20000	45.01	38.1784	20000	49.8638	31.288	20000	56.506	19.836
22500	44.5	38.7994	22500	49.0003	32.908	22500	55.818	21.857
25000	44.29	39.3491	25000	48.3965	34.482	25000	55.084	23.783
27500	44.04	39.639	27500	47.8697	35.431	27500	54.369	25.571
30000	43.88	40.0245	30000	47.3461	36.328	30000	53.526	27.073
32500	43.79	40.2318	32500	47.0606	36.887	32500	53.021	28.53
35000	43.75	40.3925	35000	46.7699	37.577	35000	52.457	29.731
37500	43.75	40.6245	37500	46.562	38.039	37500	51.988	30.74
40000	43.92	40.9796	40000	46.522	38.261	40000	51.699	31.59
42500	44.16	41.0674	42500	46.482	38.397	42500	51.394	32.228
45000	44.34	41.1944	45000	46.4421	38.894	45000	51.238	32.792
47500	44.91	41.5329	47500	46.4021	39.077	47500	51.198	33.368

Table 4. 3: Comparisons among the proposed model and Harris model regarding contact angles

4.5. Effect of applied load on the bearing friction at various speeds

The friction torque due to spinning exhibits a strong dependency on both applied axial load and rotational speed, Figure 4.8 (a). At zero load, the friction torque remains minimal across all speeds, with a notable anomaly at 10000 RPM where the torque spikes to 4.06 N·mm compared to only 0.20 and 0.93 N·mm at 6000 and 15000 RPM, respectively. As the axial load increases, friction torque rises sharply, reflecting intensified ball-raceway interaction and increased spin resistance. At 6000 RPM, the torque increases steadily, reaching 371.95 N·mm at 47500 N, highlighting a near-linear trend. In contrast, the behavior at 10000 and 15000 RPM reveals non-linear characteristics; for example, at 15000 RPM, the friction torque grows rapidly up to 25000 N, then continues increasing at a slower rate. Interestingly, at higher loads (≥ 20000 N), the values at 10000 RPM surpass those at 15000 RPM, suggesting that the interplay between speed-induced centrifugal effects and load-dependent spin friction is non-monotonic. This trend underscores the complex interaction between speed, axial force, and frictional energy loss due to ball spinning, emphasizing the need for refined modeling when predicting thermal and mechanical behavior in high-speed bearing applications.

The bearing friction torque attributed to applied load exhibits a clear and consistent monotonic increase with axial loading, independent of rotational speed, Figure 4.8 (b). Across all three speeds—6000, 10000, and 15000 RPM—the friction torque values remain identical at each load level, confirming that this component of friction is governed solely by the magnitude of the applied load rather than dynamic effects. The relationship between load and friction torque is non-linear, reflecting the increasing deformation and internal resistance at the contact interface between rolling elements and raceways as the load rises. Starting from zero torque under no load, the values increase gradually—reaching approximately 12.29 N·mm at 10000 N and surging to 277.37 N·mm at 47500 N. This behavior is characteristic of classical rolling contact mechanics, where the torque due to load grows with the normal force and contact area. The independence from speed further distinguishes this load-induced torque from speed-sensitive components like spin friction, highlighting the necessity of decomposing total friction torque into its fundamental constituents for accurate bearing performance modeling and thermal prediction.

The viscous friction torque, Figure 4.8 (c), demonstrates a constant behavior with respect to applied axial load, remaining unchanged across all load values from 0 to 47500 N. This is consistent with the theoretical understanding that viscous torque is primarily a function of rotational speed and lubricant properties, rather than mechanical load. At 6000 RPM, the viscous torque is approximately 278.17 N·mm, increasing to 391.03 N·mm at 10000 RPM and further to 512.39 N·mm at 15000 RPM. These values clearly show a direct dependency on speed, reflecting the increased shearing action within the lubricant film at higher velocities. The invariance of torque with load indicates that the hydrodynamic lubrication regime remains stable and is not significantly influenced by contact pressure within the tested range. This emphasizes that, in high-speed applications, viscous drag becomes a dominant source of friction, especially under light or moderate loading, and must be considered in thermal and power loss calculations even when mechanical load effects are minimal.

The total friction torque on the bearing is the cumulative result of three primary components: viscous friction, spin-induced friction, and load-dependent rolling friction, Figure 4.8 (d). The data reveals a consistent increase in total torque with applied axial load across all examined rotational speeds—6000, 10000, and 15000 RPM. At zero load, the total torque corresponds exactly to the viscous friction component, confirming that in the absence of load, only lubricant shear contributes significantly to torque. As the axial load increases, the total friction torque rises non-linearly, driven by the growing influence of both spin friction and load-dependent rolling resistance. Notably, the rate of increase is more pronounced at higher speeds. For instance, at 47500 N, the total torque reaches 555.54 N·m at 6000 RPM, 668.40 N·m at 10000 RPM, and 789.76 Nm at 15000 RPM. This highlights the compounded effect of speed on spin and viscous losses, emphasizing that in high-speed, heavily loaded applications, spin and viscous friction significantly dominate the total torque. The clear additive nature of the torque components in this data validates the modeling approach and reinforces the necessity of accounting for all three sources of friction in predictive bearing performance analysis.

The frictional power loss in rolling element bearings is a critical factor influencing efficiency and thermal behavior, especially in high-speed applications. The presented data in Figure 4.9 delineate the distribution of power loss between the inner and outer raceways as a function of applied axial load at three speeds: 6000, 10000, and 15000

RPM. At zero load, the power losses are minimal and with increasing load, power loss increases sharply in both raceways, with the inner raceway consistently exhibiting higher loss values. For example, at 25000 N and 15000 RPM, the inner raceway loss reaches 2026.67 W compared to 1275.54 W for the outer raceway, emphasizing the more significant energy dissipation near the driving interface. As speed increases, the total frictional power loss also rises substantially due to enhanced spin, viscous drag, and sliding effects. The difference in losses between the raceways becomes more pronounced at higher loads and speeds, suggesting asymmetric load distribution and possible differences in local sliding velocities. This trend underscores the importance of considering both raceways separately in thermal and energy efficiency analyses, as the inner raceway—often in direct contact with the driving shaft—serves as the primary locus for frictional energy dissipation, especially under high-speed and high-load conditions.

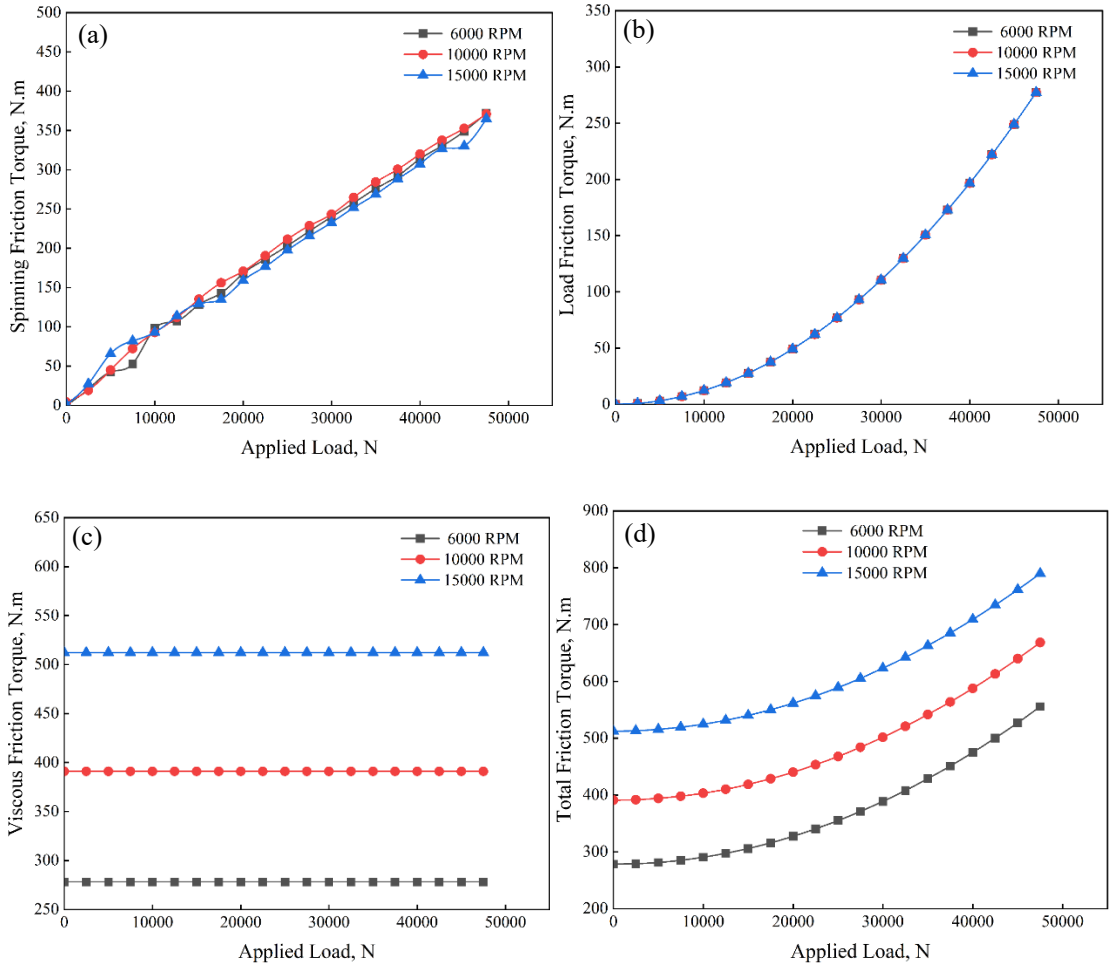

Figure 4.8: Effect of applied load on the bearing friction at various speeds, (a) spinning friction, (b), Load friction, (c) Viscous friction, and (d) Total friction torque

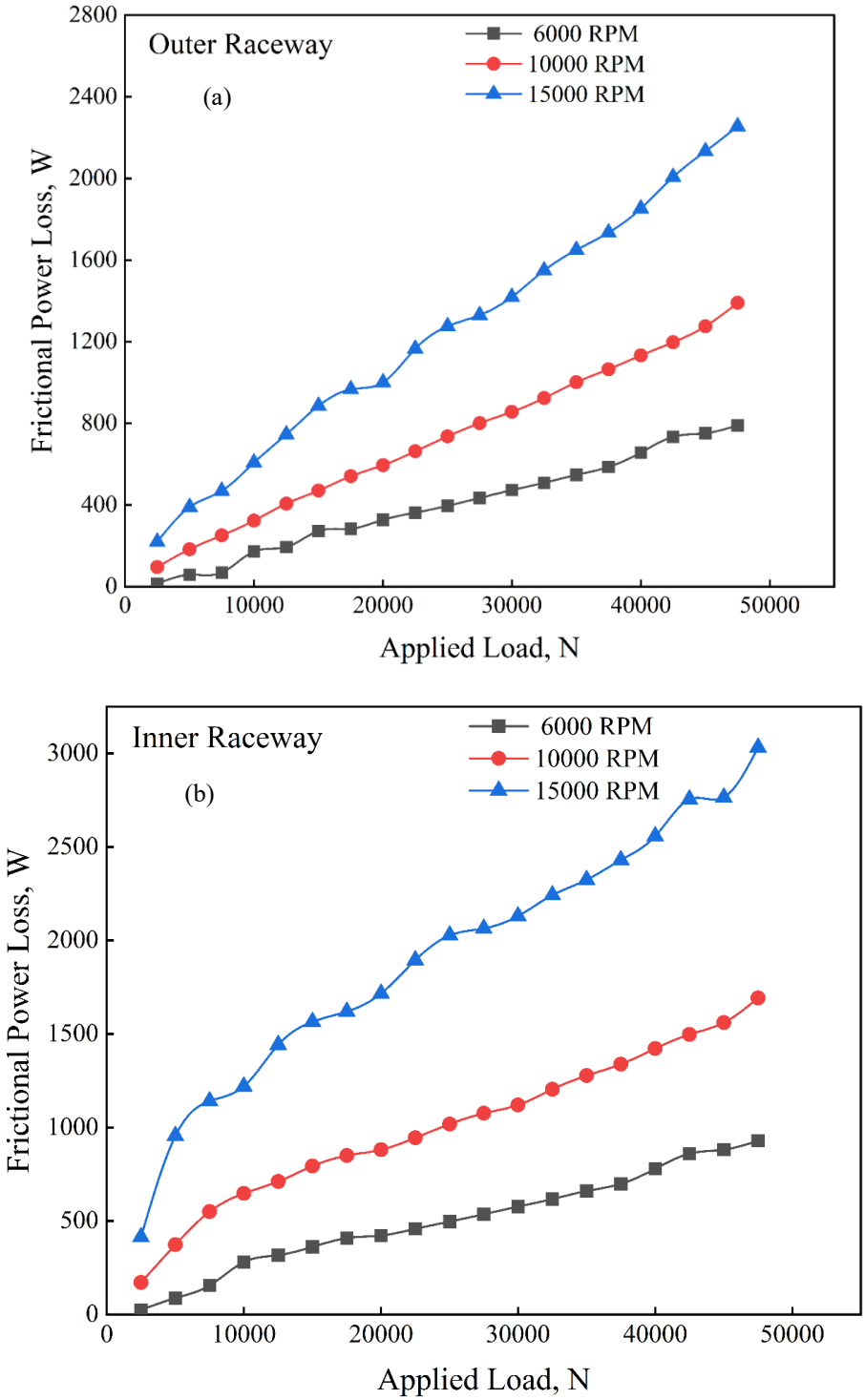

Figure 4.9: Effect of applied load on the friction power loss at various speeds regarding (a) Outer raceway and (b) Inner raceway

4.6. Effect of applied load on the generated heat at various speeds

The heat generated due to spinning friction in ball bearings is a major contributor to the overall thermal load, particularly at elevated rotational speeds. The provided data in Figure 4.10 (a) clearly demonstrate a significant increase in spinning-induced heat generation with both rising axial load and speed. At zero load, spinning heat is already considerable—289.41 W at 6000 RPM, increasing to 737.08 W and 1378.08 W at 10000 and 15000 RPM, respectively—highlighting the role of centrifugal effects and lubricant drag even in unloaded conditions. As the load increases, the heat generation rises sharply, reaching 1444.06 W at 6000 RPM, 2713.51 W at 10000 RPM, and an extensive 4721.48 W at 15000 RPM under a 47500 N axial load. The non-linear trend in the data suggests a complex interplay between increasing spin velocities, contact forces, and micro-slip behavior within the contact zones. Interestingly, at lower loads (e.g., 7500 N), fluctuations such as a slight dip at 6000 RPM may indicate transient changes in the spin-slip relationship or local changes in contact angle dynamics. Overall, the data confirm that spinning friction heat becomes a dominant thermal factor at high-speed and high-load conditions, necessitating robust thermal management strategies in bearing design to avoid excessive temperature rise and lubricant degradation.

The viscous friction heat generation rate, driven primarily by the shearing of lubricant films within the bearing clearance, shows a clear dependence on both rotational speed and applied axial load, Figure 4.10 (b). As expected, viscous heat generation increases significantly with speed: at zero load, it measures 292.79 W at 6000 RPM, 685.97 W at 10000 RPM, and 1348.31 W at 15000 RPM. This relationship aligns with the well-established behavior of fluid friction, where heat generation scales with the square of speed. Unlike the spinning and load-related friction components, viscous heating also exhibits a modest but continuous increase with rising load. For instance, at 15000 RPM, the heat generation grows from 1348.31 W at zero load to 2078.18 W at 47500 N. This load-dependence, though secondary to speed effects, likely results from the increased churning and localized film pressure in response to tighter internal clearances under load. Additionally, the gradual and monotonic rise in all three speed categories underscores the stable and predictable nature of viscous dissipation. These findings reinforce that in high-speed bearing applications, viscous friction can become the dominant thermal contributor, especially under sustained loads, and must be accounted

for in lubrication and thermal management strategies to ensure system reliability and efficiency.

The load-induced frictional heat generation rate reflects the thermal energy dissipated due to rolling and sliding resistance under applied axial loads. Unlike viscous and spinning friction, this component is solely dependent on load and remains invariant with respect to rotational speed, Figure 4.10 (c). This behavior is consistent with the theoretical basis of load-related friction, which arises from the normal contact forces between rolling elements and raceways, independent of lubricant shear or spin effects. As shown in the data, no heat is generated at zero load, and the heat generation increases linearly with load across all speeds. For instance, at 15000 N, the heat generation reaches 1149.19 W, and at the maximum tested load of 47500 N, it rises to 3639.10 W—identical across 6000, 10000, and 15000 RPM. This linear trend emphasizes the dominant role of mechanical contact over kinematic effects in this friction mode. Although speed does not directly affect this component, the total thermal behavior of the bearing system cannot be fully understood without accounting for the additive effects of load, viscous, and spin-induced heat. Thus, the load friction heat generation serves as a predictable and significant contributor to the overall thermal load, particularly in high-force, moderate-speed applications where it may rival or even exceed other forms of frictional heating.

The total frictional heat generation rate in the bearing system represents the cumulative thermal energy dissipated from all primary friction mechanisms: viscous shear, spinning friction, and load-induced rolling resistance. The data in Figure 4.10 (d) clearly illustrate that total heat generation increases significantly with both applied axial load and rotational speed. At zero load, the total heat is dominated by viscous and spin components, with values of 582.20 W at 6000 RPM, 1423.05 W at 10000 RPM, and 2726.39 W at 15000 RPM. As the load increases, the total heat generation rate rises markedly due to the additive effects of load-dependent and spin-related friction, reaching 5667.90 W, 7525.16 W, and 10438.76 W at 47500 N for 6000, 10000, and 15000 RPM, respectively. Notably, the heat generation grows nonlinearly with load, particularly at higher speeds, indicating compounding interactions between spin friction and load-induced contact deformation. The increasing gap between values across speeds at higher loads highlights the strong influence of rotational speed on total thermal dissipation. This comprehensive thermal profile underscores the need for

accurate modeling of all friction sources in high-performance bearing systems and highlights the critical importance of effective cooling and lubrication strategies to mitigate temperature rise, reduce wear, and ensure reliable operation under high-load, high-speed conditions.

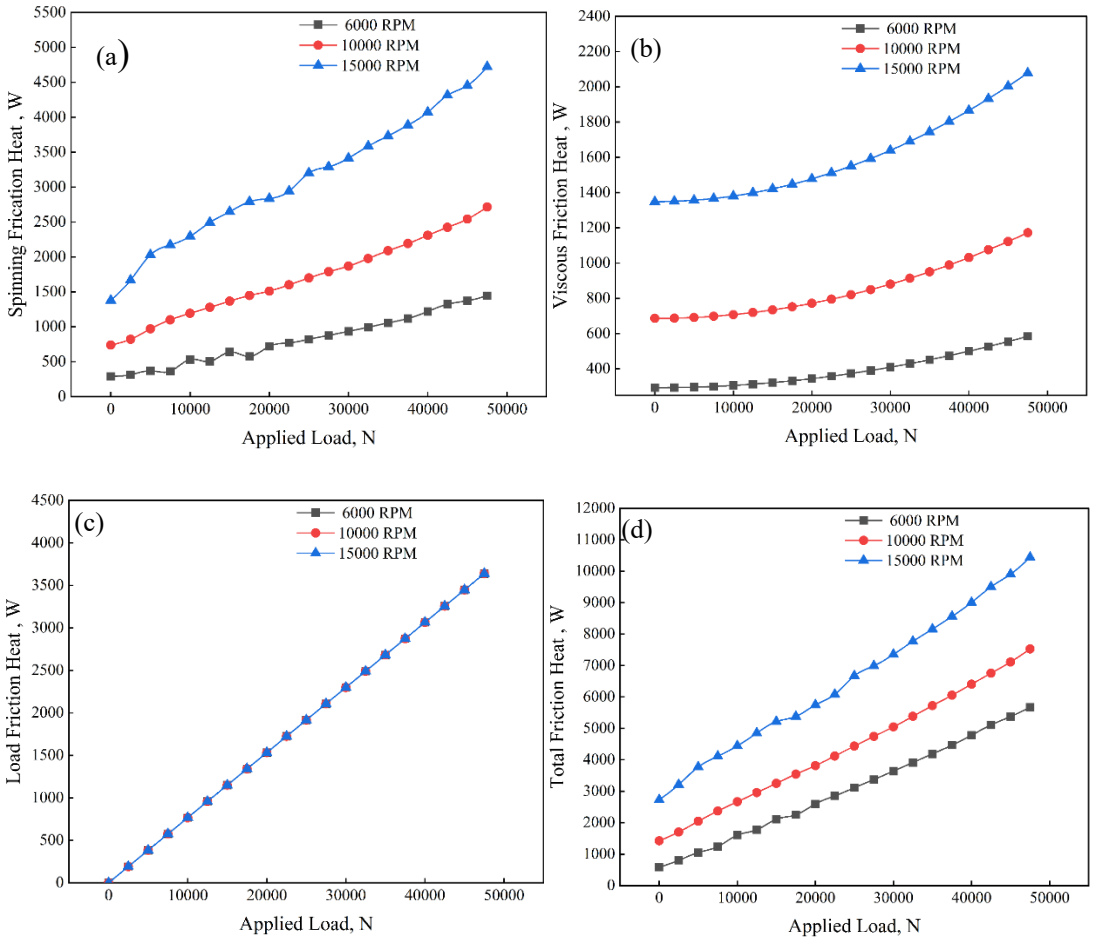

Figure 4.10: Effect of applied load on the bearing friction heat generated at various speeds, (a) spinning friction heat, (b), Viscous friction heat, (c) Load friction heat, and (d) Total friction heat

4.7. Effect of applied load on the bearing fatigue life at various speeds

The basic dynamic capacity (Qc) of the ball-raceway contact quantifies the load-carrying capability of the bearing elements under dynamic conditions. The data in Figure 4.11 show a clear influence of both applied axial load and rotational speed on the distribution of Qc between the inner and outer raceways. As expected, the inner raceway consistently carries a greater share of the dynamic load, especially at lower loads and speeds. For example, at 2500 N and 6000 RPM, Qc for the inner raceway is 17,570.74 N compared to 27,865.04 N on the outer raceway—highlighting a more

significant load transfer path through the inner race due to initial contact angle orientation and structural stiffness. However, with increasing axial load, Qc values for both raceways gradually decrease, particularly on the outer raceway, indicating a redistribution of contact stress likely due to deflection and increased angular displacement. Interestingly, higher rotational speeds result in slightly elevated Qc values for the inner raceway at corresponding loads. For instance, at 25000 N, Qc for the inner raceway increases from 16,710.59 N at 6000 RPM to 17,525.22 N at 15000 RPM, suggesting that dynamic effects such as centrifugal loading and contact angle variation with speed may help stabilize or redistribute internal load paths. The relatively modest variation in Qc at higher loads and speeds suggests the bearing operates within a relatively stable dynamic load envelope, although the shifting load distribution emphasizes the importance of accounting for both speed and load when designing for fatigue life and reliability in high-performance bearing applications.

Figure 4.12 illustrates the bearing fatigue life (in million cycles) as a function of the applied load (N) for three different rotational speeds: 6000 RPM, 10000 RPM, and 15000 RPM. The results show a clear inverse relationship between applied load and fatigue life, where an increase in applied load results in a substantial decrease in fatigue life across all three speeds. However, the trends also reveal that fatigue life is significantly influenced by rotational speed, with higher speeds generally resulting in a longer fatigue life under the same applied load conditions.

At 6000 RPM, the fatigue life starts at 141.24 million cycles for an applied load of 25000 N and gradually decreases to 24.66 million cycles at 47500 N. The trend is consistent with classical fatigue theory, where increasing the load leads to higher stress on the bearing elements, accelerating material degradation and crack propagation. A similar trend is observed at 10000 RPM, where the initial fatigue life is slightly higher at 145.58 million cycles at 25000 N but decreases more steeply compared to 6000 RPM, reaching 27.64 million cycles at 47500 N. The results suggest that the impact of load on fatigue life is more pronounced at higher rotational speeds due to additional factors such as centrifugal forces and increased dynamic loading.

At 15000 RPM, the fatigue life is significantly higher across all applied loads compared to the lower speeds. At 25000 N, the fatigue life reaches 213.31 million cycles, a substantial increase compared to the lower RPM cases. Even at the highest applied load

of 47500 N, the fatigue life remains at 45.26 million cycles, nearly double the life observed at 6000 RPM for the same load. This behavior suggests that, despite higher speeds generally leading to increased contact stresses and thermal effects, the redistribution of contact loads among the rolling elements at extreme speeds might contribute to prolonging bearing life. Additionally, the effects of elastohydrodynamic lubrication (EHL) might be more pronounced at 15000 RPM, improving load distribution and reducing direct metal-to-metal contact, thus slowing the fatigue failure process.

Interestingly, at certain load values (e.g., 35000 N at 10000 RPM), the fatigue life momentarily increases before continuing its downward trend. This could indicate complex interactions between speed, load distribution, and lubrication effects, warranting further investigation. The flattening of the fatigue life curve at 15000 RPM for higher loads (around 45000 N and above) suggests a potential stabilization effect, where the influence of applied load diminishes compared to other dominant factors, such as lubricant film thickness and thermal expansion. Recalling Equation 54, the increased centrifugal force resulting from higher rotational speeds could enhance bearing life accordingly as illustrated by Figure 4.13. The centrifugal force changes with increasing applied loads at different rotational speeds (6000, 10000, and 15000 RPM). At each speed, the centrifugal force decreases slightly as the applied load increases. However, for a given load, the centrifugal force increases significantly with higher rotational speeds. For example, at 2500 N, the force rises from approximately 291 N at 6000 RPM to over 2400 N at 15000 RPM. This confirms that centrifugal force is highly influenced by the rotating speed, while being inversely influenced by the applied load.

Overall, the findings emphasize the importance of considering rotational speed in fatigue life predictions. While high speeds introduce additional complexities like increased frictional heating and dynamic forces, they may also enhance lubrication effects and load redistribution, thereby counteracting some of the negative effects of increased applied loads. These insights are crucial for the design and maintenance of high-speed bearings in aerospace, automotive, and industrial applications, where optimizing load-bearing capacity while ensuring long operational life is critical.

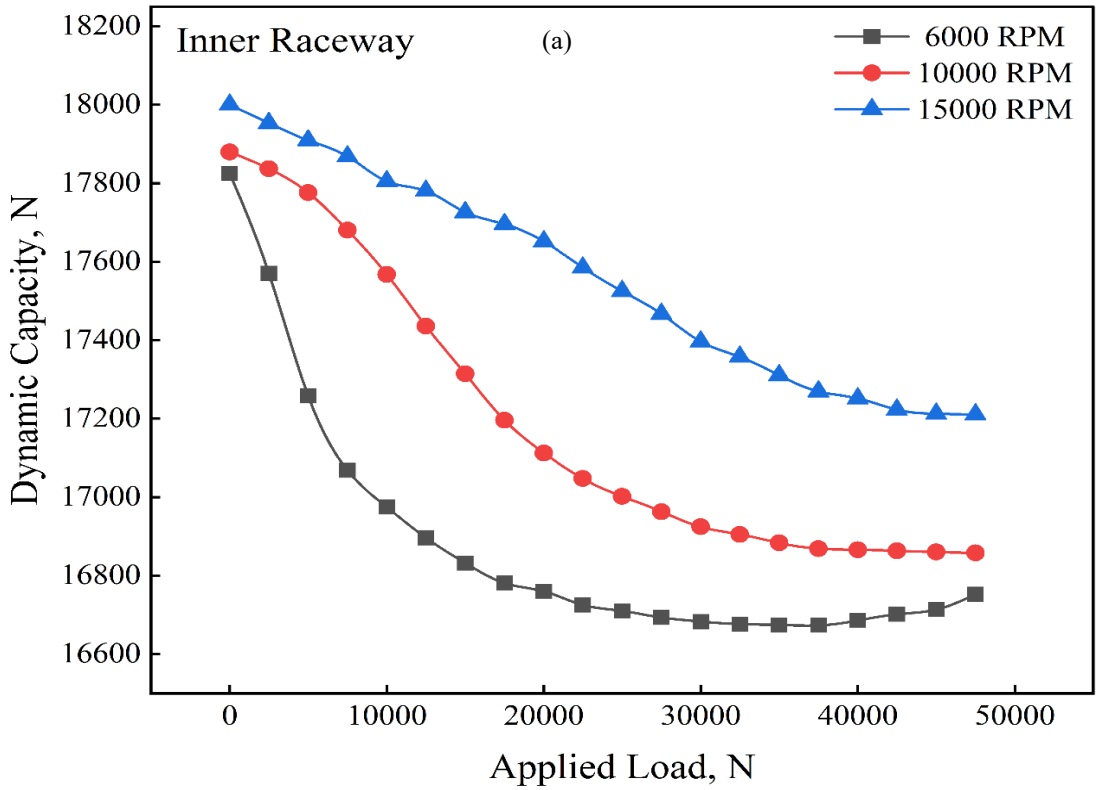

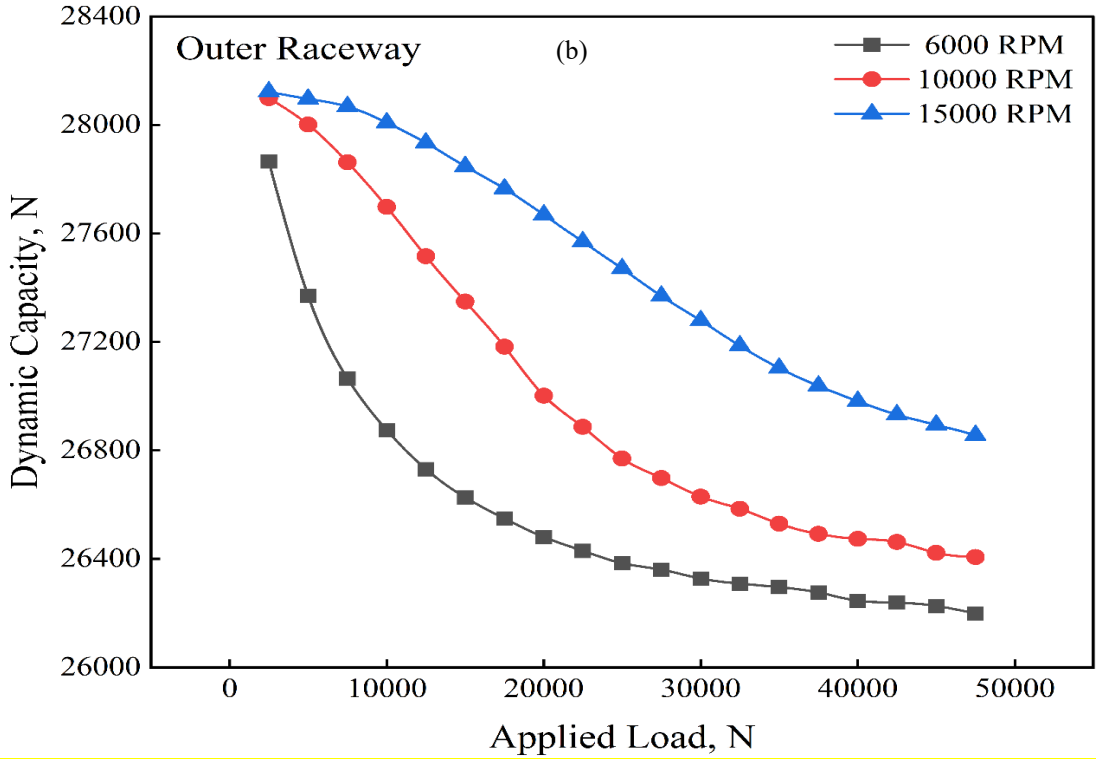

Figure 4.11: Effect of applied load on the dynamics capacity at various speeds regarding (a) inner raceway and (b) outer raceway

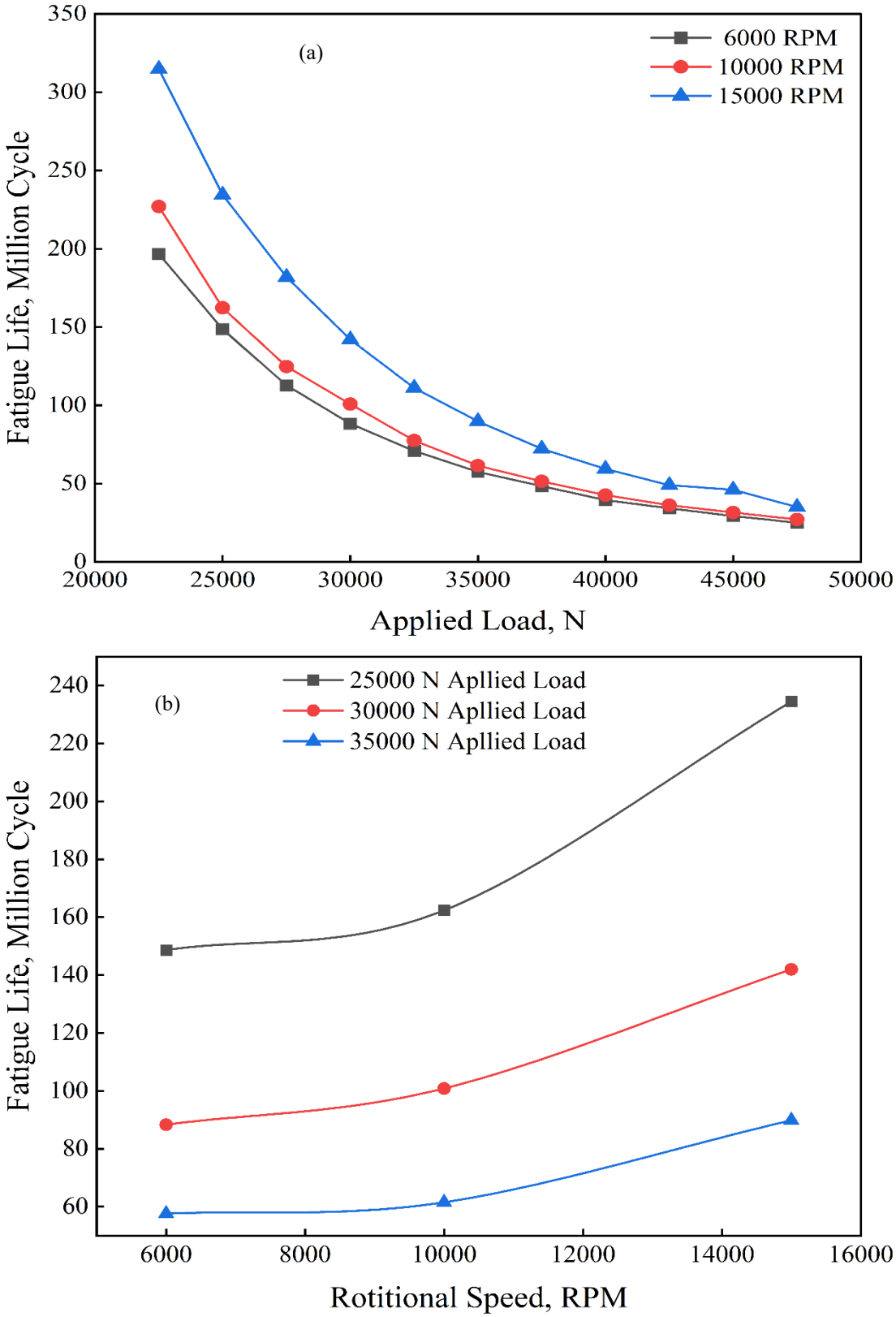

Figure 4.12: Bearing fatigue life behaviour for (a) various speeds and (b) various applied load

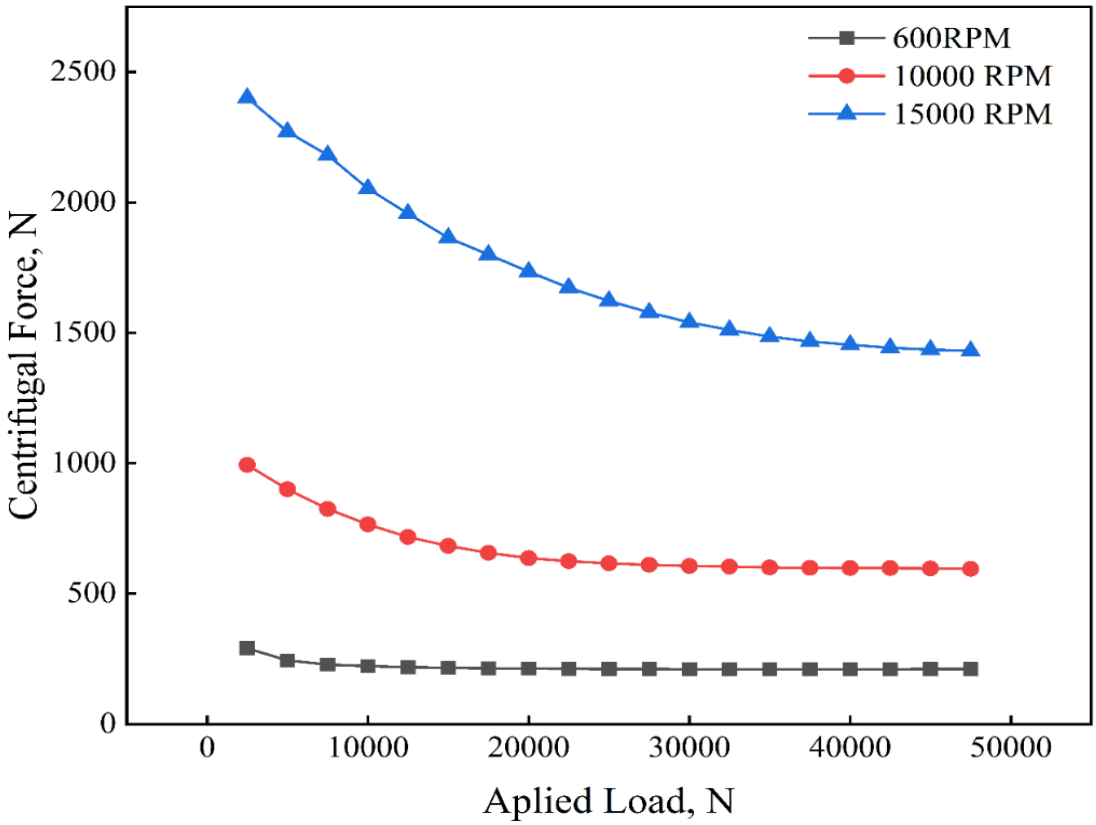

Figure 4.13: Variation of centrifugal force with applied load at different rotational speeds

4.8. Load-deflection constants of ball bearing inner raceway for different materials

The load-deflection behaviour of the bearing inner raceway at 10,000 RPM was examined for three materials: alloy steels, nickel-based superalloys, and titanium alloys, Figure 4.13. Alloy steels demonstrated the highest stiffness values, increasing from 2,903,646 N/mm² at zero load to 2,910,913 N/mm² at 47,500 N. Nickel-based superalloys followed a similar but slightly lower trend, rising from 2,800,628 to 2,807,648 N/mm². Titanium alloys exhibited the lowest load-deflection constants, increasing modestly from 1,584,934 to 1,588,994 N/mm² across the same load range. All materials showed a positive correlation between applied load and deflection resistance, with alloy steels showing the steepest increase, indicating better performance under high-load conditions.

Additionally, at a constant applied load of 40,000 N, the effect of rotational speed on stiffness was assessed. As speed increased from 6,000 to 15,000 RPM, a slight reduction

in the load-deflection constant was observed across all materials. Alloy steels decreased from 2,911,797 to 2,908,479 N/mm², nickel-based superalloys from 2,808,498 to 2,805,297 N/mm², and titanium alloys from 1,589,462 to 1,587,643 N/mm². Although the changes were relatively minor, they suggest that higher speeds can reduce structural stiffness slightly—most notably in alloy steels—due to dynamic effects such as centrifugal forces and potential thermal expansion. This behaviour should be accounted for in the design of high-speed bearing systems.

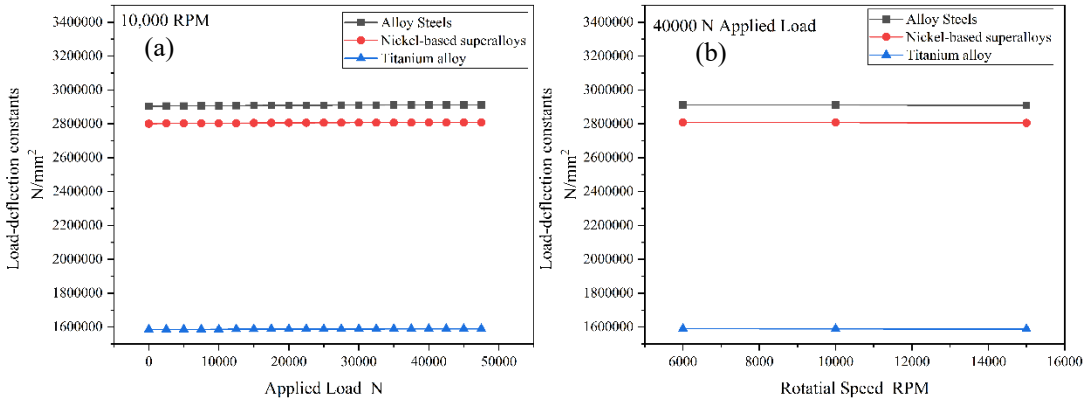

Figure 4.14: Load-deflection constants of ball bearing inner raceway for different materials with respect to (a) applied load and (b) rotating speed

4.9. The normal contact load behaviour of the bearing inner raceway for different materials

At a constant rotational speed of 10,000 RPM, the normal contact load on the inner raceway of the bearing was evaluated for alloy steels, nickel-based superalloys, and titanium alloys under applied loads ranging from 0 to 45,000 N, Figure 4.15. The results showed a non-linear increase in contact load across all materials as the applied load increased. Alloy steels consistently recorded the highest contact loads, rising from 35.94 N at no load to 3,884.31 N at 45,000 N. Nickel-based superalloys followed closely, ranging from 34.17 N to 3,872.74 N. Titanium alloys had the lowest values, from 16.05 N up to 3,441.17 N. These differences are mainly due to variations in material stiffness and elasticity, with alloy steels exhibiting superior contact resistance, making them more effective at transferring load through the raceway.

For the outer raceway, normal contact load was evaluated at a fixed applied load of 40,000 N, across rotational speeds of 6,000, 10,000, and 15,000 RPM. An increase in

contact load with speed was observed in all materials. Alloy steels showed the highest values, increasing from 3,812.24 N to 4,124.77 N. Nickel-based superalloys followed a similar trend, from 3,687.92 N to 4,004.24 N, while titanium alloys showed the lowest range, from 2,153.25 N to 2,404.37 N. These results suggest that higher speeds intensify dynamic effects—such as centrifugal force and vibration—which in turn raise the contact pressure on the outer raceway. Overall, alloy steels proved most capable of withstanding elevated contact loads, reinforcing their suitability for high-speed, high load bearing applications.

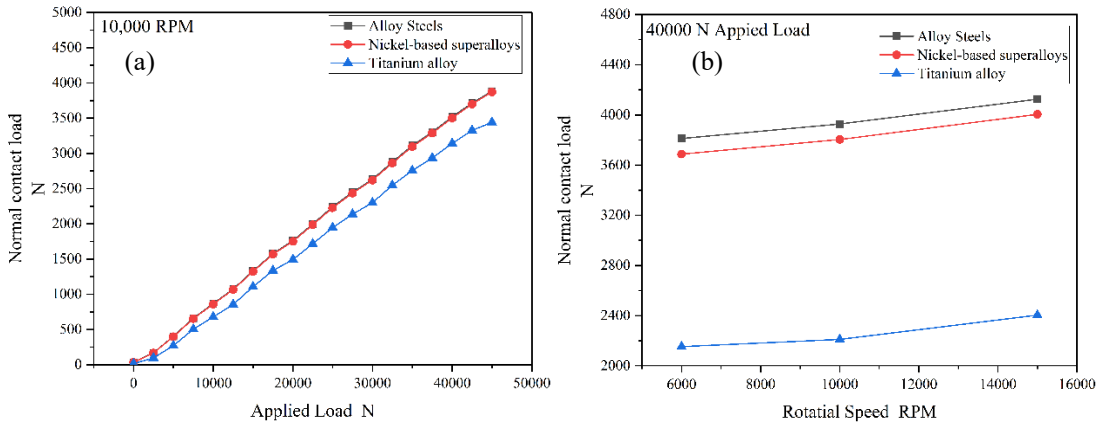

Figure 4.15: The normal contact load behaviour of the bearing inner raceway for different materials with respect to (a) applied load and (b) rotating speed

4.10. The fatigue life behaviour of the bearing across different materials

The fatigue life of the bearing at a constant speed of 10,000 RPM was evaluated under increasing applied loads for three materials: alloy steels, nickel-based superalloys, and titanium alloys. Across all materials, fatigue life decreased significantly with rising load, consistent with the inverse relationship between load intensity and bearing longevity, Figure 4.16. At zero load, titanium alloys showed the longest fatigue life, approximately 95.4 billion cycles, compared to 20.4 billion and 18.7 billion cycles for nickel-based superalloys and alloy steels, respectively. However, titanium alloys also exhibited the steepest decline in fatigue life as load increased—falling to ~65.1 million cycles at 40,000 N—indicating a higher sensitivity to loading. In contrast, alloy steels and nickel-based superalloys showed more consistent fatigue life trends across the load range, ending at ~42.6 million and ~43.6 million cycles, respectively, under the same

load. These results suggest that while titanium alloys offer superior performance under light loads, alloy steels and superalloys are more reliable for heavy-duty applications.

At a fixed 40,000 N load, fatigue life was also analysed across rotational speeds of 6,000, 10,000, and 15,000 RPM. All materials experienced reduced fatigue life with increasing speed, due to enhanced dynamic and thermal stresses. Titanium alloys maintained the highest fatigue life at each speed, decreasing from 1.81 billion to 1.41 billion cycles. Nickel-based superalloys followed, dropping from 360.4 million to 305.9 million cycles, while alloy steels showed the lowest fatigue values, declining from 326.3 million to 279.9 million cycles. These results affirm titanium's excellent high-speed endurance, though its sharp degradation rate must be considered. Meanwhile, alloy steels and superalloys provide steadier, more predictable fatigue performance under varying speed conditions, making them practical for high-speed, high-load bearing systems requiring consistent service life.

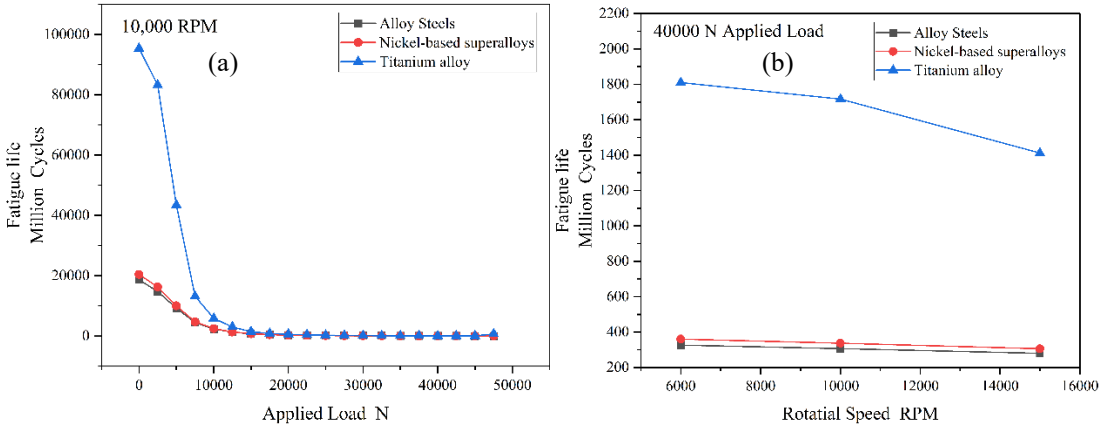

Figure 4.16: The fatigue life behaviour of the bearing across different materials with respect to (a) applied load and (b) rotating speed

Chapter 5: Description of the software

This chapter presents the detailed description of the computational approach developed to numerically solve the governing equations modeling the system's global behavior. The developed code is fully described, as well as its structure and operation, presenting an in-depth treatment of its core algorithms and functions. This chapter aims to bridge the gap between theoretical formulations and actual implementation to provide a robust and reliable computational approach.

To add clarity and content to the discussion, a series of visual representations are provided. These consist of direct screenshots of the script to unveil significant details, and graphical outputs to illustrate selected outcomes that the code generates. Furthermore, numerical data extracted and represented in Excel sheets provide an organized summary of significant findings to enable further examination and validation.

Also covered in the chapter is comparative analysis, where the results computed are graphically plotted as various representations—trend analyses and curves, say—in order to facilitate systematized comparisons with reference data provided. The comparisons are employed to verify the reliability and accuracy of the proposed methodology in displaying the effectiveness of the methodology in the prediction of the expected physical response of the system.

Through the incorporation of visual aids, tabular information, and comparative investigations, the chapter not only documents the technical implementation but also provides an informed scholarly exposition of the implication of the results. The structured approach ensures the reader is presented with a holistic picture of the computational model, its methodological strengths, and implications of the research findings for the research context in general.

5.1. MATLAB Code Description by Line Ranges

To completely solve this system—showing, saving, and exporting solutions to Excel sheet files—a variety of functions, algorithms, commands, and computing tools have been utilized to achieve accurate and reliable results. The MATLAB script utilized in

the Main-Script Windows platform exceeded 1,000 lines, reflecting the mathematical system's complexity that is being examined.

A precise and thorough examination of the operational life of angular contact ball bearings in contemporary applications such as gas turbines and jet engines—under actual operating conditions—requires serious consideration of all the variables involved. These include the loads applied, the rotational speed, the lubrication systems, the friction forces, the mechanical stresses, the thermal expansion, the heat developed due to friction, and the material properties of the metallic components of the bearings.

The interdependence of these variables renders the system very complex, which requires thorough knowledge and high-level expertise in mathematical modeling to be correctly modeled and analyzed. A few of the graphs of the MATLAB program utilized in solving the governing equations of the overall system will be presented in the following section.

5.1.1. Detailed Explanation of the MATLAB Code

This section describes in detail the MATLAB Main-Script, fully reported in Appendix A. The first section from 1 to 212 lines of the code. The first part, lines 1 to 6, aims to block interference from other processes that might run in the same computing environment. This protection helps ensure the results are valid and can be repeated, avoiding inconsistencies from overlapping operations.

Next, lines 8 to 106 outline the procedures for storing data. The computed results are saved in Excel files in an organized way. The script automatically generates these files when the numerical simulations finish, making data management and future analysis easier. Automatic file generation removes the need for manual work, improving workflow efficiency and ensuring a smooth transition to post-processing stages.

Lines 109 to 210 specify the conditions that define the types of lubrication oils used in this study and the materials of the bearing components. Three different lubricant formulations are mentioned, each with properties relevant to tribological performance and system efficiency. Additionally, the bearing components include three types of materials, all commonly used engineering alloys in mechanical systems. These

materials and oils were chosen according to industry standards and previous research, making them practical and strengthening the computational framework.

The code also includes verification checks that allow for comparing the numerical solutions with theoretical models and experimental results. These checks are necessary to validate computational solutions and identify any discrepancies. Post-processing routines are part of the code structure, enabling the visualization of key performance factors and comparisons between different lubrication and material combinations.

This MATLAB script structure highlights a systematic approach to computational modeling, with careful control over the environment, data management, and material properties. This structured method is critical for confirming the validity and applicability of the findings to real mechanical systems. The inclusion of automated processes, validation checks, and post-processing routines adds to the thoroughness of the analysis, enhancing the overall strength of the computational model for engineering design.

The second section of the MATLAB code is from line numbers 212 to 304. The section from lines 212 to 260 mainly consists of key input parameters. These parameters are the basic building blocks for the computational process. They form the first step in the mathematical modeling process by defining the main physical and operational traits of the angular contact bearing system. The inputs include the bearing's geometric dimensions, material properties, and thermal characteristics that affect its performance under different environmental conditions. Additionally, it includes key operational parameters like applied loads, rotational speed, and set operating conditions to represent real-time situations in the computational process.

These conditions involve the ambient temperature, internal heat dynamics of the system, and other assumptions that are part of the mathematical model. These assumptions are necessary to simplify complex interactions without sacrificing computational speed or accuracy. By making these assumptions clear, the script helps ensure that the following calculations meet industry standards and reference points from experiments.

Lines 263 to 304 introduce the initial values needed to start the computational procedure, ensuring stable and accurate simulation results. The initial values consist of seven key variables that act as reference points during the repeated calculation phases.

As the computational model evolves, these values serve as starting points for fine-tuning. This allows numerical algorithms to gradually minimize discrepancies between successive calculation phases. The iterative process continues until it reaches an acceptable range of error tolerance, ensuring the validity and reliability of the computational technique.

Along with clearly defined initial values and input parameters, the code includes provisions for data validation and error handling routines. These routines help confirm the results' validity by reducing the potential effects of computation anomalies and allow the generated data to fit into detailed analytical processes.

By carefully organizing input definitions, initial conditions, and validation tests, the MATLAB script presents one systematic approach to computational modeling. This helps the numerical model accurately depict physical behavior while remaining aligned with empirical observations and theory. Including iterative refinement routines also enhances the model's flexibility, making it an effective tool for analyzing the tribological and thermal performance of bearing systems under varying operating conditions.

The third section of the MATLAB code (lines 308 to 455) are the operating condition parameters, like applied load and engine speed. These parameters are the foundation for the mathematical model used in this research. Operating conditions shape how the system behaves. They directly affect performance, energy loss, and mechanical efficiency. The images include key mathematical equations that provide the theory needed for computational analysis.

Lines 308 to 340 focus on the main parameters of the mathematical model. This section lists the key variables that control physical phenomena in the system. This creates a link between the numerical outputs and experimental results. It also includes other functions that improve the performance of computational processes. These functions help with data handling, algebraic calculations, and logical tests. They are essential for ensuring the stability and reliability of the numerical outputs, which is crucial for the success of the computational plan.

In line 324 of the MATLAB code, a nested loop is used to evaluate the mechanical system’s response within a specific range of operational conditions. The simulation runs through applied loads from 0 N to 47,500 N, alongside a set of rotational speeds

between 6,000 and 15,000 RPM. This method allows for a thorough assessment of the system's dynamic behavior across all operating conditions.

At the same time, lines 346 to 473 contain mathematical equations that describe the system's behavior under different operating conditions. These equations involve various physical principles, such as kinematic relations, thermodynamic balances, and tribological interactions. They must be solved systematically within the context of the mathematical model to produce accurate results. Including these equations ensures that important aspects of the system, like load distribution, material deformation, and thermal effects, are considered in the computational simulation.

Line 395 introduces a preparatory loop that sets the angular positions of the rolling elements. The system has 16 rolling balls, and each needs specific contact angle definitions before starting any computational routines. This initialization creates a consistent and stable foundation for accurate mathematical modeling in later analyses.

For computation, the script has numerical solvers that allow for iterative solutions to equations with specified convergence tolerances. The solvers use effective mathematical methods like Newton-Raphson and finite difference approximations to improve the accuracy of the calculated values. The script also includes error mitigation techniques that prevent numerical instabilities, making the final results reliable and consistent.

By structuring the MATLAB code this way, the study creates a clear process for computational modeling. It combines necessary system parameters, governing mathematical equations, and iterative solvers into one framework. This approach ensures that the simulated results accurately represent real-world applications, making the model relevant for engineering and scientific investigations of tribological performance and mechanical system optimization.

The fourth section of the MATLAB code (lines 476 to 637) shows how the Newton-Raphson algorithm is put into practice. This algorithm is a basic and commonly used numerical method in iterative calculations. It is known for being reliable in carrying out systematic calculations, which makes it essential for mathematical applications that require iterative improvements. Thanks to its structured method for minimizing errors,

the Newton-Raphson method has become a key part of numerical analysis. It is widely used in engineering and science to solve nonlinear equations with high accuracy.

Lines 476 to 547 of the MATLAB script explain the specific implementation of the Newton-Raphson algorithm in this study. The method uses the second derivative of the function and relies on iterative feedback. In this process, computed outputs are used as new inputs for further calculations. This recursive approach gradually improves numerical estimates, helping the algorithm get closer to an accurate solution. The iterative process continues until the error margin between successive iterations is within an acceptable limit, ensuring both stability and accuracy in the final results.

At line 489 of the MATLAB code, an iterative loop applies the Newton-Raphson algorithm across all 16 discrete positions of the rolling elements. For each position, the solver works on nonlinear equations related to contact angles, forces, and deformation until it reaches convergence. This loop enables the model to consider local mechanical variations, such as contact geometry and friction impacts, caused by different positions of the elements. Its design promotes both numerical stability and physical accuracy, which is particularly important in challenging operating conditions that involve nonlinear material behavior and thermal effects.

Moreover, the Newton-Raphson algorithm shows a fast convergence rate under suitable conditions, making it especially useful for solving equations where analytical solutions are difficult or time-consuming. By using adaptive methods, the algorithm changes step sizes and directions to improve computational efficiency. The script is crafted to integrate these adjustments smoothly, helping the numerical model stay reliable with different input parameters.

The section from lines 538 to 543 includes a convergence loop based on a check that ensures thermal balance in the system. Specifically, the routine keeps iterating until the temperature difference between the inlet and outlet drops below 0.1 °C. Once this condition is met, the solver records the results and assesses the bearing's operating life and other temperature-sensitive factors. If it does not converge, the loop triggers recalculations and updates properties. This ensures that thermal expansion, which directly affects contact mechanics, stress distributions, lubricant rheology, and material behavior, is accurately factored into the overall model.

Meanwhile, lines 548 to 681 of the MATLAB code contain a set of important equations needed for calculations within this mathematical framework. These equations govern key interactions in the system, covering both algebraic and differential expressions that

define the physical and thermal properties of the model. Including these equations makes sure the Newton-Raphson algorithm works within a clear mathematical structure, supporting the accuracy of iterative calculations.

To improve numerical stability, the script includes strategies for reducing errors and assessing convergence. These efforts help prevent computational problems, ensuring the iterative process remains consistent even with extreme initial conditions or function discontinuities. By adding these safeguards, the numerical framework retains its reliability across various engineering and scientific uses.

Through careful structuring of the Newton-Raphson implementation and its related mathematical elements, this part of the MATLAB script demonstrates a thorough approach to computational modeling. The organized integration of iterative refinement, error reduction methods, and essential governing equations ensures that the numerical analysis is both accurate and efficient. Applying these principles enhances the reliability of results, making the methodology highly relevant for real-world engineering simulations and optimization challenges.

The fifth section of the MATLAB code (lines 684 to 843) presents key characteristics of the MATLAB script responsible for real-time result visualization and outcome saving. This piece of code is crucial for enhancing the user experience through dynamic monitoring of computational development. Real-time information display utilization offers users the capability to assess intermediate results, detect anomalies, and verify numerical solution correctness while running the script. This feature is also convenient for debugging and performance tuning through real-time feedback for parameter modifications.

Lines 684-693 contain commands specifically to enable critical output values to be printed directly into MATLAB's Command Window right away. These values, printed at major stages of execution, give users immediate feedback on the evolving solution, enabling real-time assessment to be made without having to access data externally. Through the inclusion of this capability, the script enables an interactive computation process where users can observe system behavior and numerical convergence in real-time.

Concurrently, lines 694-794 hold specifications that are solely responsible for storing final output data in organized Excel files. The storage mechanism of data guarantees computational output to be well-recorded in an organized fashion to facilitate post-

processing, comparative analysis, and external documentation. Both the primary and secondary Excel files are automatically created by the script upon completion of the computational task to guarantee redundancy of data and preserve the crucial information for further assessments. The two-file solution helps to maintain data integrity to prevent risks of unintended alterations or computational errors.

Apart from this, the structured storage plan of data in the MATLAB script ensures maximum accessibility since the numerical output is exhibited in pre-defined cell locations in the Excel spreadsheets. The well-structured output display makes it simple to interface with external analysis packages such that the user can perform higher-level statistical analysis, graphical plots, and other mathematical operations with ease. By integrating the storage functions into the procedure of computation, the script ensures maximum efficiency with the least intervention and maximum integrity in data retrieval operations.

In addition to the elementary task of real-time visualization and storage, the script also provides for the verification of stored outputs against theoretical calculations and experimental measurements. The verification procedures are what provide credibility to the computational results, allowing one to make an informed decision in engineering application. The provision of visualization and storage facilities in this section of the MATLAB code demonstrates an integrated approach to numerical analysis, with methodological discipline being facilitated and computational model robustness being encouraged.

The sixth section of the MATLAB code (lines 836 to 1020) demonstrates a significant part of the MATLAB script used in visualization of computed outcomes in graphical plot format. This code segment has a key role in analysis and interpretation of numerical outcomes by transforming raw computational results into useful plots. Graphical depiction of key results facilitates intuitive identification of system behavior, trend estimation, and comparative observations under varying operating conditions.

Lines 837 to 964 are specifically charged with selecting key outcomes from the resultant output and preparing them for visualization within MATLAB's plotting framework. This segment of the script employs top-level commands that enable key system parameters to be represented graphically, so users can visually track how force distributions, thermal behavior, or mechanical interactions evolve. With the inclusion

of robust plotting capabilities, the script enables more intensive data analysis, with real-time assessment of parameter sensitivities and the effects of iterative improvements on overall system performance.

Concurrently, lines 967 to 1012 hold the final group of equations that form the mathematical model of this computer program. The equations are made up of force equilibrium equations that establish the mechanical stability of the system and other constraint equations that are necessary so that the Newton-Raphson algorithm is maintained accurate. Sequential solution of the equations form the foundation for the numerical method employed such that iterative computation is focussed towards exact solutions without compromising fundamental physical principles.

Besides, this segment of the MATLAB program includes important functions dedicated to checking and optimizing the computational accuracy. By virtue of the internal verification, error-handling requirements, and adaptive step-size control, the program is ensured to produce computed results in accordance with theoretical expectation and empirical requirement. All these efforts are provided for enabling the computational model to be robust enough, and the results can be utilized unconditionally in engineering practice and scientific investigation.

Through meticulous placement of visualization commands, terminal governing equations, and error-reduction mechanisms, this code block forms the methodological backbone of this work. Through the use of graphical output combined with high-level numerical solvers, the approach shows a judicious balance towards computational modeling such that results are not only analytically accurate but also visually understandable. Such a capability permits researchers and engineers to validate system behavior, optimize design parameters, and calibrate predictive models with accuracy and efficiency.

Figure 5.1 are selected screenshot of the main data page on the Microsoft Excel document that is created using the developed software, which is part of the integral analytical framework of this study. The Excel file is employed to structure the results in tabular format and to enable comparison with external datasets. The data are presented in a systematic way across different columns and rows to provide extensive numerical analysis while enabling effective data recovery for additional assessment. The formatted design enables primary variables influencing system behavior to be

analyzed while promoting uniformity in computational analysis. Each column of the dataset depicts a different studied parameter, such as important variables like applied load, Kit, Kot, α_i, and α_o, among many others, from label "A" to "AV." These variables are all important in the determination of operational conditions and performance indicators of the studied system. Rows are assigned sequential labels, and they represent measured values of rotational speed in revolutions per minute (RPM), thus allowing trend analysis as well as comparison studies under varied operational conditions. The numerical inputs supply decimal values and integers, reflecting the variety of calculated measures in relationship to the purposes of the study. Through this organization of the dataset, the program facilitates effective cross-referencing of performance indicators and the capability of determining the relationship between system variables accurately. Proper organization this way enhances interpretability because researchers can examine dependencies in an organized manner and contrast predictive theory with empirical observation. Additionally, the organized structure facilitates maximum reproducibility of results to make analytical output invariant within cyclic computational procedures. In addition to data storage and organization, the resulting Excel file also accommodates post-processing modes, making it possible to extract meaningful information from raw numerical results. The integration of different system parameters into a single dataset enhances the robustness of the analytical framework, enabling a more comprehensive analysis of force interaction, thermal behavior, and mechanical stability. Additionally, the numerical setup enables graphical plotting and statistical analysis, further enhancing the robustness of the methodological approaches employed in the study. Through gathering and structuring these data items, the software makes performance measures readily understandable and facilitates thorough system analysis of the one under investigation. This systematic process enhances reproducibility in such a way that scientific precision is ensured in valid and reliable computation results. The addition of this dataset into a more extensive mathematical model enhances the study's capability to deliver insightful engineering conclusions, and optimization of mechanical system design and numerical simulation is promoted.

A	B	C	D	E	F	G	H	I	J	K
RPM	Applied loac	Kit	Kot	alpha_i	alpha_o	gamma_i	gamma_o	X1	X2	delta_i
6000	0	2904899.4	2875191.5	58.635171	0.004384545	0.092378398	0.18157913	-0.999999143	0.52999183	7.27998E-
6000	2500	2906412.9	2873989	55.639457	15.02453353	0.10017231	0.18157913	0.499999432	0.5002008	0.0016500
6000	5000	2908247.6	2872563.2	51.761393	25.53836141	0.10985219	0.18157913	0.179999883	0.46800157	0.0027739
6000	7500	2909396	2871687.9	49.284289	30.36512239	0.115774596	0.18157913	0.19999821	0.44801061	0.0024017
6000	10000	2909971.2	2871254.3	48.024966	33.06692736	0.118703183	0.18157913	0.010002854	0.43594033	0.005059
6000	12500	2910461.5	2870887.4	46.942714	35.00642624	0.121174221	0.18157913	0.099996333	0.42680123	0.0054452
6000	15000	2910844.5	2870602.3	46.044408	36.34531148	0.123192471	0.18157913	-0.009994573	0.42019873	0.0062181
6000	17500	2911147.4	2870377.8	45.315923	37.33357084	0.124806964	0.18157913	0.099994886	0.41530138	0.0067422
6000	20000	2911300	2870265.1	45.010744	38.17040359	0.125477332	0.18157913	0.00999817	0.41107902	0.0075358
6000	22500	2911501.3	2870116.7	44.502599	38.79266821	0.126585633	0.18157913	0.009998688	0.40799865	0.0081218
6000	25000	2911605.2	2870040.2	44.289517	39.34586848	0.127047424	0.18157913	0.00999949	0.40519814	0.0086484
6000	27500	2911695.7	2869973.7	44.040684	39.63047866	0.127584468	0.18157913	0.010000663	0.40398737	0.0091952
6000	30000	2911766.3	2869921.9	43.888772	40.0228977	0.12791115	0.18157913	0.010002038	0.4020965	0.0097110
6000	32500	2911804.8	2869893.6	43.792052	40.23891793	0.128118675	0.18157913	0.010003687	0.40119548	0.0101989
6000	35000	2911818.6	2869883.5	43.757233	40.39598269	0.128193294	0.18157913	0.010005382	0.40065421	0.0106809
6000	37500	2911831.4	2869874.2	43.750043	40.62300875	0.128208698	0.18157913	0.010007321	0.39966273	0.0110950
6000	40000	2911797.2	2869899.2	43.926172	40.97924342	0.127830806	0.18157913	0.001010702	0.39792055	0.0116058
6000	42500	2911723.6	2869953.2	44.155619	41.06353863	0.127336708	0.18157913	-0.009988266	0.39778803	0.0119666
6000	45000	2911673.4	2869990.1	44.340864	41.1996108	0.126936306	0.18157913	0.000896489	0.39729967	0.0123869
6000	47500	2911516.6	2870105.4	44.910733	41.53506772	0.125696247	0.18157913	0.009889089	0.3955984	0.0128172
10000	0	2903646.1	2876205.9	59.262299	0.03800284	0.090714123	0.20459369	0.199999137	0.59999579	0.0005356
10000	2500	2905013	2875100.5	58.778434	5.493452504	0.091999176	0.20459369	0.010001093	0.51796993	0.0015051
10000	5000	2905352.7	2874828.8	58.071906	10.54339081	0.093863764	0.20459369	0.010003076	0.51182983	0.0026803
10000	7500	2905885.9	2874405	56.947351	15.10162701	0.096802014	0.20459369	0.01000598	0.50281987	0.0037238
10000	10000	2906518.9	2873905.7	55.603292	19.17624427	0.100264771	0.20459369	0.010008648	0.49229971	0.0044642
10000	12500	2907256.4	2873329.2	53.995522	22.90550544	0.104334305	0.20459369	0.010012263	0.48069938	0.0051463
10000	15000	2907941.6	2872798.6	52.477872	25.89579154	0.108100414	0.20459369	0.010017975	0.46989961	0.0059397
10000	17500	2908616.5	2872280.5	50.965097	28.58629361	0.111778952	0.20459369	0.010024384	0.45920005	0.0066506

L	M	N	O	P	Q	R	S	T	U	V
delta_o	FC	Msi	Mso	P1	M1	Mv	Mtotal	Hfi	Hfo	H1v
0.002614917	374.679431	0.201064418	-0.037575066	0	0	278.170062	278.170062	-1.17784611	-5.58270367	292.7904
0.002905445	291.086978	20.87766748	11.61845728	2681.44558	0.768334241	278.170062	278.938396	25.04212391	13.93598432	293.5991
0.003678055	244.466465	42.63079937	27.97087658	5362.89117	3.073336964	278.170062	281.243399	87.61305818	57.48459032	296.0253
0.004239013	229.004553	32.84458136	41.00685463	8044.33675	6.915008168	278.170062	285.08507	55.22759234	68.95231288	300.0689
0.005194207	222.753277	98.06990901	60.4662116	10725.7823	12.29334785	278.170062	290.46341	280.2604277	172.7980223	305.7299
0.006069021	218.690804	107.224855	80.73010812	13407.2279	19.20835602	278.170062	297.378418	217.2749001	163.5873155	313.0083
0.006687995	216.110102	128.5295809	96.85283109	16088.6735	27.66003267	278.170062	305.830095	361.2560529	272.2227151	321.9042
0.007313967	214.356983	142.9863876	113.6745348	18770.1191	37.64837781	278.170062	315.81844	268.6675269	213.591354	332.4176
0.007884067	213.40292	167.9179197	130.014766	21451.5647	49.17339142	278.170062	327.343454	422.2778163	326.9594548	344.5483
0.008465684	212.455262	185.9000082	146.9359313	24133.0103	62.23507352	278.170062	340.405136	458.1191609	362.0987765	358.2965
0.008963401	211.927772	203.3723334	162.3163116	26814.4558	76.83342409	278.170062	355.003486	496.7985248	396.5067559	373.6621
0.009540356	211.554483	221.7865426	179.4798341	29495.9014	92.96844315	278.170062	371.138505	536.5186545	434.1754825	390.6452
0.010075817	211.235307	239.9395225	196.6886479	32177.347	110.6401307	278.170062	388.810193	576.8718619	472.8864395	409.2457
0.010567006	211.069639	257.7144861	212.3615839	34858.7926	129.8484867	278.170062	408.018549	617.2225605	508.6029993	429.4636
0.011080306	210.996141	275.9947083	228.9023151	37540.2382	150.5935112	278.170062	428.763573	660.0517489	547.4285153	451.2990
0.011557983	210.91536	292.1666177	245.2242664	40221.6838	172.8752042	278.170062	451.045266	698.4088621	586.1956518	474.7518
0.012083951	210.955936	313.7877733	264.4774727	42903.1293	196.6935657	278.170062	474.863628	779.3595531	656.8867957	499.8220
0.012583227	211.159104	330.1604734	281.6752288	45584.5749	222.0485956	278.170062	500.218658	860.1736625	733.8540885	526.5097
0.013029558	211.284959	349.09919	297.8210126	48266.0205	248.9402941	278.170062	527.110356	881.0488836	751.6341433	554.8148
0.013486249	211.692698	371.9467013	316.3134056	50947.4661	277.368661	278.170062	555.538723	928.7853548	789.8638639	584.7373
0.005248223	785.600482	4.063449978	-2.858182495	0	0	391.029528	391.029528	21.65121436	80.562942	685.9695
0.005359863	993.946471	19.11183309	10.69069326	2681.44558	0.768334241	391.029528	391.797863	171.3125221	95.82804628	687.317
0.005619651	900.649173	44.92957226	22.00441159	5362.89117	3.073336964	391.029528	394.102865	372.9379508	182.6476361	691.3609
0.005805772	824.961942	72.29851984	33.04107935	8044.33675	6.915008168	391.029528	397.944536	550.0230792	251.3655361	698.1003
0.006220882	765.543835	92.88250906	46.4437683	10725.7823	12.29334785	391.029528	403.322876	647.0161386	323.5255801	707.5353
0.006848149	717.296779	111.9529861	63.9290579	13407.2279	19.20835602	391.029528	410.237884	711.1201344	406.0743874	719.6661
0.007348723	683.365479	135.266525	80.17451183	16088.6735	27.66003267	391.029528	418.689561	793.379639	470.2480919	734.4925
0.007948838	656.69772	156.0416014	99.36064874	18770.1191	37.64837781	391.029528	428.677906	849.5487547	540.9564798	752.0147
0.008277497	636.484517	170.7795434	115.355546	21451.5647	49.17339142	391.029528	440.20292	880.6174888	594.8259913	772.2327
0.008841999	625.10211	190.6423186	133.8024087	24133.0103	62.23507352	391.029528	453.264602	944.8299689	663.1293962	795.146
0.009371782	616.329722	211.4754323	152.8678392	26814.4558	76.83342409	391.029528	467.862952	1018.489313	736.2285955	820.755
0.009892591	610.943661	228.7358384	170.2069313	29495.9014	92.96844315	391.029528	483.997971	1076.272516	800.8759948	849.0608
0.010330571	606.200269	243.396799	186.0638443	32177.347	110.6401307	391.029528	501.669659	1119.981674	856.166131	880.0616
0.010843886	603.675642	264.6918305	203.1209936	34858.7926	129.8484867	391.029528	520.878015	1203.505386	923.5540412	913.7582
0.011400756	600.883624	284.4789125	223.0017388	37540.2382	150.5935112	391.029528	541.62304	1277.067043	1001.087106	950.1505
0.011856355	599.127974	300.6741068	239.3047601	40221.6838	172.8752042	391.029528	563.904732	1337.843946	1064.782159	989.2385
0.012325117	598.563344	320.0627994	255.1433792	42903.1293	196.6935657	391.029528	587.723094	1421.373342	1133.07138	1031.022
0.012768927	598.224486	337.6362568	269.9951806	45584.5749	222.0485956	391.029528	613.078124	1496.953529	1197.058166	1075.50

W	X	Y	Z	AA	AB	AC	AD	AE	AF	AG
Hi_total	Hci	Hco	Hvi	Hvo	Qi	Qo	Skd_theo	ki	ko	Mg
291.612613	211.392034	189.9322856	80.2205792	69.14646609	1.78967582	384.460665	-0.659751837	7.98042473	7.10001223	-1886.214
318.6413	230.985319	202.4727017	87.655981	73.71191138	194.814052	450.094844	0.385669454	8.02719397	7.06586037	-689.414
383.638386	278.102164	229.9589316	105.536222	83.71850747	424.899986	640.762211	0.323196401	8.08414174	7.025512	-338.3647
355.296507	257.556936	236.8010572	97.7395706	86.20944156	342.456064	792.564041	0.393043302	8.11992884	7.00082351	-426.7853
585.990363	424.788535	309.4344136	161.201828	112.6522335	1047.26797	1074.85676	0.415844817	8.13789674	6.98861614	-27.23612
530.283291	384.406086	301.0034371	145.877204	109.5828647	1169.45501	1357.35719	0.361929735	8.15323043	6.97829602	-235.6749
683.160334	495.22773	382.1918541	187.932604	139.1401994	1427.2834	1570.06252	0.431947976	8.16522308	6.97028636	29.236094
601.085132	435.730839	341.8876292	165.354293	124.4671031	1611.66738	1795.43018	0.349422735	8.17471799	6.96398299	-235.7934
766.826181	555.877691	429.3216892	210.94849	156.2982172	1904.51589	2009.31259	0.395286514	8.17950267	6.96081926	-27.97174
816.415719	591.825496	460.4906329	224.590223	167.6455366	2131.06756	2235.59251	0.391437394	8.18581971	6.95665523	-28.02243
870.460711	631.003091	492.9894395	239.457621	179.4770039	2341.74179	2435.55092	0.388591592	8.18908164	6.95451078	-28.1479
927.163904	672.107634	528.431541	255.05627	192.3800028	2567.40373	2674.39039	0.386750947	8.19192262	6.95264625	-28.16544
986.117609	714.843589	566.1566096	271.27402	206.1141353	2786.48072	2902.62217	0.384698515	8.19413967	6.95119325	-28.25754
1046.68624	758.750215	603.2301343	287.936024	219.6110677	2999.11931	3117.40852	0.383487279	8.19534936	6.95040121	-28.29946
1111.35079	805.626005	643.5953961	305.724789	234.306385	3214.25673	3347.27895	0.382745158	8.195782	6.95011806	-28.34036
1173.16071	850.432447	685.3883579	322.728261	249.5214687	3403.00598	3566.03782	0.381730458	8.19618321	6.94985555	-28.41698
1279.18163	927.287762	751.3930668	351.893873	273.5510451	3640.61038	3812.23855	0.389074043	8.1951108	6.95055736	-2.945627
1386.68341	1005.21656	823.4060077	381.466856	299.7679695	3811.62806	4051.0058	0.400151857	8.19279846	6.95207203	29.922206
1435.86374	1040.86772	853.6337939	394.996018	310.7726525	4014.12675	4268.49659	0.390079027	8.19122084	6.95310655	-2.6304C
1513.52275	1097.16328	899.9787281	416.359466	327.6449205	4224.84671	4495.05074	0.388724529	8.18629919	6.95633977	-29.13481
707.620762	474.940064	480.1705593	232.680698	225.6789738	35.9418853	1093.10506	0.424415215	7.941836	7.1289089	-1063.44
858.629932	576.294219	490.4745338	282.335712	230.5218163	169.632626	1128.19355	0.493332789	7.98392724	7.09742198	-86.96071
1064.29895	714.334905	550.2063257	349.964042	258.5956106	403.162694	1211.08889	0.486866558	7.99441302	7.08969922	-83.27378
1248.12339	837.713974	600.0189985	410.409412	282.0074434	660.341651	1271.56326	0.477632255	8.01088667	7.07766213	-80.40058
1354.55148	909.146256	652.1828833	445.405224	306.5243401	866.952842	1410.10191	0.466744511	8.03047638	7.06349841	-78.28699
1430.78624	960.313409	711.547794	470.472826	334.4257011	1073.32964	1628.34042	0.45422411	8.05334207	7.04716904	-76.65642
1527.87222	1025.47547	761.2438286	502.396756	357.7827143	1331.19563	1809.76822	0.442517441	8.07462467	7.03216307	-75.67886
1601.56355	1074.93552	816.4192341	526.628024	383.7150183	1577.55329	2035.55264	0.430844207	8.09562725	7.01753345	-75.083C
1652.85021	1109.35805	864.1373073	543.492167	406.1423945	1761.21854	2162.77999	0.419528461	8.11269488	7.00577349	-75.31064
1739.97635	1167.83526	921.6460272	572.141086	433.1713505	1997.94445	2387.50497	0.411812349	8.12501774	6.9973535	-75.45864
1839.24507	1234.46233	984.5328795	604.782746	462.7280153	2241.99196	2605.05181	0.404623213	8.13475988	6.99073838	-75.97101
1925.33338	1292.24298	1043.581647	633.090405	490.4807899	2449.94724	2825.01634	0.399754353	8.14223608	6.98568655	-76.19211
2000.04337	1342.38674	1098.756288	657.656631	516.4127343	2633.5065	3014.50502	0.39505477	8.14952329	6.98078289	-76.43166
2117.26363	1421.06249	1163.40864	696.201138	546.7991798	2879.54289	3241.84947	0.391820996	8.15342364	6.97816655	-76.64986
2227.21757	1494.86125	1236.44396	732.356321	581.1255993	3112.82527	3494.6198	0.388653506	8.15786951	6.97519127	-77.06878
2327.08247	1561.88845	1302.713274	765.194018	612.2720128	3303.68832	3706.08513	0.386296252	8.16089154	6.97317309	-77.31845
2452.39559	1645.99597	1373.849391	806.399627	645.7058115	3519.46715	3928.01116	0.385241619	8.16157445	6.9727175	-77.53310
2572.45523	1726.57745	1444.09281	845.877779	678.7200444	3715.45817	4142.05773	0.384562815	8.1620089	6.97242776	-77.65859

Figure 5. 1: Selected screenshots of the main data page in the Excel file generated by MATLAB code

Figure 5.2 is a screen capture of the analysis pages created to compare methodically and evaluate the outcomes of the ball-raceway contact angle and contact normal loads at the ball-raceway interface—both of the leading parameters that govern the mechanical behavior of the system under investigation. These are the dominant factors for the efficiency, life span, and overall performance of the ball-bearing machine and influence critical factors including frictional interactions, load distribution, and dynamic stability for different operating conditions.

This organized dataset in the figure provides a complete picture of the range of contact angles and normal loads such that they can be thoroughly analyzed for the impact they exert on behavior of rolling elements. By analyzing these controlling variables' effect, researchers can formulate astute conclusions concerning bearing design configuration optimization, wear pattern prediction, and enhancement of ball-raceway interface reliability under practical operational conditions. The ability to test and quantify these

interactions is the turning point in the development of engineering models and tribological performance, maximizing the efficiency of bearing systems.

Plotted alongside are reference data in the form of black numbers that are existing results from past experiments or simulations. Reference datasets constitute a comparative standard required by which newly derived results are tested against known results. Comparative analysis is necessary to ascertain the validity and reliability of computational resources adapted by this study. Through comparison with existing experimental and numerical results with the newly derived observations, scientists can systematically identify trends, discover inconsistencies, and optimize analytic procedures for improving computational accuracy.

Additionally, comparative analysis facilitates the establishment of the dialogue between theoretical prediction and experimental observation and brings the gap between simulation-based analysis and actual engineering application closer. Systematic analysis not only enhances the interpretability of the observed results but brings about a better understanding of the governing physical laws that govern the operation of the system. With thorough comparison and calibration, the research enhances the level of confidence in the mathematical model developed and its applicability in tribological performance analysis. Hence, a more systematic approach is considered in this research.

More detailed discussion of the general findings and interpretation of the implications of their variations is given in chapter Results and Discussion. The results from this study are discussed in detail in this chapter, the broader general practical implications of the results discussed, and the research contribution to ball-bearing system optimisation. By including ordered analysis of data within a comparative verification and theoretical analyses framework, the research contributes to methodological rigour behind engineering reliability and predictive confidence.

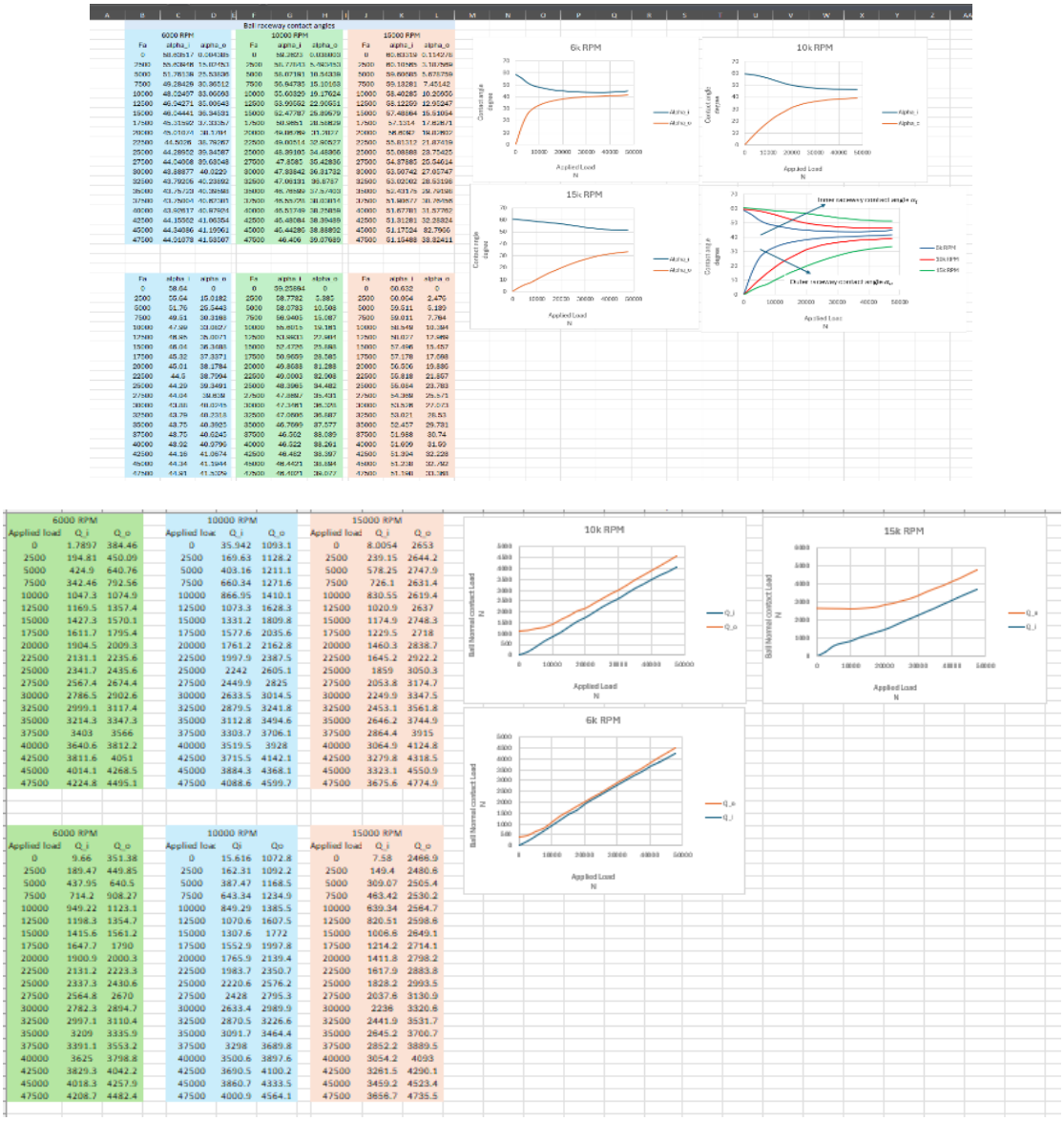

Figure 5. 2: A screenshot of the data page from the Excel file displaying the results for contact angles and normal loads

Figure 5.3 illustrates a group of screenshots depicting the results achieved for the basic dynamic capacity and one of the most important parameters in determining the operating life for this type of bearing. The parameter is very important in determining the performance and lifespan of the bearings under various working circumstances.

The basic dynamic capability is also determined significantly by the mechanical nature of the material utilized in the manufacture of bearings. The material strengths, fatigue life, and structural stability also directly impact the capability of the bearing to withstand continuous loads and maintain optimal performance for a prolonged period. Other such major parameters—e.g., contact angles, external loads, and rotational

speeds—are also critical with regard to the dynamic capability and performance of the bearing system.

The screenshots provide an accurate visualization regarding the three rotational speeds' fundamental dynamic capacity behaviors under investigation of the impact of different applied loads ranging from 0 to 47,500 Newtons. By exploring the capacity under different changing conditions in the test runs, this study provides thoughtful insights into the performance of the bearing under different operating stresses to help in bearing design and performance prediction.

There is a need to comprehend how material properties, contact mechanics, and load distribution are related to improve reliability for high-performance applications such as aerospace, automotive engineering, and industrial machinery. The conclusions of the research aid in the development of predictive models for wear resistance, fatigue failure prevention, and improved operation efficiency under harsh conditions.

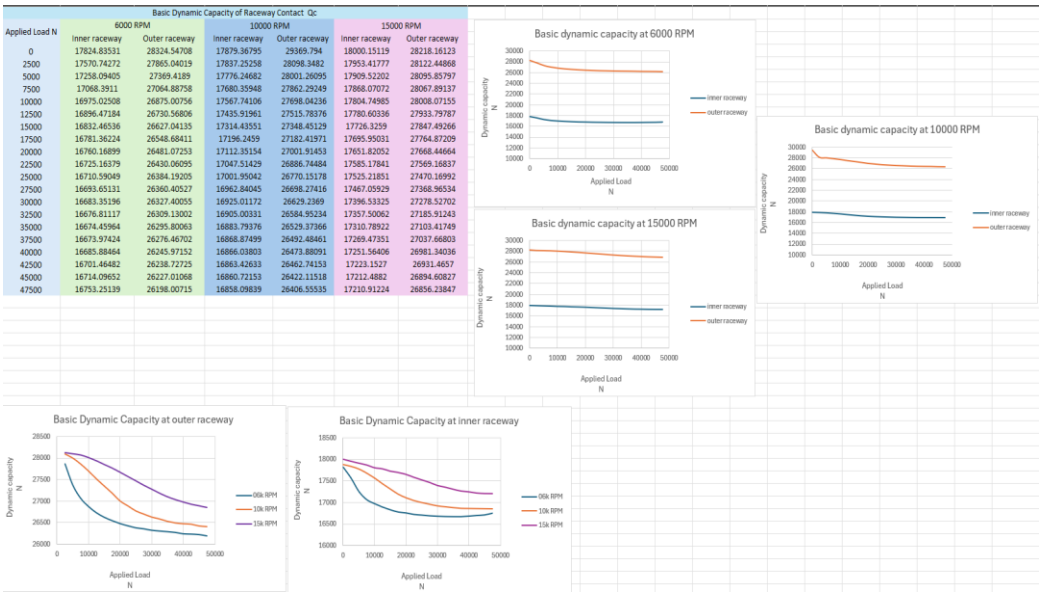

Figure 5. 3*:* A screenshot of basic dynamic capacity analysis of angular contact bearings under varying loads and rotational speeds

Figure 5.4 is a set of screenshots documenting the results obtained for a set of important variables that influence the performance of the angular contact ball bearings. These variables are of interest to comprehend the mechanical behavior and working reliability of the bearing system under various loading and rotational speed conditions.

The chief variables taken into consideration in the current study are centrifugal forces, the overall resultant force on the entire bearing, and the frictional torque produced as a result of the loading. These are critical parameters that greatly influence the calculation of the efficiency and life ofangular contact bearings, particularly in the case of high-speed and high-load applications where precise distribution of the loads and minimal losses in terms of energy are required.

Centrifugal Forces: These are forces generated as a result of the high speeds of rotation of bearing elements, and they influence contact pressure as well as load transmission on raceway surfaces. High centrifugal forces cause high wear, material fatigue, and reduced service life, and hence their assessment is necessary in the optimization of bearing design and ensuring the stability of operation.

Resultant Force Acting on the Bearing: This is the overall distribution of the forces over the bearing structure that includes the external applied forces and the internal reaction forces. The behavior of resultant forces addresses the prediction of bearing deformation, accumulation of stresses, and potential failure mechanisms under dynamic loading.

Frictional Torque: Frictional Torque results from interaction of rolling bearings with raceways. Frictional torque is a significant component of efficiency in terms of energy and heat. Higher frictional resistance may result in higher energy losses, excessive heat generation and early degradation of the material, necessitating analysis at due time for optimizing the performance and life of the bearings.

The plots presented in Figure 10 are a close-up illustration of how these variables evolve at three rotational speeds and over the large range of applied loads between 0 and 47,500 Newtons. When comparing these results in a direct manner, the behavior in the bearing can be further analyzed to yield improved predictions regarding wear mechanisms, operating efficiency, and structural integrity over the long-term.

Moreover, the findings highlight the interconnectedness of these parameters in reflecting the dynamics that control the forces felt by the bearing system under various speeds and loads. By utilizing this combined analysis, the engineering models are more precise, with predictive precision enhanced and bearing designs optimized for commercial use.

A comprehensive discussion of these results, including their implications for bearing design and modeling of the long-term performance is provided in the chapter "Results and Discussion". This chapter includes theoretical relationships, experimental correlations and the implications of these results for the advancement in the area of knowledge in the mechanics of angular contact bearings.

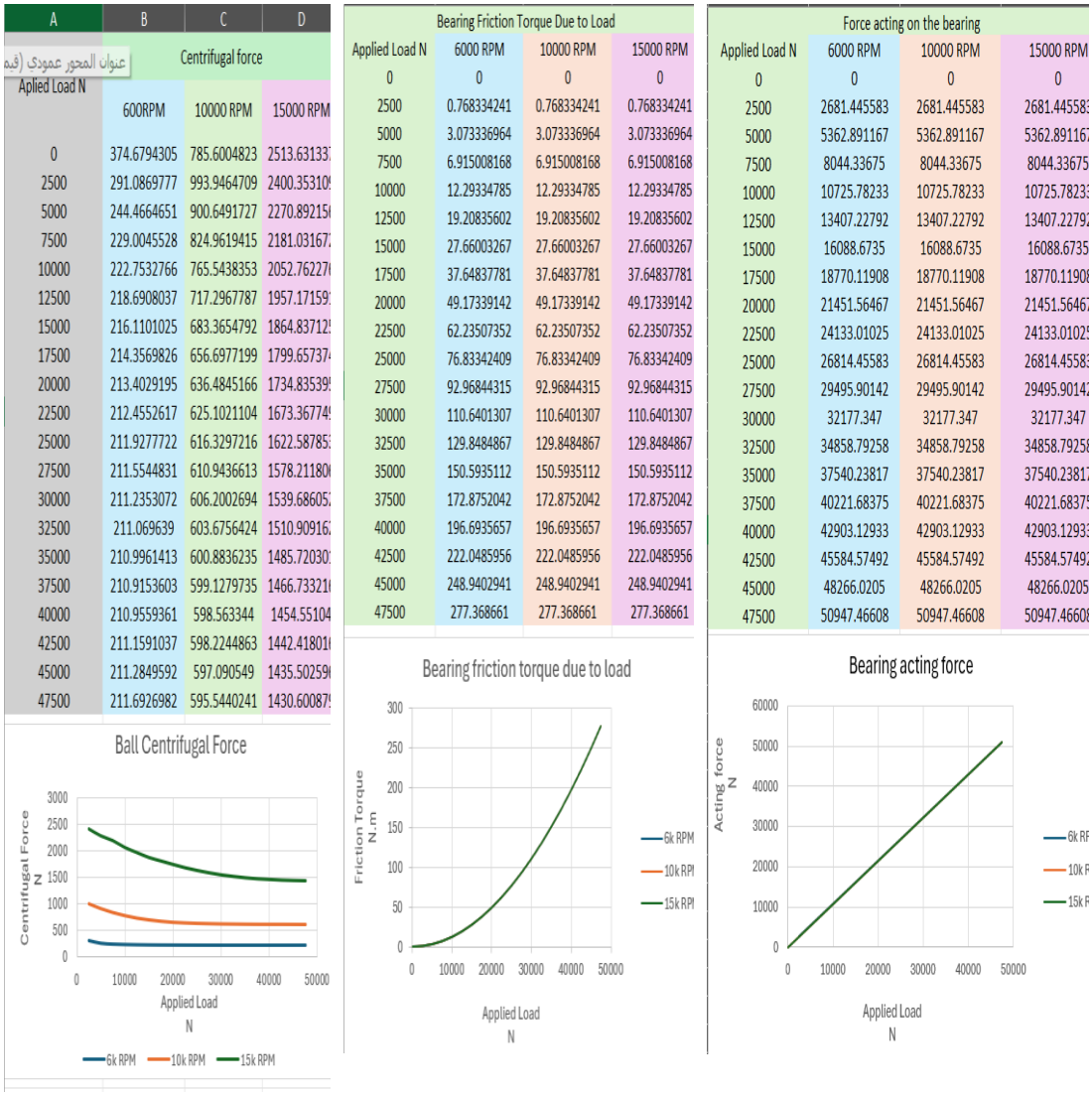

Figure 5. 4: Screenshots of centrifugal forces, resultant bearing loads and frictional torque under varying speeds and applied loads

The following screenshots in Figure 5.5 show a clear visual representation of frictional torque in angular contact ball bearings. They highlight three key components: friction torque from spinning, viscous friction torque, and total friction torque on the bearing. These factors are essential for bearing performance. They influence both thermal behavior and mechanical integrity.

Friction from spinning significantly raises heat levels. If the heat is too high, it can speed up material degradation and lower bearing efficiency. Its effects go beyond just heat; it also plays an important role in wear mechanisms. It can cause micro-fractures beneath the surface layer of the bearing material. These subsurface fractures can develop into larger cracks, which can weaken the bearing's structure and shorten its lifespan. Additionally, ongoing exposure to friction-related wear can lead to surface fatigue. This results in material delamination and reduces load-bearing capacity.

Viscous friction torque is equally important in this context. It occurs due to interactions between the bearing components and the lubricating oil. The lubrication system is crucial for reducing friction forces. It lowers direct contact between surfaces and allows for smoother motion. Efficient heat dissipation helps maintain optimal operating temperatures. This prevents thermal raceway conditions where too much heat can soften materials and lead to early failure. Furthermore, lubrication forms a protective film over contact surfaces to reduce abrasive wear, extending the bearing's service life.

The drag force from the lubricant system is considered a minor factor in the overall friction analysis of this study. Given its minimal impact, it has been left out of detailed calculations. However, the total frictional torques acting on the bearing system, as shown in the figure, highlight the combined effects of various frictional components. The trends in the curves provide insights into overall frictional behavior, helping to understand how mechanical resistance and lubrication efficiency interact.

A more detailed discussion of these results can be found in the "Results and Discussion" chapter. This section explores the comparative analysis of different frictional influences, providing a thorough evaluation of their effects on bearing performance and lifespan. This revision improves technical clarity, expands on wear mechanisms, and highlights the role of lubrication in reducing friction and preventing material damage.

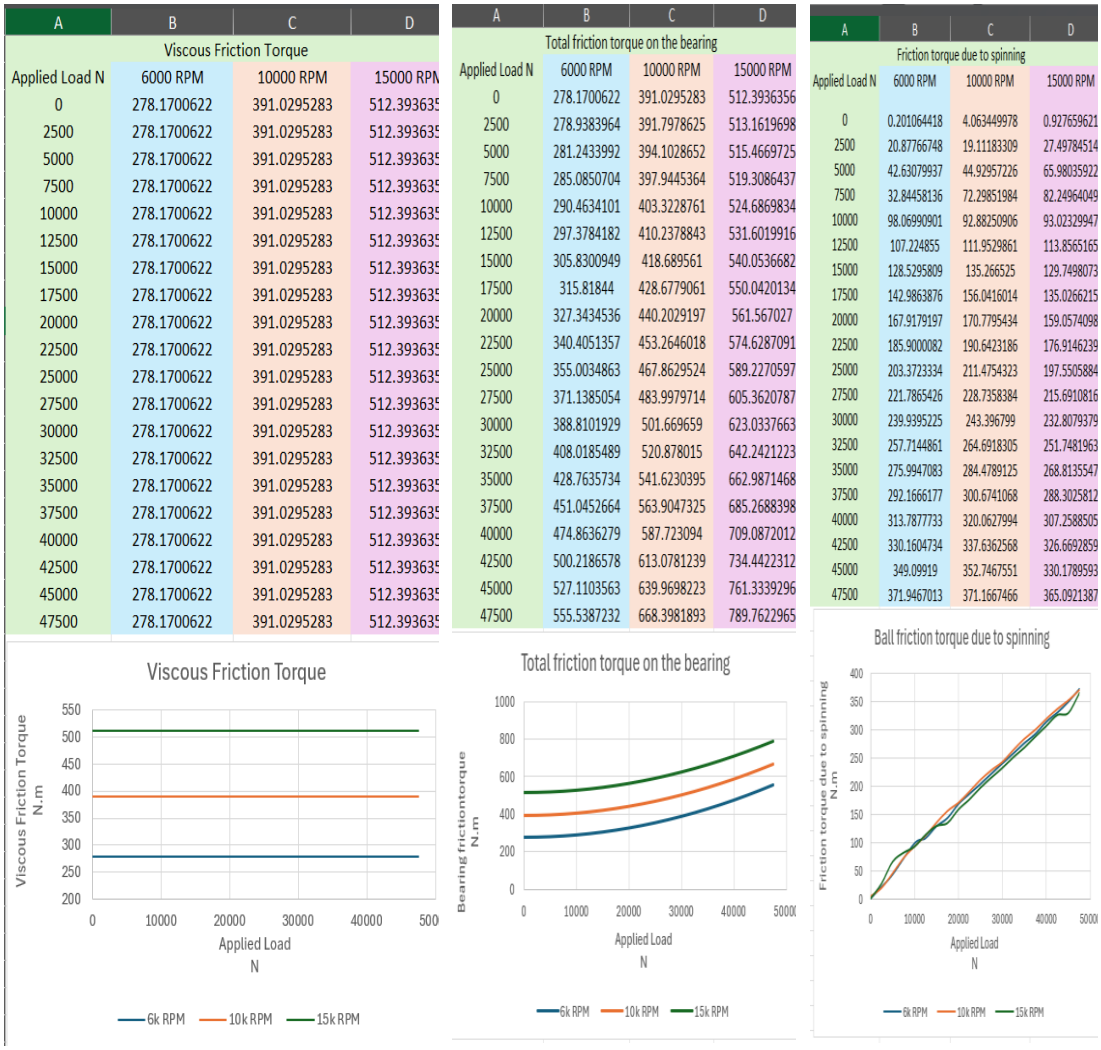

Figure 5. 5: Screenshots of friction torque due to spinning, viscous friction torque and total friction torque on the bearing

Figure 5.6 provides screen shots of the calculations for Bearing Frictional Power Loss, Spinning Friction Heat, and Viscous Friction Heat Generation Rate in the angular contact ball bearing under investigation here. These frictional and thermal effects lie at the heart of the process of rotational motion and applied load-induced heat generation, both of which are issues of paramount significance to the efficiency of operation and lifespan of ball-bearing systems.

The effect of these factors extends far beyond local heat generation with direct influence upon the bearing's thermomechanical behavior. Thermal expansion itself, caused by ongoing heat generation at the contact zone between the ball and raceway, generates structural distortion at the area of critical contact. These thermal effects are important in that they modify patterns of load distribution, influence tribological performance and

lead to material fatigue at an increased rate. Understanding these interactions is imperative in order to optimize bearing design and to design effective heat dissipation strategies.

By analyzing these thermal phenomena systematically, the research gains insight into how they influence the performance and life of the angular contact ball bearings. Computational modeling in this context allows the detailed quantification of the friction losses that can be useful to researchers by identifying areas that can be optimized for performance. Systematic consideration of the heat generation mechanisms is also useful for the design of predictive thermal management models for high-speed rotating machinery.

In addition, results provided constitute a reference against which experimental findings can be contrasted with numerical simulations to confirm the applied mathematical model. The integration with calculations for frictional power loss into the heat generation rate analysis will permit a complete investigation into the thermal behavior of the system to facilitate engineering choices in lubricant design, cooling systems, and material optimalization strategies.

A detailed explanation of these results and their implications on bearing performance, wear mechanisms, and stability operations is provided in the "Results and Discussion" chapter in this dissertation. The chapter also describes bearing behavior against thermal influence and offers insight into engineering developments that minimize heat-induced degradation and enhance mechanical reliability.

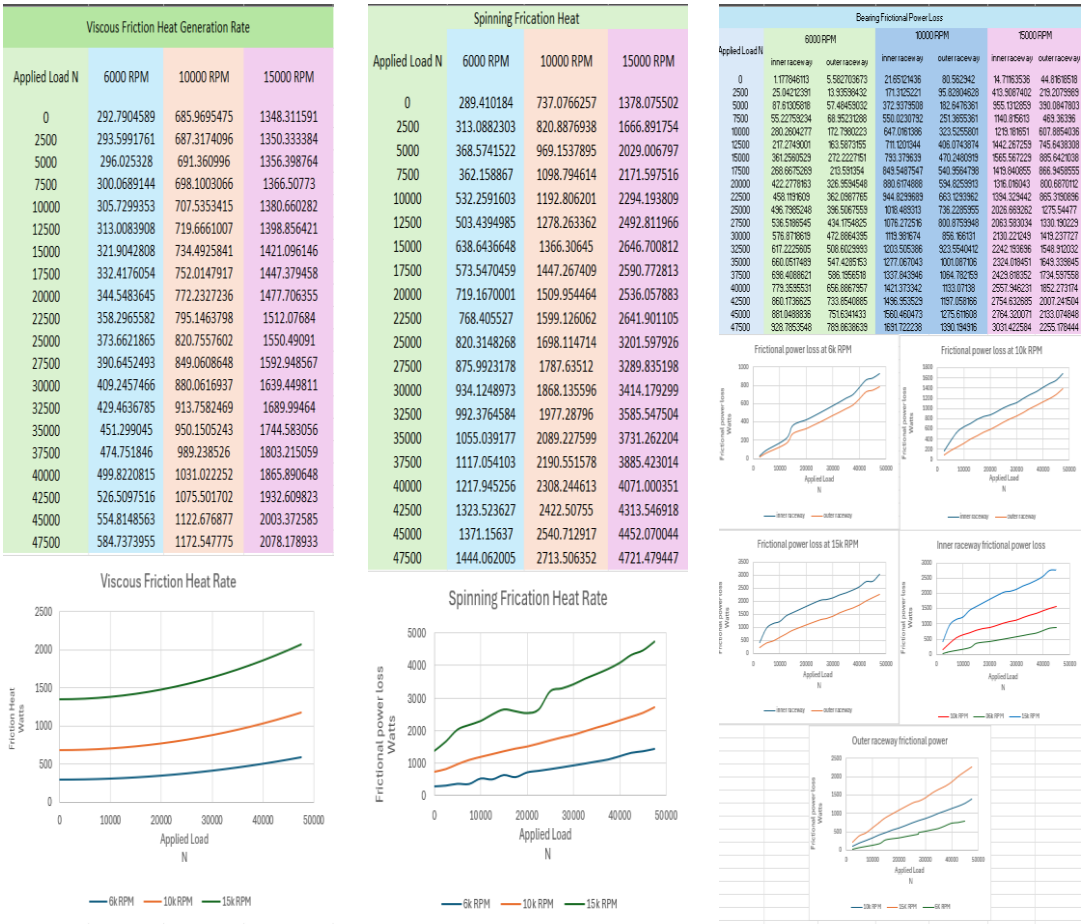

Viscous Friction Heat Generation Rate

Applied Load N	6000 RPM	10000 RPM	15000 RPM
0	292.7904589	685.9695475	1348.311591
2500	293.5991761	687.3174096	1350.333384
5000	296.025328	691.360996	1356.398764
7500	300.0689144	698.1003066	1366.50773
10000	305.7299353	707.5353415	1380.660282
12500	313.0083908	719.6661007	1398.856421
15000	321.9042808	734.4925841	1421.096146
17500	332.4176054	752.0147917	1447.379458
20000	344.5483645	772.2327236	1477.706355
22500	358.2965582	795.1463798	1512.07684
25000	373.6621865	820.7557602	1550.49091
27500	390.6452493	849.0608648	1592.948567
30000	409.2457466	880.0616937	1639.449811
32500	429.4636785	913.7582469	1689.99464
35000	451.299045	950.1505243	1744.583056
37500	474.751846	989.238526	1803.215059
40000	499.8220815	1031.022252	1865.890648
42500	526.5097516	1075.501702	1932.609823
45000	554.8148563	1122.676877	2003.372585
47500	584.7373955	1172.547775	2078.178933

Viscous Friction Heat Rate

Spinning Frication Heat

Applied Load N	6000 RPM	10000 RPM	15000 RPM
0	289.410184	737.0766257	1378.075502
2500	313.0882303	820.8876938	1666.891754
5000	368.5741522	969.1537895	2029.006797
7500	362.158867	1098.794614	2171.597516
10000	532.2591603	1192.806201	2294.193809
12500	503.4394985	1278.263362	2492.811966
15000	638.6436648	1366.30645	2646.700812
17500	573.5470459	1447.267409	2590.772813
20000	719.1670001	1509.954464	2536.057883
22500	768.405527	1599.126062	2641.901105
25000	820.3148268	1698.114714	3201.597926
27500	875.9923178	1787.63512	3289.835198
30000	934.1248973	1868.135596	3414.179299
32500	992.3764584	1977.28796	3585.547504
35000	1055.039177	2089.227599	3731.262204
37500	1117.054103	2190.551578	3885.423014
40000	1217.945256	2308.244613	4071.000351
42500	1323.523627	2422.50755	4313.546918
45000	1371.15637	2540.712917	4452.070044
47500	1444.062005	2713.506352	4721.479447

Spinning Frication Heat Rate

Bearing Frictional Power Loss

Applied Load N	6000 RPM		10000 RPM		15000 RPM	
	inner raceway	outer raceway	inner raceway	outer raceway	inner raceway	outer raceway
0	1.17784613	5.582703673	21.65121436	80.582942	14.71163536	44.81616518
2500	25.04212391	13.33539432	171.3125221	95.82804628	413.9087402	215.2073989
5000	87.81005918	57.48458032	372.9373588	182.6478381	955.1312859	390.0847803
7500	55.22759234	68.85231288	550.0230792	251.3855381	1140.815613	469.36396
10000	280.2604277	172.7990223	647.0761386	323.5255801	1219.181651	607.8854036
12500	217.2749001	163.5873155	711.1201344	406.0743874	1442.267259	745.6438308
15000	361.2560529	272.2227151	793.379639	470.2480919	1565.567229	885.6421038
17500	288.6675269	213.591354	845.5487547	540.9564798	1419.840855	866.9458555
20000	422.2776163	326.9594548	880.6174888	594.8253913	1316.076043	800.6870712
22500	458.1191609	362.0987765	944.8239889	663.1293962	1394.329442	865.3180896
25000	496.7365248	396.5067559	1018.489313	736.2285955	2026.693262	1275.54477
27500	536.5186545	434.1754825	1076.272516	800.8759348	2063.583034	1330.190229
30000	576.8718619	472.8864395	1113.381674	856.166131	2130.221243	1413.237727
32500	617.2225605	508.6023993	1203.505386	923.5540412	2242.193696	1548.312032
35000	660.0517489	547.4285153	1277.067043	1001.087106	2324.019451	1643.338845
37500	698.4088621	586.1956518	1337.843946	1064.782153	2428.816352	1734.597558
40000	773.3535531	656.8867957	1421.373942	1133.07108	2557.946231	1852.273174
42500	860.1738625	733.8549885	1496.953529	1197.052986	2754.632885	2007.247504
45000	881.0498838	751.6341433	1568.460473	1275.611688	2784.320071	2133.078498
47500	928.7853546	789.8638639	1691.722238	1380.194916	3031.422584	2255.178444

Figure 5. 6: Screen captures of the results for bearing frictional power loss, spinning friction heat, and viscous friction heat generation rate

Figure 5.7 presents the screen shots of the result associated with the Load Friction Heat Generation Rate and Total Friction Heat Generation Rate in the bearing system under analysis. These are the parameters that are crucial to include in analysis as they allow making the precise prediction about the operating performance of the bearing, its temperature behavior, and its efficiency in different conditions.

The topmost figure clearly shows the Load Friction Heat Generation Rate that is the most important parameter in determining the amount of the heat created by friction forces as a result of imposed loads. Being a critical factor in determining the local heat effects on the structure of the bearings and consequently its general endurance and working status is vital. With the capacity to quantify the rate, the researchers can assess the impact of different load settings and their contribution in the creation of friction-induced thermal buildup.

The second graph illustrates the Total Friction Heat Generation Rate, which is a measure of the total thermal impact of the various frictional contacts present in the bearing system. This parameter allows researchers to comprehend the total energy dissipation by friction for various operating conditions. All these analyses are important to develop predictive models that can simulate the thermal behavior of the bearing, which will open the door for the creation of advanced lubrication techniques and thermal management strategies.

Besides, the requirement to include these parameters in analytical modeling stems from the possibility that they can simulate real working conditions more realistically. By being included in numerical simulation, these parameters provide a greater degree of understanding of the thermal performance of the bearing in a way that the engineering analysis is brought closer to empirical reality. Utilizing such an approach, performance prediction is made more accurate and optimized bearings are developed to avoid excessive generation of heat with a focus towards improved operating life.

In addition to that, the third figure also introduces comparative results of existing research that are employed as a reference for validation of the numerical model created in the current research. Comparative analysis enables closer insight into the disparity between the results that have already been derived and the proposed analytical approach, allowing the predictive performance of the developed model to be validated successfully. The explanation of the results in detail and their effect upon the performance of the bearings and thermal efficiency is given under the chapter “Results and Discussion” in this dissertation, where the influence of such parameters upon the creation of analytical approaches is discussed in further detail as well.

The inclusion of such frictional heat generation rates in analytical analyses not only enhances thermal prediction accuracy but also helps in the formulation of bearing system designs that lead to improved performance and sustainability of mechanical systems.

Total Frication Heat Generation Rate			
Applied Load N	6000 RPM	10000 RPM	15000 RPM
0	582.2006429	1423.046173	2726.387093
2500	798.2192338	1699.736931	3208.756966
5000	1047.663135	2043.57844	3768.469216
7500	1236.823263	2371.490403	4112.700729
10000	1604.116405	2666.468852	4440.981401
12500	1774.107026	2955.588599	4849.327524
15000	2109.73891	3249.989998	5216.987923
17500	2246.687443	3540.004992	5378.875062
20000	2595.969984	3814.441806	5546.018857
22500	2850.488532	4118.058888	5877.764391
25000	3109.295287	4434.188748	6667.40711
27500	3373.487668	4743.546086	6989.633867
30000	3641.752573	5046.579218	7352.011038
32500	3911.753893	5380.959963	7765.4559
35000	4187.783805	5720.823706	8157.290844
37500	4464.78336	6052.767515	8561.615484
40000	4782.276576	6403.776103	9001.400237
42500	5106.074444	6754.050317	9502.197807
45000	5373.544119	7110.962687	9903.015522
47500	5667.904121	7525.158848	10438.7631

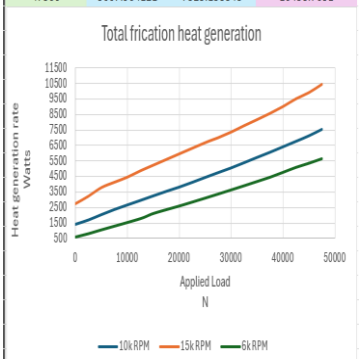

Load Friction Heat Generation Rate			
Applied Load N	6000 RPM	10000 RPM	15000 RPM
0	0	0	0
2500	191.5318274	191.5318274	191.5318274
5000	383.0636548	383.0636548	383.0636548
7500	574.5954821	574.5954821	574.5954821
10000	766.1273095	766.1273095	766.1273095
12500	957.6591369	957.6591369	957.6591369
15000	1149.190964	1149.190964	1149.190964
17500	1340.722792	1340.722792	1340.722792
20000	1532.254619	1532.254619	1532.254619
22500	1723.786446	1723.786446	1723.786446
25000	1915.318274	1915.318274	1915.318274
27500	2106.850101	2106.850101	2106.850101
30000	2298.381929	2298.381929	2298.381929
32500	2489.913756	2489.913756	2489.913756
35000	2681.445583	2681.445583	2681.445583
37500	2872.977411	2872.977411	2872.977411
40000	3064.509238	3064.509238	3064.509238
42500	3256.041065	3256.041065	3256.041065
45000	3447.572893	3447.572893	3447.572893
47500	3639.10472	3639.10472	3639.10472

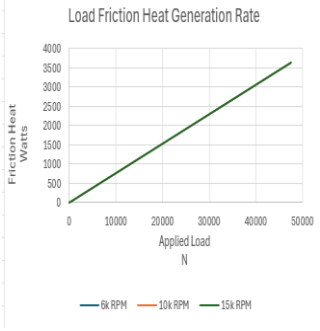

Figure 5. 7: screen captures depict the results related to load friction heat generation rate and total friction heat generation rate

Figure 5.8, screen shots of results obtained for Bearing Conducted Heat and Bearing Convected Heat for the bearing system under consideration. These thermal values must be incorporated into analytical studies in an attempt to attain a correct picture of the heat transfer behavior of the bearing, providing a clearer view of its efficiency under operating conditions.

The initial figure clearly illustrates Bearing Conducted Heat, a most important parameter representing the thermal energy transferred by solid contact inside the bearing assembly. This mode of the heat transfer is predominantly controlled by material properties, geometric configuration, and loading distribution between the bearing components. The understanding of the conductive heat transmission is important in the calculation of the temperature gradients, thermal expansion influence approximation, and structural integrity under various operating conditions. Through the quantification of the parameter, thermal models can be improved by the inclusion of material conductivity, and bearing design optimized for enhanced thermal performance.

The second graph shows Bearing Convected Heat, or the heat that is transferred through fluid interaction—primarily air or lubrication—around the bearing surfaces. This is heavily dependent upon fluid velocity, ambient conditions, and bearing geometry. The convective heat transfer process is the process by which the bearing system maintains correct thermal equilibrium to avoid excessive temperature rise that can lead to increased wear and degradation. Through analysis of the convection heat dissipation, researchers can optimize the cooling process, design a more effective lubricant flow mechanism, and have an overall improved thermal management system for the bearing.

The inclusion of thermal parameters in analytical analyses is paramount to simulating the actual operating conditions satisfactorily. Convected and conducted heat influence the thermal behavior of the bearing and modify its working life and efficiency. Through inclusion of these parameters in numerical calculations, the optimal thermal control systems can be designed, the losses can be minimized, and high-performance bearing systems can be made with improved efficiency.

With the integration of conducted and convected thermal parameters into analysis models, this study contributes to thermal modeling approaches in a manner that ensures bearing systems are made resistant to extreme thermal conditions while not jeopardizing their efficiency and reliability. These findings are discussed in the “Results and Discussion” chapter within this thesis.

Heat Transfer Modes						
Applied Load N	6000 RPM		10000 RPM		15000 RPM	
	Conducted Heat	Convection Heat	Conducted Heat	Convection Heat	Conducted Heat	Convection Heat
0	211.3920336	80.22057919	474.9400639	232.6806979	851.8777983	511.1454283
2500	230.985319	87.65598101	576.2942195	282.3357122	1102.63616	661.6059644
5000	278.1021638	105.5362223	714.3349052	349.9640416	1444.686408	866.8436416
7500	257.5569361	97.7395706	837.7139742	410.4094116	1567.055533	940.2678097
10000	424.7885347	161.2018283	909.1462563	445.4052238	1624.878857	974.9630764
12500	384.4060864	145.8772044	960.3134088	470.4728263	1775.677874	1065.445806
15000	495.2277298	187.9326039	1025.475467	502.396756	1866.638932	1120.024443
17500	435.7308391	165.3542932	1074.935522	526.6280243	1791.988045	1075.232267
20000	555.8776907	210.9484901	1109.358046	543.4921666	1746.052481	1047.669918
22500	591.8254957	224.5902234	1167.835263	572.141086	1816.478939	1089.927343
25000	631.0030906	239.4576207	1234.462327	604.7827456	2235.694354	1341.465818
27500	672.1076335	255.0562702	1292.242975	633.090405	2285.300814	1371.230786
30000	714.8435887	271.2740199	1342.386736	657.6566315	2356.012004	1413.659056
32500	758.7502148	287.9360242	1421.062495	696.2011381	2457.583904	1474.604432
35000	805.6260053	305.7247885	1494.861246	732.3563213	2542.840963	1525.760544
37500	850.4324468	322.7282613	1561.888454	765.1940175	2645.609489	1587.423922
40000	927.287762	351.8938727	1645.995967	806.3996271	2764.860017	1658.976863
42500	1005.216558	381.4668563	1726.577452	845.8777791	2929.48627	1757.756238
45000	1040.867722	394.9960181	1800.864945	882.2724047	2979.766921	1787.925735
47500	1097.163285	416.3594657	1922.437351	941.8326619	3193.45702	1916.144498

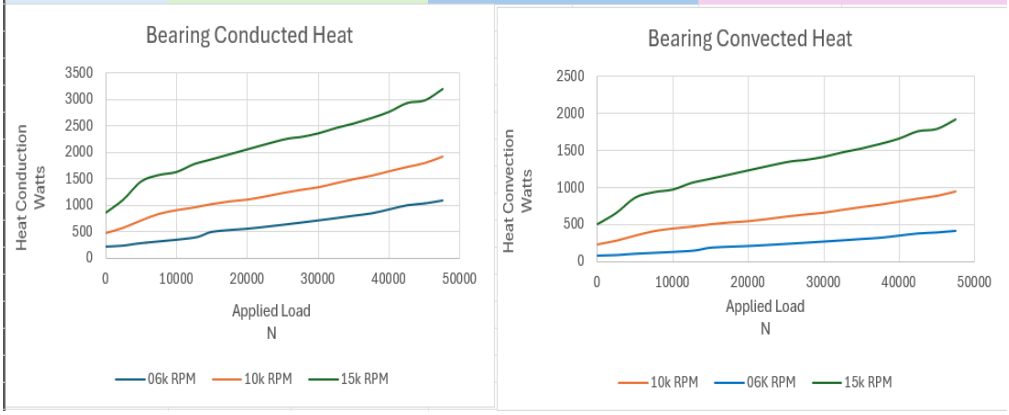

Figure 5. 8: Screen captures present the results of the bearing conducted heat and bearing convected heat

Figure 5.9 depicts a sequence of screenshots presenting the results obtained for the deformation analysis under the imposed load at various rotational speeds. The analysis is significant in investigating the angular contact bearing's mechanical behavior under severe loading and high-speed operation, where the structural reliability and stability of performance are the foremost issues in engineering applications.

The studied deformation behavior is critical to explaining the mechanical response of the bearing system under varying operating stresses. The parameters are utilized to establish the influence of imposed loads on the overall distribution of stresses, contact mechanics, and the potential wear mechanisms in the bearing. The findings are critical in the design optimization process, material selection during design, and performance improvement in high-speed applications within the aeronautics, automotive, and

industrial machinery industries. Moreover, the figures also show fatigue life results for the identical bearing, providing an overall assessment of its endurance upon being subjected to cyclic loading. Fatigue life calculations are a significant aspect of bearing reliability in relation to long-term reliability estimation since cyclic loading can result in material degradation, microstructural alteration, and failure upon repeated exposure.

By combining fatigue analysis and deformation studies, this study guarantees a more dependable estimation of the bearing's lifespan in addition to its capacity to endure long-term operational stresses. In progressing toward a comprehensive bearing performance evaluation through its inquiry into the coupled interaction among applied loads, rotational velocities, deformation responses, and fatigue behaviors, the study addresses a critical need in the engineering field. Comparisons with experimental observations and theoretical predictions offer a valuable benchmark for validating computational simulations and refining predictive subroutines for engineering design. Such investigations close the divide between simulation-based evaluation and real-world application, ensuring that such models effectively capture the response of bearings in the real environment. Furthermore, by systematic study of bearing deformation and fatigue life, maintenance procedures can be optimized, predictive diagnostics can be enhanced, and stronger bearing systems can be developed for demanding applications. Clarification of the interaction amongst these critical parameters is necessary to improve efficiency, avoid early failure, and maximize the service life for high-performance applications of angular contact bearings.

The full description of these results, including their implications and contrasts with theoretical modeling, is given in the Results and Discussion chapter. This chapter provides a more in-depth analysis of the trends identified, outlining why they are significant at a wider level within the context of bearing design optimization, maximum load-carrying capacity, and performance reliability. These results form part of the contribution towards engineering knowledge progression and the establishment of more efficient practical solutions to high-speed rotary systems. Figure 15 shows the angular contact ball bearing deformation and fatigue life at different applied loading and varying rotational speed.

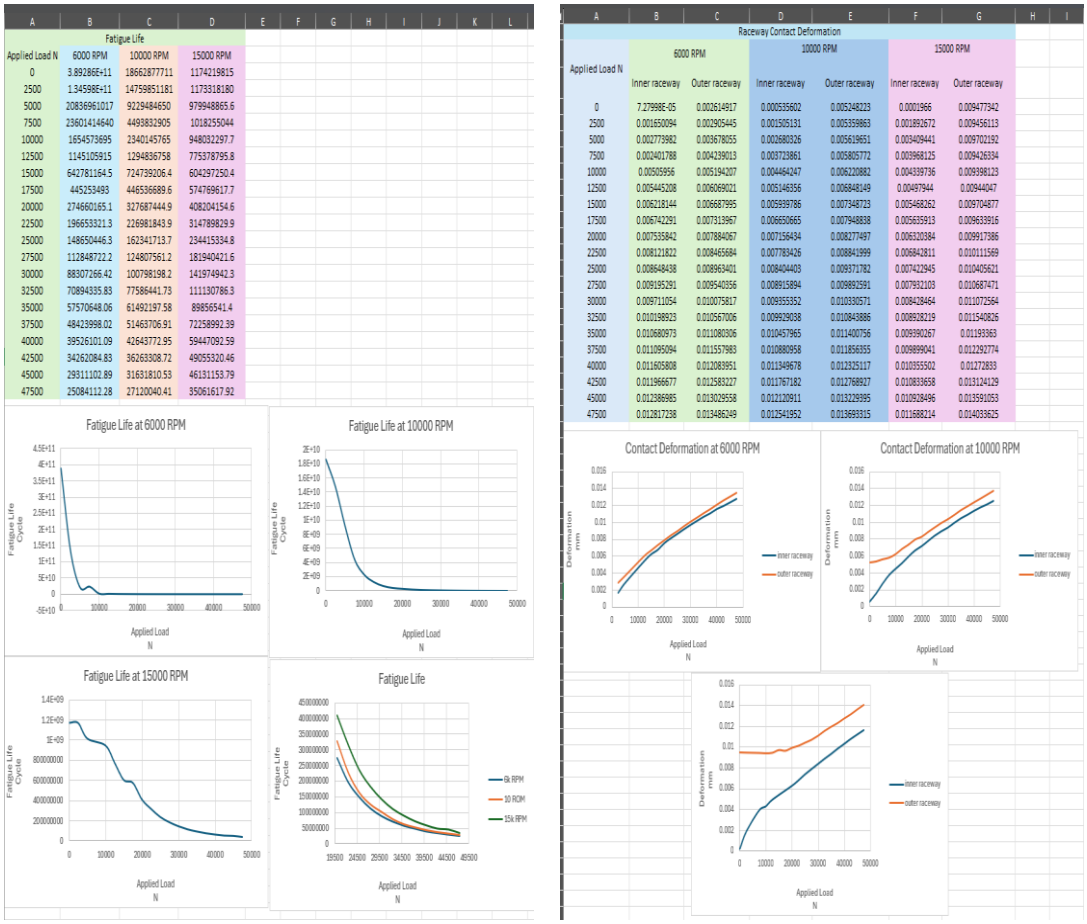

Figure 5. 9*:* Deformation and fatigue life analysis of angular contact ball bearings under applied load and varying rotational speeds screenshot

Chapter 6: Conclusions and Recommendations

This study provides a comprehensive investigation into the effects of applied load and rotational speed on key performance metrics of angular contact ball bearings (ACBBs), including inner and outer raceway contact loads and bearing fatigue life. The new mathematical and theoretical coupled model predicts greater contact loads compared to the widely employed Harris model. This is because the new model takes into account more variables, such as localized deformation, elastohydrodynamic lubrication (EHL), variable temperature, and the interaction of multiple particles. The contact loads on the inner and outer raceways increase in a very linear fashion with greater load. Significant differences between the new model and the Harris model only appear when higher speeds and loads are involved. These differences indicate that older analysis approaches have limitations in revealing the increased significance of changes in dynamic load, lubrication stress, and thermal expansion at high speeds and loads. The new model further reveals that increased speeds, particularly at 15000 RPM, facilitate improved lubrication and load distribution that minimizes direct metal-to-metal contact and postpones fatigue failure. This aids in enhancing the bearings' fatigue life despite increased dynamic forces. Fatigue life analysis indicates a strong negative relationship between applied loads and the duration bearings last. As loads rise, bearings fail more quickly at any speed.

Nevertheless, the study discovered that higher speeds actually increase fatigue life, particularly at 15000 RPM. This may be due to the fact that there are conditions for better lubrication, the load is more evenly distributed, and there is less stress in a single location. Quite surprisingly, at very high loads, fatigue life remains almost constant, meaning that such factors as lubricant thickness and how materials expand under heat become more significant. These findings indicate the necessity of taking into account temporary heat effects, lubrication regimes, and contact types in predicting fatigue life for high-speed applications. These findings from this study are highly relevant for designing and maintaining ACBBs in aerospace, automotive, and machine tool fields. In these applications, good lubrication methods, appropriate preload levels, and heat management are essential in ensuring bearings remain reliable and durable. Follow-up

studies should involve testing these numerical predictions and also investigating how the structure of materials, lubricant breakdown, and defects evolve under extreme conditions. This will enhance models for predicting and understanding bearing performance under real-world conditions.

Furthermore, The comprehensive analysis of bearing materials under dynamic loading conditions has revealed critical performance differences. Alloy steels, with their high stiffness and consistent load-deflection behaviour, are best suited for applications demanding minimal deformation and high structural rigidity. Nickel-based superalloys offer a balanced performance with moderate stiffness and fatigue life, making them suitable for high-temperature or aerospace environments. Titanium alloys, although less stiff, provide exceptional fatigue life at low to moderate loads, positioning them well for lightweight, low-load systems. As rotational speed increases, all materials experience reduced fatigue life and increased contact loads, emphasizing the need for careful material selection based on both operational speed and loading conditions. Overall, the results support the strategic use of each material depending on the specific performance priorities of stiffness, fatigue resistance, or weight efficiency in bearing design.

6.1. Summary of Findings

This thesis presents a comprehensive study of the mechanical behavior and fatigue performance of angular contact ball bearings (ACBBs) under variable loads and rotational speeds using a newly developed a novel mathematical and theoretical coupled model. The model incorporates critical multiphysics phenomena—elastohydrodynamic lubrication (EHL), transient heat generation, centrifugal effects, and multiparticle contact mechanics—to provide a more accurate and realistic prediction of bearing performance.

The study highlights several key findings:

- The proposed model consistently predicts higher contact loads on both inner and outer raceways compared to the classical Harris model. This is due to its inclusion of thermal expansion, EHL effects, and dynamic contact deformations, especially under high load and low-speed conditions.

- Contact angles are shown to shift significantly with increasing axial load and speed. The inner contact angle decreases while the outer increases, indicating a redistribution of load that is more accurately captured by the new model.
- Friction torque increases nonlinearly with applied load. While load-dependent rolling friction is unaffected by speed, spinning and viscous friction are highly sensitive to speed. The total friction torque and heat generation escalate rapidly at higher speeds and loads, with the inner raceway identified as the primary source of frictional power loss.
- The study confirms that bearing fatigue life decreases with increasing load but can improve at very high rotational speeds (e.g., 15,000 RPM) due to enhanced lubrication and load redistribution effects. This behavior was not captured accurately by the Harris model, which overlooks such dynamic phenomena.
- A comparative analysis of bearing materials reveals that alloy steels provide the highest stiffness and contact load capacity, titanium alloys offer the best fatigue life under light loads, and nickel-based superalloys strike a balance between strength and endurance. However, titanium's fatigue performance deteriorates faster with increasing speed and load.

6.2 Significance of the Study

This work contributes significantly to the field of bearing design and analysis by addressing the limitations of traditional models and offering a more robust predictive framework. The integration of thermal, lubrication, and material effects provides a deeper understanding of real-world bearing behavior, which is essential for:

- Enhancing bearing design in aerospace, automotive, and industrial machinery.
- Reducing operational failures and unplanned downtimes.
- Optimizing lubrication and cooling systems.
- Supporting material selection for specialized applications.

By providing a unified and comprehensive approach to bearing performance analysis, this thesis helps bridge the gap between theory and practical engineering needs.

6.3. Contributions

The main contributions of this thesis include:

- Development of an advanced mathematical and theoretical coupled model that integrates EHL, thermal effects, and particle dynamics for realistic simulation of ACBB behavior.
- Demonstration of the limitations of the Harris model and justification for more physics-informed models in high-speed bearing applications.
- Extensive evaluation of the interactions between speed, load, material properties, and fatigue life, providing deeper insights into the design and maintenance of rolling element bearings.
- Provision of actionable recommendations for material selection and lubrication strategies in aerospace, automotive, and industrial applications.

6.4. Practical Implications

The findings have strong implications for engineering practice:

- Predictive maintenance can be improved by using more accurate contact and fatigue models that account for operational speed and thermal effects.
- Better material selection can be made for specific applications—e.g., using titanium alloys for low-load, high-speed environments or alloy steels for heavy-duty use.
- Improved lubrication and heat management systems should be considered in high-speed bearings to minimize frictional losses and extend operational life.

6.5. Limitations

While the model offers several improvements over traditional approaches, the study is not without limitations:

- The results are based on numerical simulations and require experimental validation to confirm accuracy.
- Surface roughness, real-life lubricant degradation, and manufacturing tolerances were not included but can influence bearing behavior significantly.
- The defect evolution and failure mechanisms under prolonged use or in the presence of contamination were not modelled.

6.6. Recommendations for Future Work

To build on the outcomes of this research, the following directions are recommended:

1. Experimental validation of the proposed model using test rigs and high-speed bearing test data.
2. Integration of realistic surface profiles, lubricant degradation models, and contamination effects.
3. Extension of the model to include crack initiation, defect propagation, and long-term reliability prediction.
4. Development of a digital twin framework for online monitoring, simulation, and predictive maintenance of rotating machinery using the proposed model as a core engine.

Reference

[1] E. V. Zaretsky, " Rolling Bearing Life Prediction, Theory, and Application," no. NOV 2016. [Online]. Available: https://ntrs.nasa.gov/api/citations/20160013905/downloads/20160013905.pdf.

[2] T. Lazović, A. Marinković, I. Atanasovska, M. Sedak, and B. Stojanović, "From Innovation to Standardization—A Century of Rolling Bearing Life Formula," *Machines,* vol. 12, no. 7, p. 444, 2024. [Online]. Available: https://www.mdpi.com/2075-1702/12/7/444.

[3] T. A. - Harris and R. M. - Barnsby, "Tribological Performance Prediction of Aircraft Gas Turbine Mainshaft Ball Bearings," *Tribology Transactions* vol. - 41, no. - 1, pp. – 68, 1998, doi: https://doi.org/10.1080/10402009808983722.

[4] K. A. - Arkhitskaya, V. P. - Monahova, and V. A. - Afanasyev, "- Measurement of Axial Loads on the Rotor Bearings of Gas-Turbine Engines," vol. - 43, no. - 6, pp. – 676, 2023, doi: https://doi.org/10.3103/S1068798X23060047.

[5] J. Piotrowski, *Shaft alignment handbook*. Crc Press, 2006 doi: https://doi.org/10.1201/9781420017878.

[6] L. P. J. - Tipton, "Bearing Load Measurements on a 3-Shaft Gas Turbine," *Applied Mechanics and Materials,* vol. - 1-2, pp. – 232, September 2004 2004, doi: https://doi.org/10.4028/www.scientific.net/AMM.1-2.225.

[7] F. C. Ke Yan; Bin Fang; Bei Yan, "Advances in Bearing Lubrication and Thermodynamics 2023," *Lubricants*, no. 2023, doi: https://doi.org/10.3390/books978-3-7258-1130-4.

[8] G. Hallgren and I. T. T. F. Ab, "Shaft and Bearing Calculations," *High temperature,* vol. 2, p. 1.

[9] S. Gao, S. Chatterton, L. Naldi, and P. Pennacchi, "Ball bearing skidding and over-skidding in large-scale angular contact ball bearings: Nonlinear dynamic model with thermal effects and experimental results," *Mechanical Systems and Signal Processing,* vol. 147, p. 107120, 2021/01/15/ 2021, doi: https://doi.org/10.1016/j.ymssp.2020.107120.

[10] S. Gao, S. Chatterton, P. Pennacchi, Q. Han, and F. Chu, "Skidding and cage whirling of angular contact ball bearings: Kinematic-hertzian contact-thermal-elasto-hydrodynamic model with thermal expansion and experimental validation," *Mechanical Systems and Signal Processing,* vol. 166, p. 108427, 2022/03/01/ 2022, doi: https://doi.org/10.1016/j.ymssp.2021.108427.

[11] C. Wen, X. Meng, C. Fang, J. Gu, L. Xiao, and S. Jiang, "Dynamic behaviors of angular contact ball bearing with a localized surface defect considering the influence of cage and oil lubrication," *Mechanism and Machine Theory,* vol. 162, p. 104352, 2021/08/01/ 2021, doi: https://doi.org/10.1016/j.mechmachtheory.2021.104352.

[12] C. Mishra, A. K. Samantaray, and G. Chakraborty, "Ball bearing defect models: A study of simulated and experimental fault signatures," *Journal of Sound and Vibration,* vol. 400, pp. 86–112, 2017/07/21/ 2017, doi: https://doi.org/10.1016/j.jsv.2017.04.010.

[13] S. Gao, L. Wang, and Y. Zhang, "Modeling and dynamic characteristic analysis of high speed angular contact ball bearing with variable clearance," *Tribology International,* vol. 182, p. 108330, 2023/04/01/ 2023, doi: https://doi.org/10.1016/j.triboint.2023.108330.

[14] Z. Chunjiang, Y. Xiaokai, H. Qingxue, G. Shidong, and G. Xin, "Analysis on the load characteristics and coefficient of friction of angular contact ball bearing at high speed," *Tribology International,* vol. 87, pp. 50–56, 2015/07/01/ 2015, doi: https://doi.org/10.1016/j.triboint.2015.02.012.

[15] Y. Wang, W. Wang, S. Zhang, and Z. Zhao, "Investigation of skidding in angular contact ball bearings under high speed," *Tribology International,* vol. 92, pp. 404–417, 2015/12/01/ 2015, doi: https://doi.org/10.1016/j.triboint.2015.07.021.

[16] M. Xu, M. Wang, D. He, X. Ding, Y. Shao, and F. Gu, "Skidding behavior of lubricated rolling element bearings under the influence of oil film and radial clearances," *Tribology International,* vol. 194, p. 109500, 2024/06/01/ 2024, doi: https://doi.org/10.1016/j.triboint.2024.109500.

[17] W. W. Wang Yunlong, Li Yulong, Zhao Ziqiang, "Lubrication and Thermal Failure Mechanism Analysis in High-Speed Angular Contact Ball Bearing," *Journal of Tribology* 2018, doi: https://doi.org/10.1115/1.4038356.

[18] J. Zhang, B. Fang, J. Hong, and Y. Zhu, "Effect of preload on ball-raceway contact state and fatigue life of angular contact ball bearing," *Tribology International,* vol. 114, pp. 365–372, 2017/10/01/ 2017, doi: https://doi.org/10.1016/j.triboint.2017.04.029.

[19] T. Xu *et al.*, "A preload analytical method for ball bearings utilising bearing skidding criterion," *Tribology International,* vol. 67, pp. 44–50, 2013/11/01/ 2013, doi: https://doi.org/10.1016/j.triboint.2013.06.017.

[20] W. W. F. X. J. H. Y. Li, "Investigating effects of non-uniform preload on the thermal characteristics of angular contact ball bearings through simulations," *Journal of Engineering Tribology,* vol. Volume 228, Issue 6, 2014, doi: https://doi.org/10.1177/1350650114524185.

[21] D. Zheng, W. Chen, and D. Zheng, "An enhanced estimation on heat generation of angular contact ball bearings with vibration effect," *International Journal of Thermal Sciences,* vol. 159, p. 106610, 2021/01/01/ 2021, doi: https://doi.org/10.1016/j.ijthermalsci.2020.106610.

[22] X. Shi, L. Wang, and F. Qin, "Relative fatigue life prediction of high-speed and heavy-load ball bearing based on surface texture," *Tribology International,* vol. 101, pp. 364–374, 2016/09/01/ 2016, doi: https://doi.org/10.1016/j.triboint.2016.05.007.

[23] M. J. Martin, Alanou, M. P., Evans, H. P., Snidle, R. W., Kawamura, H., & Dodd, A. , "Scuffing Performance of M50 Bearing Steel Lubricated with a Gas Turbine Engine Oil at High Sliding Speeds," *Tribology Transactions,* vol. 44(3), 465–471, 2001, doi: https://doi.org/10.1080/10402000108982482.

[24] G. S. Reichenbach, Accinelli, J. B., & Beaubien, S. J., " Lubrication of High-Speed High-Temperature Thrust Ball Bearings," *A S L E Transactions,* vol. 1(2), 259–265, 1958, doi: https://doi.org/10.1080/05698195808972339.

[25] H. Wang, H. Lv, and Z. Luo, "Analysis of Mechanical Properties and Fatigue Life of Microturbine Angular Contact Ball Bearings under Eccentric Load

Conditions," *Sensors*, vol. 23, no. 9, doi: https://doi.org/10.3390/s23094503.
[26] F. Kong, W. Huang, Y. Jiang, W. Wang, and X. Zhao, "A Vibration Model of Ball Bearings with a Localized Defect Based on the Hertzian Contact Stress Distribution," *Shock and Vibration,* vol. 2018, no. 1, p. 5424875, 2018/01/01 2018, doi: https://doi.org/10.1155/2018/5424875.
[27] J. Liu, L. Wang, and Z. Shi, "Dynamic modelling of the defect extension and appearance in a cylindrical roller bearing," *Mechanical Systems and Signal Processing,* vol. 173, p. 109040, 2022/07/01/ 2022, doi: https://doi.org/10.1016/j.ymssp.2022.109040.
[28] S. Gao *et al.*, "Experimental and theoretical approaches for determining cage motion dynamic characteristics of angular contact ball bearings considering whirling and overall skidding behaviors," *Mechanical Systems and Signal Processing,* vol. 168, p. 108704, 2022/04/01/ 2022, doi: https://doi.org/10.1016/j.ymssp.2021.108704.
[29] T. A. Harris and M. N. Kotzalas, *Rolling bearing analysis-2 volume set*. Crc Press, 2006 doi: https://doi.org/10.1201/9781482275148.
[30] A. B. Jones, "Ball Motion and Sliding Friction in Ball Bearings," *Journal of Basic Engineering,* vol. 81, no. 1, pp. 1–12, 1959, doi: https://doi.org/10.1115/1.4008346.
[31] M. - Schierz, "- Plastische Konditionierung von Pressverbindungen in der Antriebstechnik – ein Verfahren mit Potenzial," vol. - 84, no. - 4, pp. – 355, 2020, doi: https://doi.org/10.1007/s10010-020-00419-w.
[32] A. Harnoy, *Bearing design in machinery: engineering tribology and lubrication*. CRC press, 2002 doi: https://doi.org/10.1201/9780203909072.
[33] eassistant. "Interference Fits According to DIN 7190." https://www.eassistant.eu/fileadmin/dokumente/eassistant/etc/HTMLHandbuch/en/eAssistantHandbch15.html (accessed May 2025.
[34] SKF. "Principles of rolling bearing selection." https://www.skf.com/mena/products/rolling-bearings/principles-of-rolling-bearing-selection (accessed 12/05, 2025).
[35] T. o. Fits. "How to Choose the Right Fits in Engineering." https://www.mechdaily.com/what-are-different-types-of-fits/ (accessed.
[36] W. G. Robertson and D. Dowson, "Paper R4: A Review of the 1964 A.S.M.E.—A.S.L.E. International Lubrication Conference*," *Proceedings of the Institution of Mechanical Engineers, Conference Proceedings,* vol. 179, no. 10, pp. 15–26, 1964/06/01 1964, doi: https://doi.org/10.1243/PIME_CONF_1964_179_261_02.
[37] H. Martin, "Lubrication of gear teeth," vol. 102, p. 119, 1916. [Online]. Available: https://cir.nii.ac.jp/crid/1574231874336311040.
[38] J. F. J. W. Osterle, "On the hydrodynamic lubrication of roller-bearings," vol. 2, pp. 195–202, 1959, doi: https://doi.org/10.1016/0043-1648(59)90004-3.
[39] L. B. Sargent Jr, "Pressure-Viscosity Coefficients of Liquid Lubricants," *A S L E Transactions,* vol. 26, no. 1, pp. 1–10, 1983/01/01 1983, doi: https://doi.org/10.1080/05698198308981471.

[40] D. E. Brewe and B. J. Hamrock, "Simplified solution for elliptical-contact deformation between two elastic solids," 1977, doi: https://doi.org/10.1115/1.3453245.
[41] J. K. Evans CR, " The Rheological Properties of Elastohydrodynamic Lubricants," *Proceedings of the Institution of Mechanical Engineers, Part C: Journal of Mechanical Engineering Science,* vol. 1986;200(5):303-312., 1986, doi: https://doi.org/10.1243/PIME_PROC_1986_200_134_02.
[42] S. - Deng, L. - Hua, X. - Han, and S. - Huang, "- Investigation of rolling contact fatigue cracks in ball bearings," vol. - 188, no. - 1, pp. – 78, 2014, doi: https://doi.org/10.1007/s10704-014-9947-3.
[43] G. Lundberg and A. Palmgren, "Dynamic capacity of rolling bearings," 1949, doi: https://doi.org/10.1115/1.4009930.
[44] B. Trivia. "Bearing Failure (Part 2): Causes and countermeasures for bearing failure (I)." https://koyo.jtekt.co.jp/en/bearing-column/bearing_trivia_3rd_series/bearing_trivia_3rd_series_02.html (accessed.
[45] BearingNews. "Ultrasonic Testing Provides Highly Accurate Bearing Life Predictions." https://www.bearing-news.com/world-first-ultrasonic-testing-provides-highly-accurate-bearing-life-predictions/ (accessed.
[46] "A brief history of Matlab. MATLAB & Simulink. (n.d.). https://au.mathworks.com/company/technical-articles/a-brief-history-of-matlab.html ".
[47] C. Moler and J. Little, "A history of MATLAB," *Proceedings of the ACM on Programming Languages,* vol. 4, no. HOPL, pp. 1–67, 2020, doi: https://doi.org/10.1145/3386331.
[48] "Wikimedia Foundation. (2025, June 24). Matlab. Wikipedia. https://en.wikipedia.org/wiki/MATLAB ".

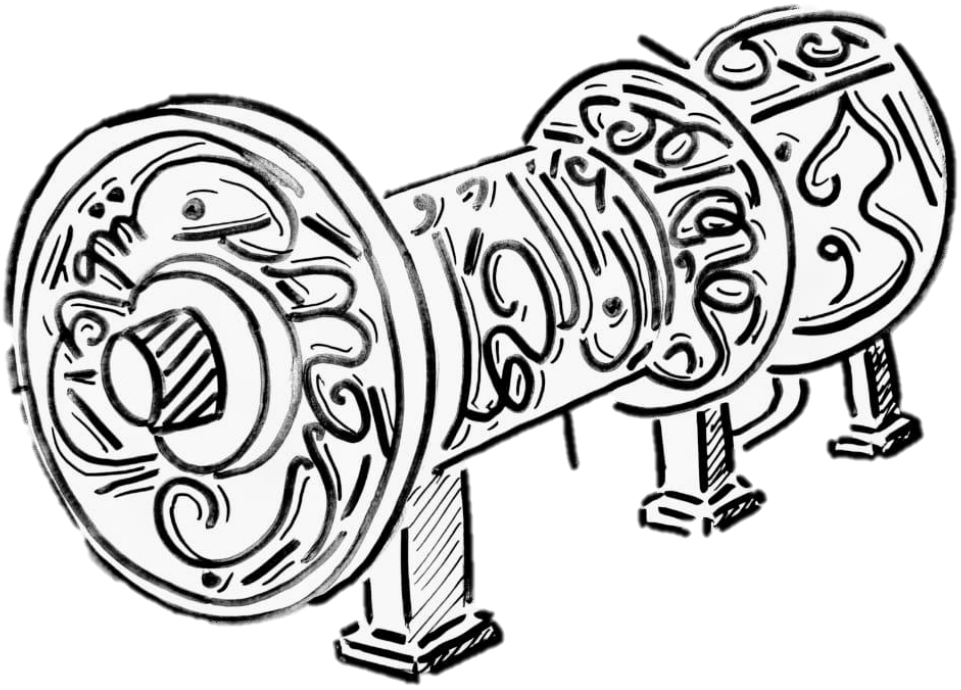

List of Figures

Figure 3.1: An angular contact ball bearing's cross section [13] 28
Figure 3.2: Rolling elements angular positions in ψz plane [29] 33
Figure 3.3: Positions of the raceway groove curvature centres and ball centre at angular position ψ, both with and without load applied [29] 34
Figure 3.4: Ball loading at angular position ψ_j [29] 37
Figure 3.5: Ball mass element instantaneous position dm [29] 38
Figure 3.6: Contacting bodies geometry [29] 39
Figure 3. 7: Axial deflection constant K for ball bearings vs total curvature B [29] .. 41
Figure 3.8: Point-contact ellipsoidal surface compressive stress distribution [29] 43
Figure 3. 9: S-N curve for mild steel [29] 50
Figure 3. 10: A typical fatigue failure in a ball bearing raceway [44] 50
Figure 3.11: A diagram showing how the fatigue starts beneath the surface of the metal [45] 52
Figure 3.12: Flowchart of the coupled iterative algorithm for solving mechanical-thermal-lubrication equilibrium in the proposed model 54
Figure 4. 1: Effect of applied load on the inner raceway contact load at 6000 RPM 59
Figure 4.2: Effect of applied load on the inner raceway contact load at 10000 RPM 59
Figure 4.3: Effect of applied load on the inner raceway contact load at 15000 RPM 60
Figure 4.4: Effect of applied load on the outer raceway contact load at 6000 RPM 62
Figure 4. 5: Effect of applied load on the outer raceway contact load at 10000 RPM 62
Figure 4.6: Effect of applied load on the outer raceway contact load at 15000 RPM 63
Figure 4. 7: Effect of applied load on the ball raceway contact angles at various speeds, (a) 6000 RPM, (b) 10000 RPM, and (c) 15000 RPM 67
Figure 4.8: Effect of applied load on the bearing friction at various speeds, (a) spinning friction, (b), Load friction, (c) Viscous friction, and (d) Total friction torque 71
Figure 4.9: Effect of applied load on the friction power loss at various speeds regarding (a) Outer raceway and (b) Inner raceway 72

Figure 4.10: Effect of applied load on the bearing friction heat generated at various speeds, (a) spinning friction heat, (b), Viscous friction heat, (c) Load friction heat, and (d) Total friction heat 75
Figure 4.11: Effect of applied load on the dynamics capacity at various speeds regarding (a) inner raceway and (b) outer raceway 78
Figure 4.12: Bearing fatigue life behaviour for (a) various speeds and (b) various applied load 79
Figure 4.13: Variation of centrifugal force with applied load at different rotational speeds 80
Figure 4.14: Load-deflection constants of ball bearing inner raceway for different materials with respect to (a) applied load and (b) rotating speed 81
Figure 4.15: The normal contact load behaviour of the bearing inner raceway for different materials with respect to (a) applied load and (b) rotating speed 82
Figure 4.16: The fatigue life behaviour of the bearing across different materials with respect to (a) applied load and (b) rotating speed 83
Figure 5. 1: Selected screenshots of the main data page in the Excel file generated by MATLAB code 95
Figure 5. 2: A screenshot of the data page from the Excel file displaying the results for contact angles and normal loads 97
Figure 5. 3: A screenshot of basic dynamic capacity analysis of angular contact bearings under varying loads and rotational speeds 98
Figure 5. 4: Screenshots of centrifugal forces, resultant bearing loads and frictional torque under varying speeds and applied loads 100
Figure 5. 5: Screenshots of friction torque due to spinning, viscous friction torque and total friction torque on the bearing 102
Figure 5. 6: Screen captures of the results for bearing frictional power loss, spinning friction heat, and viscous friction heat generation rate 104
Figure 5. 7: screen captures depict the results related to load friction heat generation rate and total friction heat generation rate 106
Figure 5. 8: Screen captures present the results of the bearing conducted heat and bearing convected heat 108
Figure 5. 9: Deformation and fatigue life analysis of angular contact ball bearings under applied load and varying rotational speeds screenshot 110

List of Tables

Table 3.1: Dimensionless contact parameter 44
Table 3.2: Heat generation parameters and their values..... 49
Table 4. 1:Primary input parameters for numerical simulations..... 57
Table 4. 2: compassion among the proposed model and Harris model regarding normal contact loads 65
Table 4. 3: A compass sion among the proposed model and Harris model regarding contact angles 68

Appendix

Appendix A: The Written Code

```
clear
clc
close all;
format long;
c_c=1;
count=1;
cellArray{1,1}='RPM';
cellArray{1,2}="Applied load";
cellArray{1,3}="Kit";
cellArray{1,4}="Kot";
cellArray{1,5}="alpha_i";
cellArray{1,6}="alpha_o";
cellArray{1,7}="gamma_i";
cellArray{1,8}="gamma_o";
cellArray{1,9}="X1";
cellArray{1,10}="X2";
cellArray{1,11}="delta_i";
cellArray{1,12}="delta_o";
cellArray{1,13} = "FC";
cellArray{1,14} = "Msi";
cellArray{1,15} = "Mso";
cellArray{1,16} = "P1";
cellArray{1,17} = "M1";
cellArray{1,18} = "Mv";
cellArray{1,19} = "Mtotal";
cellArray{1,20} = "Hfi";
cellArray{1,21} = "Hfo";
cellArray{1,22} = "H1v";
cellArray{1,23} = "Hi_total";
cellArray{1,24} = "Hci";
cellArray{1,25} = "Hco";
cellArray{1,26} = "Hvi";
cellArray{1,27} = "Hvo";
cellArray{1,28} = "Qi";
cellArray{1,29} = "Qo";
cellArray{1,30} = "Skd_theo";
```

```
cellArray{1,31} = "ki";
cellArray{1,32} = "ko";
cellArray{1,33}='Mg';
cellArray{1,34}='beta_deg';
cellArray{1,35}="Li";
cellArray{1,36}="Lo";
cellArray{1,37}="L";
cellArray{1,38}="Ti";
cellArray{1,39}="To";
cellArray{1,40}="Type Oil";
cellArray{1,41}="Type Matrial";
cellArray{1,42}='Qci';
cellArray{1,43}='Qci_prime';
cellArray{1,44}='Qco';
cellArray{1,45}='SpinFH';
cellArray{1,46}='H1v';
cellArray{1,47}='LoadF';
cellArray{1,48}='TotFH';

%Store all data of all Postion of epsi
allArray{1,1}='RPM';
allArray{1,2}="Applied load";
allArray{1,3}="Kit";
allArray{1,4}="Kot";
allArray{1,5}="alpha_i";
allArray{1,6}="alpha_o";
allArray{1,7}="gamma_i";
allArray{1,8}="gamma_o";
allArray{1,9}="X1";
allArray{1,10}="X2";
allArray{1,11}="delta_i";
allArray{1,12}="delta_o";
allArray{1,13} = "FC";
allArray{1,14} = "Msi";
allArray{1,15} = "Mso";
allArray{1,16} = "P1";
allArray{1,17} = "M1";
allArray{1,18} = "Mv";
allArray{1,19} = "Mtotal";
allArray{1,20} = "Hfi";
allArray{1,21} = "Hfo";
```

```
78- allArray{1,22} = "H1v";
79- allArray{1,23} = "Hi_total";
80- allArray{1,24} = "Hci";
81- allArray{1,25} = "Hco";
82- allArray{1,26} = "Hvi";
83- allArray{1,27} = "Hvo";
84- allArray{1,28} = "Qi";
85- allArray{1,29} = "Qo";
86- allArray{1,30} = "Skd_theo";
87- allArray{1,31} = "ki";
88- allArray{1,32} = "ko";
89- allArray{1,33}='Mg';
90- allArray{1,34}='beta_deg';
91- allArray{1,35}="Li";
92- allArray{1,36}="Lo";
93- allArray{1,37}="L";
94- allArray{1,38}="Ti";
95- allArray{1,39}="To";
96- allArray{1,40}="Type Oil";
97- allArray{1,41}="Type Matrial";
98- allArray{1,42}='Qci';
99- allArray{1,43}='Qci_prime';
100-         allArray{1,44}='Qco';
101-         allArray{1,45}='SpinFH';
102-         allArray{1,46}='H1v';
103-         allArray{1,47}='LoadF';
104-         allArray{1,48}='TotFH';
105-
106-
107-         %Section select used Oil
108-         type_oil=["Synthetic oils" "Diester oils" "Mineral oil"];
109-         type_mat=["Titanium alloys" "Nickel-based superalloys" "Alloy
    Steels"];
110-
111-         select=input("Please Choose The Oil Type : (Synthetic oils,Diester
    oils,Mineral oil,other)",'s');
112-
113-         SSU0=[48 55 105];% SSU for mineral oil
114-         rho0_oil=[0.00085 0.00092 0.0008663]; % Oil density in g/mm^3
115-         vo0=[25.26 3.8 20];%Kinematic viscosity
116-
```

```
117-        switch select
118-          case "Synthetic oils"
119-            SSU = SSU0(1);
120-            rho_oil = rho0_oil(1);
121-            vo = vo0(1);
122-          case "Diester oils"
123-            SSU = SSU0(2);
124-            rho_oil = rho0_oil(2);
125-            vo = vo0(2);
126-          case "Mineral oil"
127-            SSU = SSU0(3);
128-            rho_oil = rho0_oil(3);
129-            vo = vo0(3);
130-          case "other"
131-            SSU = input("SSU for mineral oil: ");
132-            rho_oil = input("Oil density in g/mm^3: ");
133-            vo = input("Kinematic viscosity: ");
134-        end
135-
136-
137-        %Section select used Matrial
138-        select2=input("Please choose the type of material you want
    :(Titanium alloy,Nickel-based superalloys ,Alloy Steels,other)",'s');
139-
140-        Ei0=[110000 200000 210000];% Young's modulus for inner race in
    N/mm^2
141-        Eo0=[110000 200000 210000];% Young's modulus for outer race in
    N/mm^2
142-
143-        xi_i0=[0.34 0.30 0.28];% Poisson's ratio for inner race
144-        xi_o0=[0.34 0.30 0.28]; % Poisson's ratio for outer race
145-
146-        rho_i0=[0.0046 0.0087 0.00785];   % Inner race density in g/mm^2
147-        rho_o0=[0.0046 0.0087 0.00785];   % Outer race density in g/mm^3
148-
149-        Gamma_i0=[9.3E-6 14.8E-6 11.7E-6]; % Thermal expansion
    coefficient for inner race in mm/mm/°C
150-        Gamma_o0=[9.3E-6 14.8E-6 11.7E-6]; % Thermal expansion
    coefficient for outer race in mm/mm/°C
151-
152-
```

```
153-        switch select2
154-          case "Titanium alloy"
155-            E_i = Ei0(1);
156-            E_o = Eo0(1);
157-
158-            xi_i = xi_i0(1);
159-            xi_o = xi_o0(1);
160-
161-            rho_i = rho_i0(1);
162-            rho_o = rho_o0(1);
163-
164-            Gamma_i = Gamma_i0(1);
165-            Gamma_o = Gamma_o0(1);
166-
167-          case "Nickel-based superalloys"
168-            E_i = Ei0(2);
169-            E_o = Eo0(2);
170-
171-            xi_i = xi_i0(2);
172-            xi_o = xi_o0(2);
173-
174-            rho_i = rho_i0(2);
175-            rho_o = rho_o0(2);
176-
177-            Gamma_i = Gamma_i0(2);
178-            Gamma_o = Gamma_o0(2);
179-
180-          case "Alloy Steels"
181-            E_i = Ei0(3);
182-            E_o = Eo0(3);
183-
184-            xi_i = xi_i0(3);
185-            xi_o = xi_o0(3);
186-
187-            rho_i = rho_i0(3);
188-            rho_o = rho_o0(3);
189-
190-            Gamma_i = Gamma_i0(3);
191-            Gamma_o = Gamma_o0(3);
192-
193-          case "other"
```

```
194-            E_i = input("Young's modulus for inner race in N/mm^2: ");
195-            E_o = input("Young's modulus for outer race in N/mm^2: ");
196-
197-            xi_i = input("Poisson's ratio for inner race: ");
198-            xi_o = input("Poisson's ratio for outer race: ");
199-
200-            rho_i = input("Inner race density in g/mm^2: ");
201-            rho_o = input("Outer race density in g/mm^3: ");
202-
203-            Gamma_i = input("Thermal expansion coefficient for inner race
    in mm/mm/°C: ");
204-            Gamma_o = input("Thermal expansion coefficient for outer
    race in mm/mm/°C: ");
205-        end
206-
207-
208-        %  Section Given parameters
209-            D = 22.23; % Ball diameter in mm
210-            r_i = 11.63; % Inner groove radius in mm
211-            alpha_node=40*pi/180; % Nominal contact angle in radian
212-            r_o = 11.63; % Outer groove radius in mm
213-            %SSU = 40; % Mineral oil in SSU
214-            G = 10000; % Gravitationalacceleration constant in mm/sec^2
215-            %rho_oil = 0.00085; % Oil density in g/mm^3
216-            rho_ball = 7810; % Rolling element density in g/m^3
217-            l_0 = 0.014; % Interference of the bearing initial installation for
    bearing shaft contact in mm
218-            l_0_outer = 0.0113; % Interference of the bearing initial
    installation for bearing housing contact in mm
219-            d_i = 102.8; % Inner raceway diamete in mm
220-            D_b = 63.5; % Shaft diamete in mm
221-            %E_i = 206900; % Elastic modulus of inner ring N/mm^2
222-            E_s = 206900; % Elastic modulus of housing ring N/mm^2
223-            D_s = 90; % Bore diamete in mm
224-            xi_s = 0.3; % Poisson's ratio of housing
225-            D_h = 160; % Housing diamete in mm
226-            do = 147.73; % Outer raceway diamete in mm
227-            di = 102.8;  % Inner raceway diameter in mm
228-            ro = 11.63;  % Outer groove radius in mm
229-            rho_s = 0.00785; % Shat density in g/mm^2
230-            d_o = 147.7; % Outer raceway diamete in mm
```

```
231-        %rho_i = 0.00785; % Inner raceway density in g/mm^2
232-        %Gamma_i = 11.7e-6; % Thermal expansion coefficient for inner
    raceway in mm/mm/°C
233-        D_o = 160; % Housing diamete in mm
234-        lambda_ij = 1 % Control parameter of the inner ring groove
235-        lambda_oj = 1 % Control parameter of the outer ring groove
236-        %E_o = 206900; Elastic modulus of ouer ring in N/mm^2
237-        E_h = 206900; % Elastic modulus of housing in N/mm^2
    N/mm^2
238-        E_b=206900;  % Elastic modulus of ball N/mm^2
239-        D_h = 203.2; % Housing effective outer diameter in mm
240-        xi_h = 0.3;  % Poisson's ratio of bearing housing
241-        xi_b=0.3; % Poisson's ratio of bearing rolling element
242-        %rho_o = 0.00785; % Outer raceway density in g/mm^2
243-        omega_o = 0.0; % Outer ring speed in RPM
244-        rho_h = 0.00785; % Housing raceway density in g/mm^2
245-        T_a = 23; % Ambient temperature in °C
246-        T_i = 24; % Inner ring temperature in °C
247-        T_o = 24; % Outr ring temperature in °C
248-        T_h = 24; % Housing temperature in °C
249-        Ts= 23; % Shaft temperature in °C
250-        %Gamma_o = 11.7e-6; % Thermal expansion coefficient for
    outer raceway in mm/mm/°C
251-        Gamma_h = 8.5e-6; %  Thermal expansion coefficient for
    housing in mm/mm/°C
252-        Z = 16; % Rolling element number "how many balls in the
    bearing?"
253-        do = 147.7; % Outer raceway diamete in mm
254-        Fr = 0; % Radial applied load in N
255-        M = 0; % Appied moment in N.m
256-        %vo=5 Oil Kinematic viscosity;
257-
258-        % Initial value Section
259-        X1_b1 = [-1 0.5 0.18 0.2 0.01 0.1 -0.01 0.1 0.01 0.01 0.01 0.01 0.01
    0.01 0.01 0.01 0.001 -0.01 0.001 0.01];
260-
261-        X1_b2 = [0.2 0.01 0.01 0.01 0.01 0.01 0.01 0.01 0.01 0.01 0.01
    0.01 0.01 0.01 0.01 0.01 0.01 0.01 0.01 0.001];
262-
263-        X1_b3 = [0.002 0.003 0.0001 0.001 0.0001 0.0001 0.0001 0.033
    0.1 0.1 0.001 0.01 0.01 0.01 0.01 0.01 0.01 0.001 0.001 0.001];
```

```
X1_b=[X1_b1 X1_b2 X1_b3];

X2_b1 = [0.53 0.5002 0.468 0.44801 0.43594 0.4268 0.4202
    0.4153 0.41108 0.408 0.4052 0.40399 0.4021 0.4012 0.40066 0.39967
    0.39793 0.3978 0.3973 0.3956];
X2_b2 = [0.6 0.51797 0.51183 0.50282 0.4923 0.4807 0.4699
    0.4592 0.4472 0.4398 0.43223 0.4277 0.42328 0.42062 0.4172 0.41499
    0.41406 0.41363 0.41115 0.41045];

X2_b3 = [0.53 0.523646 0.52213 0.52 0.516 0.5111 0.5056 0.5
    0.4938 0.4873 0.4809 0.4743 0.4685 0.4626 0.4573 0.4531 0.4496 0.4465
    0.44435 0.4367];
X2_b=[X2_b1 X2_b2 X2_b3];

delta_i_b1 = [0.00006 0.00115 0.00179 0.00134 0.00367 0.00284
    0.00304 0.00293 0.00294 0.00289 0.002781 0.0027 0.0026 0.00248
    0.00238 0.00224 0.00214 0.00212 0.00745 0.00757];
delta_i_b2 = [0.0004 0.0011 0.0022 0.0036 0.0042 0.0047 0.006
    0.007 0.006999 0.0078 0.0087 0.009 0.0088 0.0103 0.0104 0.0103 0.0107
    0.0107 0.0089 0.000222];
delta_i_b3 = [0.0002 0.00154 0.0026 0.0025 0.002208 0.0022
    0.00233 0.00084 0.00196 0.00194 0.001 0.00093 0.00087 0.00082
    0.00077 0.00074 0.0007 0.00135 0.0012 0.1252];
delta_i_b=[delta_i_b1 delta_i_b2 delta_i_b3];

delta_o_b1= [0.00305, 0.00297, 0.00367, 0.00432, 0.00523,
    0.00609, 0.00681, 0.00733, 0.00800, 0.00860, 0.00912, 0.00973,
    0.01030, 0.01083, 0.01139, 0.01192, 0.01253, 0.01313, 0.01329,
    0.01377];
delta_o_b2 = [0.0055 0.0054 0.0057 0.0059 0.00634 0.007 0.0075
    0.0081 0.0084 0.00896 0.00948 0.01 0.01043 0.01094 0.0115 0.01196
    0.01244 0.0129 0.0134 0.01506];
delta_o_b3 = [0.00955 0.00956 0.0099 0.0096 0.0096 0.00967
    0.009991 0.0099 0.0102 0.0104 0.0108 0.0111 0.01153 0.01206 0.0125
    0.0129 0.0134 0.0138 0.01436 0.0104];

delta_o_b=[delta_o_b1 delta_o_b2 delta_o_b3];

delta_a_b1 = [-0.2082, -0.0844, -0.0229, -0.0055, 0.0064, 0.0154,
    0.0229, 0.0277, 0.0335, 0.0373, 0.0412, 0.0447, 0.0477, 0.0532, 0.0532,
    0.0561, 0.0581, 0.0619, 0.0658, 0.0658];
```

```
284-
285-        delta_a_b2 = [-0.2254 -0.1658 -0.113 -0.0739 -0.0469 -0.0233 -
    0.0053 0.0074 0.0187 0.0261 0.0325 0.0379 0.0416 0.0736 0.0488 0.0506
    0.0539 0.0576 0.0605 0.0666];
286-        delta_a_b3 = [-0.2196 -0.1924 -0.165 -0.1395 -0.1154 -0.0947 -
    0.075 -0.0581 -0.0411 -0.0251 -0.0123 -0.0006 0.0094 0.0169 0.023
    0.0289 0.034 0.0394 0.0423 0.0519];
287-
288-        delta_a_b=[delta_a_b1 delta_a_b2 delta_a_b3];
289-
290-
291-        Delta_r_b1 = [0.0098, 0.003, -0.0006, -0.0038, -0.0057, -0.00747,
    -0.00763, -0.0074, -0.00923, -0.00858, -0.00973, -0.0089, -0.0095, -
    0.00943, -0.0094, -0.0101, -0.0128, -0.01425, -0.01574, -0.02124];
292-        Delta_r_b2 = [0.0806 -0.0036 -0.0037 -0.00356 -0.00354 -0.00277
    -0.00199 -0.0014 -0.0057 -0.0068 -0.00999 -0.0106 -0.01126 -0.0117 -
    0.01287 -0.01344 -0.01381 -0.0137 -0.01585 -0.01606];
293-        Delta_r_b3 = [-0.0069 -0.0084 -0.005 -0.003 -0.001 -0.0036 -
    0.004 -0.007 -0.009 -0.0092 -0.0099 -0.011 -0.01 -0.0122 -0.013 -0.0131 -
    0.0148 -0.015 -0.0162 -0.018];
294-        Delta_r_b=[Delta_r_b1 Delta_r_b2 Delta_r_b3];
295-
296-        Theta_b1 = [0.01, 0.01, 0.01, -0.001, 0.01, 0.001, 0.01, 0.001,
    0.001, 0.001, 0.001, 0.001, 0.001, 0.001, 0.001, 0.001, 0.001, 0.0001, -
    0.01, -0.01];
297-        Theta_b2 = [0.01 0.02 0.02 0.02 0.02 0.02 0.02 0.02 0.02 0.02 0.02
    0.02 0.02 0.02 0.02 0.02 0.02 0.02 0.02 0.02];
298-        Theta_b3 = [0.01 -0.001 0.00148 0.00148 0.00148 0.0015 -0.0015
    0.019 0 0 0.01 0.01 0.01 0.01 0.01 0.01 0.01 0.001 0.001 0.1];
299-        Theta_b=[Theta_b1 Theta_b2 Theta_b3];
300-
301-
302-
303-
304-        %Operation conditions Section
305-        F_new1=0:2500:47500;%the Speed (Target)6000
306-        F_new2=0:2500:47500;%the Speed (Target) 10000
307-        F_new3=0:2500:47500;%the Speed (Target)15000
308-        F_new=[F_new1 F_new2 F_new3];%the Load (Target)
309-         Error_Ti=3;
310-        Error_To=3;
```

```
311-        Ti_old=0;
312-        To_old=0;
313-        L=length(F_new);%length
314-        N_SPEED1=repmat(6000,1,20);%the Speed (Target) 6000
315-        N_SPEED2=repmat(10000,1,20);%the Speed (Target) 10000
316-        N_SPEED3=repmat(15000,1,20);%the Speed (Target) 15000
317-
318-        N_SPEED=[N_SPEED1 N_SPEED2 N_SPEED3];%the Speed (Target)
319-        A1=4;
320-        A2=6;
321-        %Start Loop
322-
323-        for F_aa=1:length(F_new)
324-
325-         %      Speed & Load
326-             N=N_SPEED(F_aa);
327-             Fa =F_new(F_aa);
328-         %  initial of value X1 & X2 & delta_i & delta_o & theta & delta_a &
    delta_r
329-             X1j_1= X1_b(F_aa);
330-             X2j_1 =X2_b(F_aa);
331-             delta_ij_1   =delta_i_b(F_aa);
332-             delta_oj_1 =delta_o_b(F_aa);
333-             delta_a =delta_a_b(F_aa);
334-             delta_r =Delta_r_b(F_aa);
335-             theta=Theta_b(F_aa);
336-
337-
338-           % Positions 16 values
339-           psi_j = [0, 0.3926990817, 0.7853981634, 1.1780972451,
    1.5707963268, 1.9634954085, 2.3561944902, 2.7488935719,
    3.1415926536, 3.534291735, 3.926990817, 4.319689899, 4.71238898,
    5.105088062, 5.497787144, 5.890486226];
340-
341-
342-          % Equations
343-           f_i = r_i / D; % Eq.1
344-           f_o = r_o / D; % Eq.2
345-           B = f_i + f_o - 1; % Eq.3
346-           d_m = 0.5 * (d_i + d_o); % Eq.4
347-           P_d = d_o - d_i - 2 * D; % Eq.5
```

```
348-            A = r_i + r_o - D; % Eq.6
349-            omega = 2 * pi * N / 60; % Eq.7
350-
351-            % Temperature effect on inner ring
352-            Delta_I_T_inner = Gamma_i * do * (T_o - T_a) - Gamma_i * d_i *
    (T_i - T_a);
353-            I_s = I_0 + Delta_I_T_inner;
354-            Delta_s = (2 * I_0 * (d_i / D_s)) / ((((d_i / D_s)^2) - 1) * (((d_i /
    D_s)^2 + 1) / ((d_i / D_s)^2 - 1) + xi_i) + (E_i / E_s) * ((((D_s / D_b)^2 + 1) /
    ((D_s / D_b)^2 - 1) - xi_s)));
355-            Delta_sn = (I_s / I_0) * Delta_s;
356-
357-            % Temperature effect on outer ring
358-            Delta_I_T_outer = Gamma_o * D_h * (T_o - T_a) - Gamma_h * D_h
    * (T_o - T_a);
359-            I_h = I_0_outer + Delta_I_T_outer;
360-            Delta_h = (2 * I_0_outer * (D_o / d_o)) / ((((D_o / d_o)^2) - 1) *
    (((D_o / d_o)^2 + 1) / ((D_o / d_o)^2 - 1) + xi_o) + (E_o / E_h) * ((((D_h /
    D_o)^2 + 1) / ((D_h / D_o)^2 - 1) - xi_h)));
361-            Delta_hn = (I_h / I_0_outer) * Delta_h;
362-
363-            % Other calculations
364-            Delta_P_d = -Delta_sn - Delta_hn;
365-            P_w = P_d + Delta_P_d;
366-            alpha_i = acos(max(min(1 - P_w / (2 * A), 1), -1));
367-
368-          % Small initial guess A1 & A2
369-
370-            %init value of varible to store output of N.R
371-            X1j = 3e-1 * ones(1, Z); % Small initial guess
372-            X2j = 5e-1 * ones(1, Z); % Small initial guess
373-            delta_oj = 1e-2 * ones(1, Z); % Small initial guess
374-            delta_ij = 1e-3 * ones(1, Z); % Small initial guess
375-
376-           %Start lOOP Postion of 16 epsi
377-           if Fa==0
378-
379-           %Calculted angle inner and outer
380-            p1=(A2-X2j_1);
381-            q1=((f_i-0.5)*D +delta_ij_1);
382-
```

```
383-        % cos and sin
384-         cos_alpha_ij =p1/q1;
385-         sin_alpha_ij = (A1-X1j_1)/((f_i-0.5)*D +delta_ij_1);
386-         cos_alpha_oj=X2j_1/((f_o-.5)*D +delta_oj_1);
387-         sin_alpha_0j=X1j_1/((f_o-.5)*D +delta_oj_1);
388-            gamma_o = (D * cos_alpha_oj) / d_m;
389-
390-         end
391-
392-
393-
394-        for j1=1:length(psi_j)
395-
396-         if j1==1
397-            gamma_i=((D*((B*D*cos(alpha_node)+delta_r*cos(psi_j(j1)))-
    X2j)/((f_i-0.5)*D+delta_ij)))/d_m;
398-
399-         end
400-        %Inner section
401-         m = rho_ball * (4 / 3) * pi * ((D * 1e-3) / 2)^3;
402-         Q_t = Fa / Z;
403-         dm = 0.5*(di + do); % Eq. 4
404-         ri = 11.63;              % Inner race radius in mm
405-         % Equations
406-         fi = ri / D; % Eq. 1
407-         Ri = dm/2 + (fi - 0.5) * D * cos(alpha_node); % Eq. 39
408-         fo = ro / D; % Eq. 2
409-
410-        %Outer section
411-          Jo = (1 / 60) * rho_ball * pi * ((D * 1e-3)^5);
412-          gamma_prime = D / d_m;
413-          tan_beta = sin_alpha_0j / (cos_alpha_oj + gamma_prime);
414-          beta_rad = atan(tan_beta);
415-          beta_deg = rad2deg(beta_rad);
416-
417-
418-          %Section of calcultions for Spn ratio and Orb ratio
419-          numerator_o = cos_alpha_oj + ((tan(beta_rad) * sin_alpha_0j));
420-          denominator_o = 1 + (gamma_prime * cos_alpha_oj);
421-          AA1= numerator_o/denominator_o;
422-          numerator_i = (cos_alpha_ij + ((tan(beta_rad) * sin_alpha_ij)));
```

```
423-        denominator_i = 1 - (gamma_prime * cos_alpha_ij);
424-        AA2= numerator_i/ denominator_i;
425-        AA3= gamma_prime * cos (beta_rad);
426-
427-        %spn
428-        omega_spn_over_omega= (-1/(((AA1)+(AA2))*AA3));
429-        AA4= (1-(gamma_prime*cos_alpha_ij));
430-        alpha_ij=acos(cos_alpha_ij);
431-        alpha_oj=acos(cos_alpha_oj);
432-        AA5=(1+(cos(alpha_ij-alpha_oj)));
433-        %orb
434-        omega_orb_over_omega= AA4/AA5;
435-
436-        %error
437-        M_g = Jo * 1e3 * (omega_spn_over_omega) *
    (omega_orb_over_omega) * omega^2 * sin(beta_rad);
438-        F_c = 0.5 * m * d_m * 1e-3 * (omega^2) *
    (omega_orb_over_omega)^2;
439-        alpha_o = acot(cot(alpha_i) + F_c / Q_t);
440-
441-        %init Ti and To
442-
443-
444-        n_m = 0.5 * omega * (1 - gamma_i);
445-        n_R = 0.5 * d_m / D * omega * (1 - gamma_i^2);
446-        R_i = d_m / 2 + (f_i - 0.5) * D * cos(alpha_node);
447-        R_x_i_inv = 2 / D + 2 / D * (gamma_i / (1 - gamma_i));
448-        R_y_i_inv = 2 / D + (-1 / (f_i * D));
449-        kappa_e_i = 1.0339 * (R_x_i_inv / R_y_i_inv)^0.636;
450-        E_e_i = 1.0003 + 0.5968 / (R_x_i_inv / R_y_i_inv);
451-        F_i = 1.5277 + 0.6023 * log(R_x_i_inv / R_y_i_inv);
452-        a_star_i = ((2 * kappa_e_i^2 * E_e_i) / pi)^(1 / 3);
453-        b_star_i = ((2 * E_e_i) / (pi * kappa_e_i))^(1 / 3);
454-        delta_star_i = (2 * F_i / pi * (pi / (2 * kappa_e_i^2 * E_e_i)))^(1 / 3);
455-        R_x_o_inv = 2 / D + (-2 / D * (gamma_i / (1 + gamma_i)));
456-        R_y_o_inv = 2 / D + (-1 / (f_o * D));
457-        kappa_e_o = 1.0339 * (R_x_o_inv / R_y_o_inv)^0.636;
458-        E_e_o = 1.0003 + 0.5968 / (R_x_o_inv / R_y_o_inv);
459-        F_o = 1.5277 + 0.6023 * log(R_x_o_inv / R_y_o_inv);
460-        a_star_o = ((2 * kappa_e_o^2 * E_e_o) / pi)^(1 / 3);
461-        b_star_o = ((2 * E_e_o) / (pi * kappa_e_o))^(1 / 3);
```

```
462-            delta_star_o = (2 * F_o / pi * (pi / (2 * kappa_e_o^2 * E_e_o)))^(1 /
    3);
463-            rho_o_sum = (1 / D) * (4 - 1 / f_o - (2 * gamma_i) / (1 + gamma_i));
464-            F_rho_o = (1 / f_o - (2 * gamma_i) / (1 + gamma_i)) / (4 - 1 / f_o - (2
    * gamma_i) / (1 + gamma_i));
465-            rho_i_sum = (1 / D) * (4 - 1 / f_i + (2 * gamma_i) / (1 - gamma_i));
466-            F_rho_i = (1 / f_i + (2 * gamma_i) / (1 - gamma_i)) / (4 - 1 / f_i + (2 *
    gamma_i) / (1 - gamma_i));
467-            K_H_i = (((2 * sqrt(2)) * (E_i / (1 - xi_i^2))) / (3 * (rho_i_sum)^(1 /
    2))) * (1 / delta_star_i)^(3 / 2);
468-            K_H_o = (((2 * sqrt(2)) * (E_o / (1 - (xi_o)^2))) / (3 * (rho_o_sum)^(1
    / 2))) * (1 / delta_star_o)^(3 / 2);
469-
470-            % Initial guesses for the variables
471-
472-            % Newton-Raphson method parameters
473-            max_iter = 300;
474-            tol = 1e-2; % Reduced tolerance
475-            h = 1e-4; % Reduced step size
476-
477-            sum_rho_o = 1/D*(4 - (1/f_o) - (2 * gamma_o/(1 + gamma_o))); %
    Eq. 44
478-            f_a = 79.8619;
479-            sum_rho_i = 1 /D * (4 -(1/f_i) +(2*gamma_i/(1 - gamma_i))); % Eq.
    40
480-
481-            Qt =f_a/sin(alpha_i); % Eq. 56
482-
483-          %ai = 0.0236 * a_star_i * (Qt / sum_rho_i)^(1/3); % Eq. 59
484-
485-
486-            % Iterate over each position
487-            %Start Loop  solve Newton-Raphson of 16 epsi
488-            for j = 1:length(psi_j)
489-               psi = psi_j(j);
490-
491-
492-                % Initial guess for the current position
493-              %  x0 = [X1j; X2j; delta_oj; delta_ij; delta_a; theta; delta_r];
494-               x0 = [X1j_1; X2j_1; delta_oj_1; delta_ij_1; delta_a; theta;
    delta_r];
```

```
495-            % Newton-Raphson iteration
496-            for iter = 1:max_iter
497-                % Compute the function values
498-                F = compute_F(x0, B, D, alpha_i, R_i, f_i, f_o, K_H_i, K_H_o,
    lambda_ij, lambda_oj, M_g, F_c, Fa, Fr, M, psi, x0);
499-
500-                % Check convergence for F5, F6, and F7
501-                if abs(F(5)) < tol && abs(F(6)) < tol && abs(F(7)) < tol
502-                    fprintf('Converged at position %d, iteration %d.\n', j, iter);
503-                    break;
504-                end
505-
506-                % Compute the Jacobian
507-                J = compute_Jacobian(x0, B, D, alpha_i, R_i, f_i, f_o, K_H_i,
    K_H_o, lambda_ij, lambda_oj, M_g, F_c, Fa, Fr, M, psi, h);
508-
509-                % Check for singularity
510-                if cond(J) > 1e15
511-                    warning('Jacobian is singular or nearly singular at iteration
    %d, position %d. Stopping.', iter, j);
512-                    break;
513-                end
514-
515-                % Solve for the update
516-                dx = J \ F;
517-
518-                % Update the solution
519-
520-                x0 = x0 - dx;
521-
522-                % Check for convergence
523-                if norm(dx) < tol
524-                    break;
525-                end
526-            end
527-
528-            % Store the solution
529-            X1j(j) = x0(1);
530-
531-            X2j(j) = x0(2);
532-
```

```
533-              delta_oj(j) = x0(3);
534-
535-              delta_ij(j) = x0(4);
536-
537-              while true
538-          if Error_Ti <0.1 && Error_To<0.1
539-            Error_Ti=3;
540-            Error_T0=3;
541-              break;
542-
543-             end
544-              %the Eq the private from output N.R
545-              A1 = D*B*sin(alpha_node)+ delta_a +theta *Ri*cos(psi_j(j1));
546-              A2 =  D*B*cos(alpha_node) +delta_r*cos(psi_j(j1));
547-
548-              Qi =  K_H_i * delta_ij(j1)^(1.5); % Eq. 76
549-              Qo =  K_H_o * delta_oj(j1)^(1.5); % Eq. 76
550-
551-              ai=a_star_i*(  ((3*Qi)/(2*rho_i_sum))*   (  ((1-xi_i^2)/E_i)+( (1-
    xi_b^2)/E_b )   )              )^(1/3);
552-
553-              bi =b_star_i*(  ((3*Qi)/(2*rho_i_sum))*   (  ((1-xi_i^2)/E_i)+( (1-
    xi_b^2)/E_b )   )              )^(1/3); % Eq. 61
554-
555-              delta__i=delta_star_i*(  ((3*Qi)/(2*rho_i_sum))*   (  ((1-
    xi_i^2)/E_i)+( (1-xi_b^2)/E_b )   )              )^(1/3)*(rho_i_sum/2); % Eq. 61
556-
557-              ki = ai/bi; % Eq. 62
558-
559-          %ao = 0.0236 * a_star_o * (Qt / sum_rho_o)^(1/3); % Eq. 68
560-              ao=a_star_o*(  ((3*Qo)/(2*rho_o_sum))*   (  ((1-xi_i^2)/E_i)+( (1-
    xi_b^2)/E_b )   )              )^(1/3);
561-              delta__o=delta_star_o*(  ((3*Qo)/(2*rho_o_sum))*   (  ((1-
    xi_i^2)/E_i)+( (1-xi_b^2)/E_b )   )              )^(1/3)*(rho_o_sum/2); % Eq. 61
562-
563-          %bo = 0.0236 * b_star_o * (Qt / sum_rho_o)^(1/3); % Eq. 70
564-              bo =b_star_o*(  ((3*Qo)/(2*rho_o_sum))*   (  ((1-xi_i^2)/E_i)+( (1-
    xi_b^2)/E_b )   )              )^(1/3); % Eq. 61
565-
566-              ko = ao/bo; % Eq. 71
567-
```

```
568-
569-        %Recalculted angles for inner and outer based on output of N.R
570-            p1=(A2-X2j(j));
571-            q1=((f_i-0.5)*D + delta_ij(j));
572-            cos_alpha_ij =p1/q1;
573-
574-        %Inner angle
575-            alpha_i=acos(cos_alpha_ij);
576-            sin_alpha_ij = (A1- X1j(j))/((f_i-0.5)*D + delta_ij(j));
577-
578-        %Outer angle
579-           cos_alpha_oj=X2j(j)/((f_o-.5)*D + delta_oj(j));
580-            alpha_o=acos(cos_alpha_oj);
581-            sin_alpha_0j=X1j(j)/((f_o-.5)*D + delta_oj(j));
582-
583-        % life Equations
584-        gamma_i = (D *(cos (alpha_i)) / dm); % Eq. 77
585-
586-        Qci = 93.2 * ((2 * fi)/(2*fi - 1))^(0.41) * ((1 - gamma_i)^(1.39)/(1 +
    gamma_i)^(1/3)) * ((gamma_i/cos(alpha_i))^(0.3)) * (D^(1.8)) * (Z^(-1/3));
    % Eq. 78
587-
588-        Qci_prime = Qci * (1 - (0.33 * sin(alpha_i))); % Eq. 79
589-
590-        Li = (10^6)*((Qci_prime / Qi)^(3)); % Eq. 80
591-
592-        gamma_o_2 = D * cos(alpha_o) / dm; % Eq. 82
593-
594-        Qco = 93.2 * (((2 * fo)/((2*fo) - 1)))^(0.41) * (((1 +
    gamma_o_2))^(1.39)/((1 - gamma_o_2))^(1/3)) *
    ((gamma_o_2/cos(alpha_o))^(0.3)) * (D^(1.8)) * (Z^(-1/3)); % Eq. 83
595-
596-        Lo = (10^6)*((Qco / Qo)^(3)); % Eq. 84
597-
598-        L = ((Li^(-1.11)) + (Lo^(-1.11)))^(-0.9); % Eq. 85
599-
600-        LH = L/(N * 60); % Eq. 86
601-
602-
603-
604-
```

```
605-
606-        %show relations of the life
607-
608-        %Friction and heat generation calculations
609-        u=0.03;          % Coefficient of friction
610-        ps=15.48;        % A parameter related to the bearing geometry
611-        ohm=46;          % Thermal conductivity W/mm.K
612-        pi_distance=12.79;   % The distance between the same two points
    in inner ring side in mm
613-        po_distance=12.27;   % The distance between the same two
    points in outer ring side in mm
614-        alpha_2= 0.6981 ;    % Nominal contact angle in radian
615-        i=1;             % Number of the rows in bearing
616-        XS=0.5;          % The radial load factor
617-        YS=0.26;         % The axial load factor
618-        Ye=0.33;         % The distance in the Y direction in mm
619-        Ze=0.001;        % The distance in the Z direction in mm
620-        fe=6.6;          % A factor depending upon the type of bearing and
    method of lubrication
621-        vo_opte=5;       % An oil kinematic viscosity at operating
    temperature in mm^2/s
622-        Cp=2.2;          % The specific heat capacity at constant pressure
    J/g.°C
623-
624-
625-        Exi=0.5*((b_star_i)^0.3)*pi*ki;              %Eq.H1
626-        Msi=(3*u*Qi*alpha_i*Exi)/(8);                %Eq.H2
627-        Exo=0.5*((b_star_o)^0.3)*pi*ko;              %Eq.H1
628-        Mso=(3*u*Qo*alpha_o*Exo)/(8);                %Eq.H4
629-        Cs=ps*i*Z*(D^2)*cos(alpha_node);             %Eq.H5
630-        FS=XS*Fr+YS*Fa;                              %Eq.H6
631-        fl=Ze*Ye*(FS/Cs);                            %Eq.H7
632-        P1=0.9*Fa*cot(alpha_node)-0.1*Fr;            %Eq.H8
633-        LoadF=P1/14;
634-        M1=fl*P1*dm;                                 %Eq.H9
635-        Mv=1e-7*fe*(vo_opte*omega)^(2/3)*(dm)^3;     %Eq.H10
636-        Mtotal=M1+Mv;                                %Eq.H11
637-
638-        ns=( ((1-gamma_prime*cos(alpha_i))*tan(alpha_i-
    beta_rad)+gamma_prime*sin(alpha_i))/gamma_prime)*omega*( (1-
    gamma_prime*cos(alpha_i))/(1+cos(alpha_i-alpha_o)) );%Eq.H12
```

```
639-        Hfij=1.047e-4*ns*Msi;                    %Eq.H13
640-        Hfi=Z*Hfij;                          %Eq.H14
641-        Hfoj=1.047e-4*ns*Mso;                    %Eq.H14
642-        Hfo=Z*Hfoj;                          %Eq.H15
643-        H1v=1.047e-4*omega*Mtotal*Z;                 %Eq.H16
644-        Hi_total=H1v+Hfi;                        %Eq.H17
645-        Ho_total=H1v+Hfo;                        %Eq.H18
646-        SpinFH=(Hi_total+Ho_total)/2;
647-        us=0.5*((pi*omega*dm)/60);                   %Eq.H19
648-        Pr=Cp*vo/ohm;                            %Eq.H20
649-        hv=0.0332*ohm*Pr^(0.33)*(us/(vo*dm))^(0.5);      %Eq.H21
650-        Si=(Z*2*(ai/2)*(bi/2)*pi);                   %Eq.H22
651-        So=(Z*2*(ao/2)*(bo/2)*pi);                   %Eq.H23
652-        hsid=(hv*Si+(ohm*Si/pi_distance));           %Eq.H28
653-        hsod=(hv*So+(ohm*So/po_distance));           %Eq.H29
654-        Ti=(Hi_total/hsid)+T_a;                  %Eq.H30
655-        To=(Ho_total/hsod)+T_a;                  %Eq.H31
656-        Error_Ti=abs(Ti-Ti_old);
657-        Error_To=abs(To-To_old);
658-        TotFH=(SpinFH+LoadF+H1v);
659-        Hvi=hv*Si*(Ti-Ts);                       %Eq.H24
660-        Hvo=hv*So*(To-T_h);                      %Eq.H25
661-        Hci=(ohm*Si/pi_distance)*(Ti-Ts);            %Eq.H26
662-        Hco=(ohm*So/po_distance)*(To-T_h);           %Eq.H27
663-
664-        Ti_old=Ti;
665-        To_old=To;
666-
667-          end
668-
669-
670-            AA6= (  ( 1- (D/(dm*cos_alpha_ij)) ))*
    (cos_alpha_oj+(tan_beta*sin_alpha_0j));
671-
672-            AA7=
    (1+(D/(dm*cos_alpha_oj)))*(cos_alpha_ij+(tan_beta*sin_alpha_ij))+ ( 1-
    (D/(dm*cos_alpha_ij)) )* (cos_alpha_oj+(tan_beta*sin_alpha_0j));
673-
674-            Skd_theo = AA6/AA7;
675-
676-          end
```

```
677-
    fprintf("=============================================\n");
678-            fprintf("| %-15s | %-10.5f |\n", "Qi", Qi);
679-            fprintf("| %-15s | %-10.5f |\n", "Qo", Qo);
680-            fprintf("| %-15s | %-10.5f |\n", "alpha_i", alpha_i);
681-            fprintf("| %-15s | %-10.5f |\n", "alpha_o", alpha_o);
682-            fprintf("| %-15s | %-10.5f |\n", "alpha_i_deg",rad2deg(alpha_i) );
683-            fprintf("| %-15s | %-10.5f |\n", "alpha_o_deg", rad2deg(alpha_o));
684-            fprintf("| %-15s | %-10.5f |\n", "count", count);
685-            fprintf("| %-15s | %-10.5f |\n", "Error_Ti", Error_Ti);
686-            fprintf("| %-15s | %-10.5f |\n", "Error_To", Error_To);
687-            allArray{1+count,1}=N;
688-        allArray{1+count,2}=Fa;
689-        allArray{1+count,3}=K_H_i;
690-        allArray{1+count,4}=K_H_o;
691-        allArray{1+count,5}=rad2deg(alpha_i);
692-        allArray{1+count,6}=rad2deg(alpha_o);
693-        allArray{1+count,7}=gamma_i;
694-        allArray{1+count,8}=gamma_o;
695-        allArray{1+count,9}=X1j(j);
696-        allArray{1+count,10}=X2j(j);
697-        allArray{1+count,11}=delta_ij(j);
698-        allArray{1+count,12}=delta_oj(j);
699-        allArray{1+count,13} = F_c;
700-        allArray{1+count,14} = Msi;
701-        allArray{1+count,15} = Mso;
702-        allArray{1+count,16} = P1;
703-        allArray{1+count,17} = M1;
704-        allArray{1+count,18} = Mv;
705-        allArray{1+count,19} = Mtotal;
706-        allArray{1+count,20} = Hfi;
707-        allArray{1+count,21} = Hfo;
708-        allArray{1+count,22} = H1v;
709-        allArray{1+count,23} = Hi_total;
710-        allArray{1+count,24} = Hci;
711-        allArray{1+count,25} = Hco;
712-        allArray{1+count,26} = Hvi;
713-        allArray{1+count,27} = Hvo;
714-        allArray{1+count,28} = Qi;
715-        allArray{1+count,29} = Qo;
716-        allArray{1+count,30} = Skd_theo;
```

```
717-        allArray{1+count,31} = ki;
718-        allArray{1+count,32} = ko;
719-        allArray{1+count,33}=M_g;
720-        allArray{1+count,34}=beta_deg;
721-        allArray{1+count,35}=Li;
722-        allArray{1+count,36}=Lo;
723-        allArray{1+count,37}=L;
724-        allArray{1+count,38}=Ti;
725-        allArray{1+count,39}=To;
726-        allArray{1+count,40}=select;
727-        allArray{1+count,41}=select2;
728-        allArray{1+count,42}=Qci;
729-        allArray{1+count,43}=Qci_prime;
730-        allArray{1+count,44}=Qco;
731-        allArray{1+count,45}=SpinFH;
732-        allArray{1+count,46}=H1v;
733-        allArray{1+count,47}=LoadF;
734-        allArray{1+count,48}=TotFH;
735-
736-        count=count+1;
737-
738-        end
739-
740-        cellArray{1+c_c,1}=N;
741-        cellArray{1+c_c,2}=Fa;
742-        cellArray{1+c_c,3}=K_H_i;
743-        cellArray{1+c_c,4}=K_H_o;
744-        cellArray{1+c_c,5}=rad2deg(alpha_i);
745-        cellArray{1+c_c,6}=rad2deg(alpha_o);
746-        cellArray{1+c_c,7}=gamma_i;
747-        cellArray{1+c_c,8}=gamma_o;
748-        cellArray{1+c_c,9}=X1j(j);
749-        cellArray{1+c_c,10}=X2j(j);
750-        cellArray{1+c_c,11}=delta_ij(j);
751-        cellArray{1+c_c,12}=delta_oj(j);
752-        cellArray{1+c_c,13} = F_c;
753-        cellArray{1+c_c,14} = Msi;
754-        cellArray{1+c_c,15} = Mso;
755-        cellArray{1+c_c,16} = P1;
756-        cellArray{1+c_c,17} = M1;
757-        cellArray{1+c_c,18} = Mv;
```

```
758-        cellArray{1+c_c,19} = Mtotal;
759-        cellArray{1+c_c,20} = Hfi;
760-        cellArray{1+c_c,21} = Hfo;
761-        cellArray{1+c_c,22} = H1v;
762-        cellArray{1+c_c,23} = Hi_total;
763-        cellArray{1+c_c,24} = Hci;
764-        cellArray{1+c_c,25} = Hco;
765-        cellArray{1+c_c,26} = Hvi;
766-        cellArray{1+c_c,27} = Hvo;
767-        cellArray{1+c_c,28} = Qi;
768-        cellArray{1+c_c,29} = Qo;
769-        cellArray{1+c_c,30} = Skd_theo;
770-        cellArray{1+c_c,31} = ki;
771-        cellArray{1+c_c,32} = ko;
772-        cellArray{1+c_c,33}=M_g;
773-        cellArray{1+c_c,34}=beta_deg;
774-        cellArray{1+c_c,35}=Li;
775-        cellArray{1+c_c,36}=Lo;
776-        cellArray{1+c_c,37}=L;
777-        cellArray{1+c_c,38}=Ti;
778-        cellArray{1+c_c,39}=To;
779-        cellArray{1+c_c,40}=select;
780-        cellArray{1+c_c,41}=select2;
781-        cellArray{1+c_c,42}=Qci;
782-        cellArray{1+c_c,43}=Qci_prime;
783-        cellArray{1+c_c,44}=Qco;
784-        cellArray{1+c_c,45}=SpinFH;
785-        cellArray{1+c_c,46}=H1v;
786-        cellArray{1+c_c,47}=LoadF;
787-        cellArray{1+c_c,48}=TotFH;
788-
789-        %Store data the important of Draw
790-        c_c=c_c+1;
791-        if N==6000
792-            Qi_6000(F_aa)=Qi;
793-            Qo_6000(F_aa)=Qi;
794-            Li_6000(F_aa)=L;
795-            Skd_theo_6000(F_aa)=Skd_theo;
796-            alpha_i_6000(F_aa)=alpha_i;
797-            alpha_o_6000(F_aa)=alpha_o;
798-            FC_6000(F_aa)=F_c;
```

```
799-          M_g_6000(F_aa)=M_g;
800-
801-
802-        elseif N==10000
803-          Qi_10000(F_aa-20)=Qi;
804-          Qo_10000(F_aa-20)=Qi;
805-          Li_10000(F_aa-20)=L;
806-          Skd_theo_10000(F_aa-20)=Skd_theo;
807-          alpha_i_10000(F_aa-20)=alpha_i;
808-          alpha_o_10000(F_aa-20)=alpha_o;
809-          FC_10000(F_aa-20)=F_c;
810-          M_g_10000(F_aa-20)=M_g;
811-          H1v_10000(F_aa-20)=H1v;
812-
813-        elseif N==15000
814-          Qi_15000(F_aa-40)=Qi;
815-          Qo_15000(F_aa-40)=Qi;
816-          Li_15000(F_aa-40)=L;
817-          Skd_theo_15000(F_aa-40)=Skd_theo;
818-          alpha_i_15000(F_aa-40)=alpha_i;
819-          alpha_o_15000(F_aa-40)=alpha_o;
820-          FC_15000(F_aa-40)=F_c;
821-          M_g_15000(F_aa-40)=M_g;
822-        SpinFH_10000(F_aa-40)=SpinFH;
823-        LoadF_10000(F_aa-40)=LoadF;
824-        TotFH_10000(F_aa-40)=TotFH;
825-        end
826-
827-
828-
829-        end
830-        %Section Draw the Data
831-        da=0:2500:47500;
832-        figure(1)
833-
834-        % First Subplot: Q values
835-        subplot(3,1,1)
836-        plot(da, Qi_6000, "b-", 'DisplayName', 'Qi 6000')
837-        hold on
838-        plot(da, Qi_10000, "r-", 'DisplayName', 'Qi 10000')
839-        hold on
```

```
840-        plot(da, Qi_15000, "k-", 'DisplayName', 'Qi 15000')
841-        hold on
842-        plot(da, Qo_6000, "m-", 'DisplayName', 'Qo 6000')
843-        hold on
844-        plot(da, Qo_10000, "g-", 'DisplayName', 'Qo 10000')
845-        hold on
846-        plot(da, Qo_15000, "y-", 'DisplayName', 'Qo 15000')
847-        grid on
848-        legend('show', 'Location', 'bestoutside')
849-        title('Q Values Comparison')
850-        xlabel('Fa')
851-        ylabel('Q')
852-
853-        % Second Subplot: L values
854-        subplot(3,1,2)
855-        da_life=25000:2500:47500;
856-        plot(da_life, Li_6000(1:10), "b-", 'DisplayName', 'Li 6000')
857-        hold on
858-        plot(da_life, Li_10000(1:10), "r-", 'DisplayName', 'Li 10000')
859-        hold on
860-        plot(da_life, Li_15000(1:10), "k-", 'DisplayName', 'Li 15000')
861-        grid on
862-        legend('show', 'Location', 'bestoutside')
863-        title('L Values Comparison')
864-        xlabel('Fa')
865-        ylabel('L')
866-
867-        % Third Subplot: Alpha values
868-        subplot(3,1,3)
869-        plot(da, alpha_i_6000, "b-", 'DisplayName', 'αi 6000')
870-        hold on
871-        plot(da, alpha_i_10000, "r-", 'DisplayName', 'αi 10000')
872-        plot(da, alpha_i_15000, "k-", 'DisplayName', 'αi 15000')
873-        plot(da, alpha_o_6000, "m-", 'DisplayName', 'αo 6000')
874-        plot(da, alpha_o_10000, "g-", 'DisplayName', 'αo 10000')
875-        plot(da, alpha_o_15000, "y-", 'DisplayName', 'αo 15000')
876-        grid on
877-        legend('show', 'Location', 'bestoutside')
878-        title('Alpha Values Comparison')
879-        xlabel('Fa')
880-        ylabel('Alpha')
```

```
881-
882-       figure(2)
883-
884-       % First Subplot: Skd_theo values
885-       subplot(3,1,1)
886-       plot(da, Skd_theo_6000, "b-", 'DisplayName', 'Skd 6000')
887-       hold on
888-       plot(da, Skd_theo_10000, "k-", 'DisplayName', 'Skd 10000')
889-       plot(da, Skd_theo_15000, "m-", 'DisplayName', 'Skd 15000')
890-       grid on
891-       legend('show', 'Location', 'bestoutside')
892-       title('Skd Theoretical Values')
893-       xlabel('Fa')
894-       ylabel('Skd')
895-
896-       % Second Subplot: FC values
897-       subplot(3,1,2)
898-       plot(da, FC_6000, "b-", 'DisplayName', 'FC 6000')
899-       hold on
900-       plot(da, FC_10000, "k-", 'DisplayName', 'FC 10000')
901-       plot(da, FC_15000, "m-", 'DisplayName', 'FC 15000')
902-       grid on
903-       legend('show', 'Location', 'bestoutside')
904-       title('FC Values Comparison')
905-       xlabel('Fa')
906-       ylabel('FC')
907-       figure(3)
908-       subplot(3,1,1)
909-       plot(da, Li_6000, "b-", 'DisplayName', 'Li 6000')
910-       title("6000 rpm")
911-       grid on
912-       subplot(3,1,2)
913-       plot(da, Li_10000, "r-", 'DisplayName', 'Li 10000')
914-       title("10000 rpm")
915-       grid on
916-       subplot(3,1,3)
917-       plot(da, Li_15000, "k-", 'DisplayName', 'Li 15000')
918-       title("15000 rpm")
919-       grid on
920-
921-       figure(4)
```

```
922-          Li_6000=Li_6000(1:10)/1000000;
923-          Li_10000=Li_10000(1:10)/1000000;
924-           Li_15000=Li_15000(1:10)/1000000;
925-
926-         plot(da_life, Li_6000(1:10), "b-", 'DisplayName', 'Li 6000')
927-         hold on
928-         plot(da_life, Li_10000(1:10), "r-", 'DisplayName', 'Li 10000')
929-         hold on
930-         plot(da_life, Li_15000(1:10), "k-", 'DisplayName', 'Li 15000')
931-         figure(5)
932-         plot(da,SpinFH_10000,"r")
933-         hold on
934-         plot(da,LoadF_10000,'b')
935-         hold on
936-         plot(da,TotFH_10000,"g")
937-         hold on
938-         plot(da,H1v_10000,"m")
939-
940-         grid on
941-
942-
943-
944-         title("Frication Heat Generation in Watts")
945-         xlabel("Applied Load N")
946-         ylabel("Heat Generation rate in Watts")
947-         legend("SpinFH","LoadF","TotFH","H1v");
948-         %Section save part  from the data in file Exel
949-         fileName = 'DATA_part_Project.xlsx';
950-         writecell(cellArray, fileName);
951-         disp(['data  part save Succes ', fileName]);
952-
953-         %Section  save all data in file Exel
954-         fileName1 = 'DATA_ALL_Project.xlsx';
955-         writecell(allArray, fileName1);
956-         disp(['data all save Succes ', fileName1]);
957-
958-
959-
960-         function F = compute_F(x, B, D, alpha_o, R_i, f_i, f_o, K_H_i, K_H_o,
    lambda_ij, lambda_oj, M_g, F_c, Fa, Fr, M, psi, x0)
961-           % Extract variables
```

```
962-
963-         X1j1= x(1);
964-         X2j1 = x(2);
965-         delta_oj1= x(3);
966-         delta_ij1 = x(4);
967-         delta_a1 = x(5);
968-         theta1 = x(6);
969-         delta_r1 = x(7);
970-
971-
972-         % Compute the equations
973-         F1 = (B * D * sin(alpha_o) + delta_a1 + R_i * theta1 * cos(psi) -
    X1j1)^2 + (B * D * cos(alpha_o) + delta_r1 * cos(psi) - X2j1)^2 - ((f_i - 0.5) *
    D + delta_ij1)^2;
974-         F2 = X1j1 + X2j1^2 - ((f_o - 0.5) * D + delta_oj1)^2;
975-         F3 = (lambda_oj * M_g * X2j1 / D - K_H_o * delta_oj1^1.5 * X1j1) /
    ((f_o - 0.5) * D + delta_oj1) + (K_H_i * delta_ij1^1.5 * (B * D * sin(alpha_o) +
    delta_a1 + R_i * theta1 * cos(psi) - X1j1) - lambda_ij * M_g / D * (B * D *
    cos(alpha_o) + delta_r1 * cos(psi) - X2j1)) / ((f_i - 0.5) * D + delta_ij1);
976-         F4 = (K_H_o * delta_oj1^1.5 * X2j1 + lambda_oj * M_g * X1j1 / D) /
    ((f_o - 0.5) * D + delta_oj1) - (K_H_i * delta_ij1^1.5 * (B * D * cos(alpha_o) +
    delta_r1 * cos(psi) - X2j1) + lambda_ij * M_g / D * (B * D * sin(alpha_o) +
    delta_a1 + R_i * theta1 * cos(psi) - X1j1)) / ((f_i - 0.5) * D + delta_ij1) - F_c;
977-         F5 = Fa - sum((K_H_i * (B * D * sin(alpha_o) + delta_a1 + R_i *
    theta1 * cos(psi) - X1j1) * delta_ij1^1.5 - lambda_ij * M_g / D * (B * D *
    cos(alpha_o) + delta_r1 * cos(psi) - X2j1)) / ((f_i - 0.5) * D + delta_ij1));
978-         F6 = Fr - sum((K_H_i * (B * D * cos(alpha_o) + delta_r1 * cos(psi) -
    X2j1) * delta_ij1^1.5 + lambda_ij * M_g / D * (B * D * sin(alpha_o) +
    delta_a1 + R_i * theta1 * cos(psi) - X1j1)) / ((f_i - 0.5) * D + delta_ij1));
979-         F7 = M - sum((K_H_i * (B * D * sin(alpha_o) + delta_a1 + R_i *
    theta1 * cos(psi) - X1j1) * delta_ij1^1.5 - lambda_ij * M_g / D * (B * D *
    cos(alpha_o) + delta_r1 * cos(psi) - X2j1) * R_i) / ((f_i - 0.5) * D + delta_ij1) +
    lambda_ij * f_i * M_g * cos(psi));
980-
981-         % Penalty terms to keep the solution close to the initial guess
982-         penalty_weight = 1e6; % Adjust this weight as needed
983-         F8 = penalty_weight * (X1j1 - x0(1));
984-         F9 = penalty_weight * (X2j1 - x0(2));
985-         F10 = penalty_weight * (delta_oj1- x0(3));
986-         F11 = penalty_weight * (delta_ij1 - x0(4));
987-         F12 = penalty_weight * (delta_a1 - x0(5));
```

```
F13 = penalty_weight * (theta1- x0(6));
F14 = penalty_weight * (delta_r1- x0(7));

% Combine the equations into a vector
F = [F1; F2; F3; F4; F5; F6; F7; F8; F9; F10; F11; F12; F13; F14];
end

function J = compute_Jacobian(x, B, D, alpha_i, R_i, f_i, f_o, K_H_i, K_H_o, lambda_ij, lambda_oj, M_g, F_c, Fa, Fr, M, psi, h)
% Compute the Jacobian matrix numerically
n = length(x); % Number of variables (7)
m = 14; % Number of equations (7 original + 7 penalty terms)
J = zeros(m, n); % Jacobian matrix of size 14x7

for i = 1:n
  x_temp = x;
  x_temp(i) = x_temp(i) + h;
  F_plus = compute_F(x_temp, B, D, alpha_i, R_i, f_i, f_o, K_H_i, K_H_o, lambda_ij, lambda_oj, M_g, F_c, Fa, Fr, M, psi, x);

  x_temp(i) = x_temp(i) - 2 * h;
  F_minus = compute_F(x_temp, B, D, alpha_i, R_i, f_i, f_o, K_H_i, K_H_o, lambda_ij, lambda_oj, M_g, F_c, Fa, Fr, M, psi, x);

  J(:, i) = (F_plus - F_minus) / (2 * h);
end

end
```

Appendix B: MATLAB in the Computational Framework

B.1 Integration of MATLAB in Computational Frameworks: Reliability, History, and Applications

MATLAB is now a keystone of computational research, and it is a robust platform to solve mathematical problems that are complex in nature. Based on its ability to treat numerical computations effectively, it has become an imperative for researchers working in any field of study. Due to its extensive set of built-in functions, visualization capabilities, and algorithmic features that facilitate accurate and efficient computational modeling, MATLAB is applied in this scientific research. To verify the accuracy and efficiency of the computational framework established in this dissertation, the numerical solution of the governing equations relies on MATLAB, which is a popular numerical computing environment. MATLAB is a robust platform to solve mathematical problems that are complex in nature, and it is endowed with an extensive set of built-in functions, visualization capabilities, and algorithmic features that are particularly tailored for scientific research and engineering applications.

B.2. Numerical Algorithms and Implementation Details

The computational implementation of the coupled model relies on specific numerical algorithms to solve the system of nonlinear and interdependent equations. This section details the primary numerical methods employed in the MATLAB code.

1. **Primary Nonlinear Solver: Newton-Raphson Method**
   The core of the mechanical equilibrium solution is the **Newton-Raphson iterative algorithm**, which is employed to solve the system of nonlinear equations governing the internal load distribution. This system includes:
   - The geometric compatibility equations for each ball position, **(44)** and **(45)**.
   - The ball force equilibrium equations, **(46)** and **(47)**.

- The global equilibrium equations for the entire bearing, **(48)**, **(49)**, and **(50)**.

  The algorithm iteratively refines the primary unknowns—the inner ring displacements (δ_a,δ_r,θ)—by computing the Jacobian matrix of the system and solving for an update vector until the residual norms fall below a specified tolerance (e.g., 1×10^{-6}). This method was selected for its quadratic convergence rate near the solution and its reliability in handling the stiffness and nonlinearity inherent in Hertzian contact problems.

2. **Thermal Coupling Loop: Fixed-Point Iteration**

The thermal analysis is performed via a **fixed-point iteration scheme** (also known as successive substitution). Within each main iteration cycle, the heat generation rates—calculated from the current mechanical state using equations **(105)**, **(107)**, and **(109)**—are used as inputs to a thermal network model. This model solves for the new temperature rises of the inner and outer rings (ΔT_i,ΔT_o) using the heat transfer equations **(117)–(120)**. The loop continues until the absolute change in temperature between successive iterations is less than a convergence criterion ($|\Delta T_{new}-\Delta T_{old}|\leq 0.01$ ∘C).

3. **Auxiliary Numerical Methods**

- **Linear System Solver:** Within each Newton-Raphson iteration, the update vector is found by solving a linear system of equations ($J\cdot\Delta x=-F$). This is accomplished using MATLAB's built-in backslash operator (\), which employs optimized, stable routines for matrix factorization.
- **Numerical Integration:** For calculating elliptic integrals required in the Hertzian contact and EHL formulations, predefined MATLAB functions or high-precision numerical approximations were utilized.
- **Data Interpolation:** For efficiency, material properties and pre-computed dimensionless contact parameters (from Table 3.1) were

stored in lookup tables. **Linear interpolation** was used to fetch values during runtime, balancing accuracy and computational speed.

B.3. Historical Background and Evolution of MATLAB

MATLAB was initially developed in the late 1970s by mathematician and computer scientist Cleve Moler as an interactive matrix calculator for numerical calculations [46]. MATLAB, initially coded in Fortran, was eventually commercialized in 1984 by MathWorks, making it a full-fledged programming language with high-level capabilities [47]. MATLAB has evolved over time, with the addition of specialized toolboxes in control systems, signal processing, image processing, and machine learning, making it an indispensable tool for researchers in a wide variety of fields [48].

B.4. Reliability and Computational Strength of MATLAB

MATLAB is known for its precision and speed of operation of numerical computations since it uses highly optimized math libraries such as LAPACK and BLAS to deliver accurate solutions [47]. The application of MATLAB to efficiently solve large-scale matrix computations, differential equations, and optimization problems makes it the best tool to use for solving large systems, such as those in this dissertation [48]. MATLAB also has graphical capacity, which allows for the simple visualization of computational results, and this facilitates easy interpretation and validation of results [46].

B.5. Applications for MATLAB in Scientific Research

MATLAB is extensively used in various fields, including:

1. Engineering and Physics: Simulation of dynamic systems, finite element analysis, and computational fluid dynamics [48].
2. Data Science and Machine Learning: Development of predictive models, neural networks, and statistical analysis [47].

3. Biomedical Research: Image processing for medical diagnostics, signal analysis for physiological data, and genetic modeling [46].
4. Financial Modeling: Risk assessment, portfolio optimization, and econometric analysis [48].

B.6. Notable Examples of MATLAB in Research

Several groundbreaking studies have utilized MATLAB for computational modeling and analysis:

1. Climate Modeling: MATLAB has been employed in simulating atmospheric dynamics and predicting climate change patterns [47].
2. Robotics and AI: Researchers have developed autonomous robotic systems using MATLAB's control and machine learning toolboxes [48].
3. Structural Engineering: MATLAB has been instrumental in analyzing stress distributions in complex structures, optimizing designs for safety and efficiency [46].

By integrating MATLAB into the computational environment of this dissertation, not only are the numerical solutions presented here mathematically sound and computationally efficient, but they are also based on a well-tested and solid platform. MATLAB's ability for complex mathematical computation, coupled with its analytical and graphical capabilities, ensures that results obtained herein are not only scientifically valid but also practically viable [47].